Fields, forces, and flows: What laboratory experiments reveal about the dynamics of arched plasma structures

Thesis by

Eve Stenson

In Partial Fulfillment of the Requirements

for the Degree of

Doctor of Philosophy

California Institute of Technology

Pasadena, California

2012

(Defended 15 May 2012)

Defiantly dedicated to my parents, Dr. and Dr. Stenson, who really should have been pushier if they'd truly wanted to prevent me from becoming a "failed mathematician".

Acknowledgements

> Mr. Spock: "Under impulse power she expends fuel like any other vessel. We call it 'plasma.' But whatever the Klingon designation, is it is merely ionized gas."
>
> Lt. Uhura: "Well what about all that equipment we're carrying to catalog gaseous anomalies? Well the thing's got to have a tailpipe."
>
> —Stardate 9523.8, figuring out how to detect a cloaked bird of prey
> (*Star Trek VI: The Undiscovered Country*)

I used to think plasmas were "merely ionized gas" (though I lacked Mr. Spock's expertise with plasma propulsion). I had learned back in third grade that there were three states of matter, and when my sixth grade teacher suddenly added another, I was skeptical. Why should some wayward electrons make a gas worthy of being designated a whole separate state? I managed to maintain that skepticism all the way through junior high, high school, and even college. Then, when I was a first year grad student at Caltech, I attended a seminar given by an Applied Physics professor by the name of Paul Bellan, who opened my eyes to how fascinating plasmas can be.

In the years since, thanks to Paul's expert tutelage and his years of patience, I have become quite the fan of the fourth state of matter, joining the ranks of "scientists who have to explain to friends and acquaintances that they are not studying blood" [1] [1]. It has been my great privilege and pleasure to be a part of this research group — to be involved with plasmas and the community of people who study them, both at Caltech and around the world.

From among the ranks of Bellan Plasma Group, I must thank in particular Sett You and Gunsu Yun for being wonderful mentors as well as great officemates. My luck in officemates continued with Bao Ha and Mark Kendall; I have very much enjoyed all of our conversations over the years,

[1] It is highly gratifying to report that at the time of this writing, the top result of a Google search for the word "plasma", displayed just below an ad for an "LG Full HD Plasma TV", is the Wikipedia page entitled "Plasma (physics)". "Blood plasma" comes in second.

both on science and other topics. Other group members with whom I've had the honor of working include Shreekrishna Tripathi, Deepak Kumar, Steve Pracko, Rob Moeller, Rory Perkins, Auna Moser, Vernon Chaplin (whom I owe many thanks, as well as many cookies, for all of the comments and corrections he suggested to this dissertation), Zach Tobin, Xiang Zhai — and, more recently, Taiichi Shikama and K.B. Chai. Dave Felt has been an invaluable colleague, above and beyond his building/repairing the electronics systems upon which my research has relied, as have Eleonora Vorobieff, Connie Rodriguez, and Christy Jenstad. I am also indebted to previous group alumni — such as Carlos Romero-Talamas, Freddie Hansen, Scott Hsu, and Mike Brown — who at conferences and meetings have been generous with their time and insights, even though their tenures in the group finished before mine began.

My time in graduate school has been very much enriched by my current and former roommates (including Jessie Rosenberg, Neil Halelamien, Matthew Kelley, Tobiko, Plato and Socrates, Xerion, and especially my partner in life, adventures, and so much more, Brian Standley). I have also been lucky to enjoy the companionship of many other amazing people, be it via boba runs with Adam Griffith, board games with Scott Tesmer and Photon, dinners (and more) with the potluck group, diving with PCH Scuba and AAU, Frisbee games, dancing, or the Caltech Y, Alpine Club, CCD, et al. Meanwhile, from three time zones away, my sister Kate and the members of "In/Out" have been an ongoing source of support and friendship.

I would like to thank the Caltech faculty who served on my candidacy and/or defense committees — Ed Stone, Joe Shepherd, Sunil Golwala, and Keith Schwab — for their feedback on my research and/or encouragement. I would also like to thank those faculty from whom I took excellent and valuable courses, as well as others who were simply willing to make time for discussions.

That I was in a position to attend Paul's seminar at Caltech to begin with, I owe in part to the countless people who helped, taught, and inspired me over the years. I learned calculus, for example, from Jim Voytas, whose intense enthusiasm for the subject, superhuman vigor, and attention to important subtleties are the stuff of legend. I was lucky to do my undergraduate thesis research with Ben Crooker, whose amazing fluency in both the laboratory and classroom I will always strive to match. The physics faculty at Fordham University provided not only an educational environment, but also a welcoming one; years later, Freeman Hall still connotes to me a sense of "home". Though there is neither time nor space to enumerate them all, to all of the teachers and administrators, classmates and colleagues, friends and family members who have helped me in my personal and professional journey thus far, I will always be grateful.

Abstract

Magnetic flux tubes and, more generally, magnetic field structures that link a plasma volume to its boundary are prominent features in plasma systems of significant interest, such as the solar atmosphere and the interiors of magnetic fusion devices.

In order to study the fundamental physics of these systems, experiments were conducted in the laboratory using a magnetized plasma gun to produce individual arched, plasma-filled magnetic flux tubes. More complex plasma topologies were also explored. The absence of confining walls allowed plasmas to evolve freely — which they did, very dynamically, over the course of several microseconds. The experiment setup featured excellent reproducibility, extensive diagnostic accessibility, and several tunable parameters. In particular, a plasma "color coding" technique and magnetic measurements provided new and interesting results.

The single arches or "loops" of plasma exhibited sustained axial collimation, even during a dramatic evolution from a small, semicircular arch into a kinked structure up to seven times larger. The loops' magnetic structure was verified as consistent with that of a flux tube, and their evolution was found to be in quantitative agreement with two interrelated magnetohydrodynamic (MHD) theories: a simplified hoop force model for the axis expansion and a recently proposed MHD flow model for the collimation. More complex plasma structures were found to be similarly dominated by the effects of the magnetic field, exhibiting behavior that was highly repeatable but varied significantly from one magnetic structure to the next.

These findings suggest that MHD-driven flows are an important mechanism for the transport of plasma in arched flux tubes and other magnetic plasma structures. Because MHD has no inherent length scale, the forces driving the evolution of these experiments are expected to similarly affect other systems with low plasma beta and a high Lundquist number.

Contents

List of Figures

List of Tables

Chapter 1

Introduction

> "If there turn out to be any practical applications, that's fine and dandy. But we think it's important that the human race understands where sunlight comes from."
>
> —Nobel Laureate William Fowler, 1983 [2]

> "The sun is a mass of incandescent gas . . ."
>
> —They Might Be Giants, 1993 ("Why Does The Sun Shine?")

> "The sun is a miasma of incandescent plasma . . ."
>
> —They Might Be Giants, 2009 ("Why Does The Sun Really Shine?")

1.1 The big picture

To those who are unfamiliar with it, "the fourth state of matter" may sound like a creation of science fiction or fantasy authors, akin to "the sixth sense". To be sure, many authors in these genera do employ plasma-based creations, from radiating life forms to futuristic technologies. Plasma weaponry is a particularly popular option. And *Star Trek* aficionados know plasmas have an integral role in the warp drive of a faster-than-light starship — that is, if you believe Gene Rodenberry, the creator of that universe.

In our nonfictional universe (sadly lacking in warp drives), plasmas are still pretty fantastic. They are the stuff of neon lights, nanoscale circuit fabrication, the auroras, and — as it turns out — the vast majority of all known matter. Indeed, plasma physicists are fond of the figure that 99 percent (or perhaps 99.999...percent, depending on whom you ask) of the visible universe is

composed of plasma. This includes astrophysical jets whose lengths are measured in light years, the diffuse interstellar medium, huge discs of particles accreting around stars or black holes, the stars themselves, and more.

There is one star, of course, with which our planet has a very intimate relationship. Our Sun is plasma through and through, from its core where fusion takes place to its surface covered in arched magnetic plasma structures. Some of the structures are unstable and erupt, sending large quantities of magnetized plasma out into the solar system. If those outgoing solar "storms" encounter Earth, they not only produce dazzling auroras, but can also damage satellites and power grids. Understanding the physics of what causes eruptions can help us predict and respond to inclement "solar weather."

Back here on earth, nuclear fusion devices attempt to create plasmas that are hot and dense enough to replicate what happens naturally in the solar core — i.e., produce fusion energy — but without the benefit of a star's gravity to help with the confinement. One approach to the problem is to corral the plasma in 3D magnetic field configurations — for example, donut-shaped or cruller-shaped toroidal configurations, known as tokamaks and stellerators. At the boundary between the hot, confined plasma and the cool wall of the surrounding metal vacuum chamber are important structures known as divertors.

Both divertors and solar coronal phenomena involve plasmas whose magnetic field lines connect them to a boundary. The physics of these plasma systems can be difficult to capture in computer models, and in some cases, direct measurements of phenomena are complicated or impossible. Fortunately, because the relevant magnetohydrodynamic (MHD) equations for describing magnetized fluids (which will be discussed in detail later in this chapter) have no built-in dependence on the size of the system, we can construct laboratory experiments that experience the same physics, while providing reproducibility, diagnostic accessibility, and some parameter tuning.

Alongside theoretical models, computer simulations, and observations of naturally occurring plasma systems, these experiments allow us to further advance our knowledge of fundamental plasma physics.

1.2 Introduction to plasmas

Plasmas exist over a mind-boggling span of temperatures and pressures. The Contemporary Physics Education project has an oft-displayed graph depicting this span, shown here in Figure 1.1a. Note

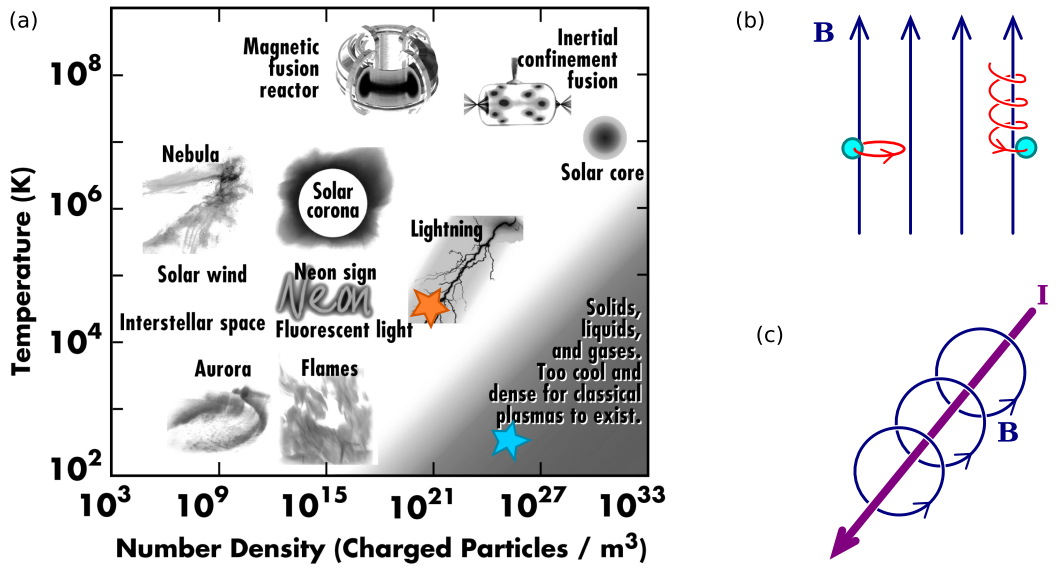

Figure 1.1: a.) A variety of plasmas are plotted according to their densities and temperatures. The orange star marks the conditions of the plasma experiments described in this dissertation, while the blue star marks Standard Temperature and Pressure (graph ©2010 Contemporary Physics Education Project, used with permission). b.) A charged particle moving in a uniform magnetic field follows a circular or helical path. It is free to move in the direction parallel to the field, but movement in the perpendicular direction is restricted to the radius of its circle (the size of which depends on its speed in the perpendicular direction). c.) A wire carrying an electric current creates a magnetic field that circles around it.

that the vertical axis, indicating temperature with a logarithmic scale, ranges from 100 to 1,000,000,000 Kelvin. The horizontal axis, indicating density with a logarithmic scale, ranges from 10^3 to 10^{33} particles per cubic meter. The blue star marking the temperature and pressure conditions considered "standard" by chemists and other scientists around the world[1] lies in bottom right eighth of the graph, where the label reads: "Solids, liquids and gases. Too cool and dense for classical plasmas to exist." Human beings are far more familiar with the first three states of matter.

In addition to being much hotter and less dense than the first three states of matter, plasmas are also ionized (their defining feature). Some percent of the atoms have lost one or more electrons, resulting in a soup of positively and negatively charged particles, all whizzing around one another.[2] Since moving, charged particles are influenced by electric and magnetic fields (Figure 1.1b), and in

[1] E.g., the 293 K and 2.5×10^{25} m^{-3} specified by the National Institute for Standards and Technology

[2] Francis Chen points out that not just any ionized gas can be considered a plasma, since there is a small percentage of ionization in any gas. He defines a plasma as "a quasi-neutral gas of charged and neutral particles that exhibits collective behavior" [3]. Roughly speaking, "quasi-neutral" means that one must zoom in to very small scales (relative to the size of the plasma) in order to find a "chunk" that doesn't have equal numbers of ions and electrons.

However, it should be noted that there is a subfield within plasma physics devoted to the study of "nonneutral plasmas" — for example, collections of electrons (but no ions) at plasma densities and temperatures — that do not meet the requirement of quasi-neutrality.

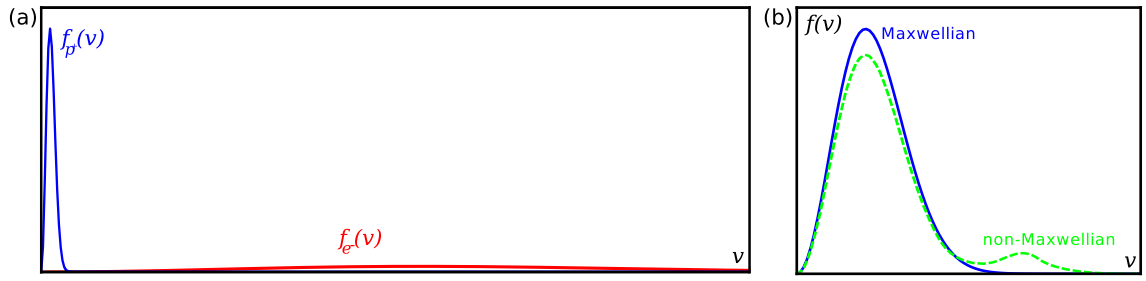

Figure 1.2: a.) Velocity distribution functions $f_{p^+}(v)$ and $f_{e^-}(v)$ for ions and electrons, respectively, that have equilibrated at the same temperature. b.) Even within a single species, if there is a source of heating but insufficient collisions to distribute that energy among all the particles, a non-Maxwellian distribution may arise, and the temperature would not be well defined.

turn generate electric and magnetic fields (the latter shown in Figure 1.1c), phenomena emerge that simply do not exist for neutral gases.

The high temperatures, low densities, and ionization can result in conditions quite unintuitive for plasma physics neophytes. Examples, some of which are illustrated in Figures 1.2 and 1.3, include:

- that a plasma with a temperature in the tens of thousands of degrees doesn't melt the experimental apparatus with which it comes in contact (because the energy density is so low);
- that ions and electrons occupying the same volume might be at different temperatures (because interspecies collisions transfer far less energy than intraspecies collisions, due to the difference in mass between ions and electrons); but if they are at the same temperature, the electrons are going much faster than the ions[3];
- that the temperature of a species might not even be well defined (because there may not even be enough intraspecies collisions to yield a Maxwell-Boltzmann distribution of velocities), or may not be isotropic (because the presence of a magnetic field is a source of anisotropy);
- that the magnetic field can be thought of as a curious type of rubber band that the plasma may drag, stretch, or even snap.

Note that some of those effects can coexist; others cannot. In short, plasmas yield a very rich (and sometimes confusing) physics. There are many different regimes, and there are infamously many

[3]According to the Maxwell-Boltzmann equation, a group of particles with mass m and temperature T have $f(v) = 4/(\sqrt{\pi})(m/2kT)^{3/2}v^2e^{-mv^2/(2kT)}$ as the distribution function for the magnitude of their velocities. The integral $\int_{v_1}^{v_2} f(v)\mathrm{d}v$ then gives the fraction of particles with speeds $v_1 < v < v_2$. Due to the dependence on mass, this implies that if the ions and electrons in a plasma are indeed at the same temperature, the electrons are moving much faster than the ions.

different types of waves (each with different components of the plasma vibrating in different ways). Fortunately, there are also plenty of sets of equations to choose from to help sort it all out.

1.3 Plasma regimes, especially magnetohydrodynamics

The most complete description of a plasma involves keeping track of the speed and location of every single particle, and does this for all, say, 10^{20} particles in the volume of interest. This would be a rather unenviable assignment: lots of tedium, little opportunity to see the big picture.

Instead, consider "grouping" particles with similar characteristics, and describing the plasma by means of a distribution function $f(\mathbf{x}, \mathbf{v}, t)$. (Integrated, this gives the number of particles at time t with positions and velocities in phase space (i.e., the six-dimensional space of $\mathbf{x}$ and $\mathbf{v}$) between the limits of the integral.) From this starting point, one can use conservation of particles in phase space to derive the Vlasov equation

$$\frac{\partial f}{\partial t} + \mathbf{v} \cdot \frac{\partial f}{\partial \mathbf{x}} + \frac{\partial}{\partial \mathbf{v}} \cdot (\mathbf{a} f) = 0. \tag{1.1}$$

The only hitch is that collisions cause particles to appear and disappear in phase space, so in order to take collisions into account the zero on the right-hand side needs to be replaced with a "collision operator" that glosses over the details a bit.

These are the sorts of tradeoffs that one must consider: by making assumptions or glossing over details, equations can be derived that are simpler, easier to understand, and easier to apply. It is a good trade to make, so long as the system to be described is outside the realm where those details are important and those assumptions become untrue. The Vlasov equation would not be a good tool for a system whose interesting physics happens at the level of those collisions, but in all other cases, it works great.

From the Vlasov equation and the distribution function, one can take moments and make judicious assumptions about the time scales of the phenomena being studied to achieve a still more approachable description of the plasma: the two-fluid approach, in which the ions and electrons are mathematically represented not as individual particles, but with each species' collective qualities: density, mean velocity, pressure, etc. The two-fluid equations relate these quantities and their time and spatial derivatives to one another and to other quantities such as electric and magnetic fields.

Next, one can combine the two-fluid equations, giving up knowledge of the individual species'

densities and velocities in favor of their cumulative density and their relative velocities (i.e., electric current). After integrating over a few more quantities, the result is magnetohydrodynamics. Magnetohydrodynamics (MHD) is the system of equations for describing a magnetized fluid in terms of its density (ρ), center of mass velocity ($\mathbf{U}$), electric current density ($\mathbf{J}$), pressure tensor ($\mathbf{P}$), resistivity (η), electric field ($\mathbf{E}$), and magnetic field ($\mathbf{B}$).

MHD comprises the continuity equation

$$\frac{\partial \rho}{\partial t} + \nabla \cdot (\rho \mathbf{U}) = 0, \tag{1.2}$$

the equation of motion[4]

$$\rho \frac{\mathrm{D}\mathbf{U}}{\mathrm{D}t} = \mathbf{J} \times \mathbf{B} - \nabla \mathbf{P}, \tag{1.3}$$

Faraday's law

$$\nabla \times \mathbf{E} = -\frac{\partial \mathbf{B}}{\partial t}, \tag{1.4}$$

Ampere's law

$$\nabla \times \mathbf{B} = \mu_0 \mathbf{J}, \tag{1.5}$$

Ohm's law

$$\mathbf{E} + \mathbf{U} \times \mathbf{B} = \eta \mathbf{J}, \tag{1.6}$$

and a slew of assumptions about the characteristics of the system under consideration. These include assumptions about length scale (large enough that the plasma is quasi-neutral), characteristic velocities (slow relative to the speed of light), relationship between the pressure and density gradients (parallel), time scale (longer than the cyclotron periods of both the electrons and ions), and what you're going to do with Ohm's law (always take its curl). Yet another approximation — a very useful one, as it turns out — is possible when the resistivity is very low, so that the right-hand side of Ohm's law can then be set to zero. This is known as ideal MHD.

For plasmas that satisfy all of those assumptions and conditions, ideal MHD is a very good description. For those that don't, the equations above will not accurately predict or explain the plasma's behavior, and other equations will be needed. The plasmas created in the Bellan Group are, in fact, primarily in the ideal MHD regime. (It is worth noting, though, that the boundary between different regimes can be surprisingly thin, and plasmas sometimes cross it without warning [4, 5].

[4]Note that $\frac{\mathrm{D}}{\mathrm{D}t} = \frac{\partial}{\partial t} + \mathbf{U} \cdot \nabla$ is the convective derivative defined by the center-of-mass velocity — i.e., a derivative in the frame of the moving plasma.

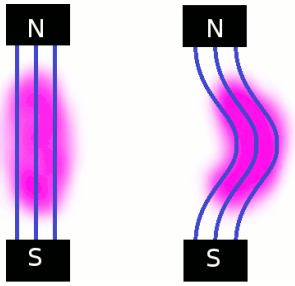

Figure 1.3: Cartoon of frozen-in flux. When the plasma moves, the frozen-in magnetic flux moves with it, modifying the externally generated magnetic field.

One of the benefits of experiments over computer simulations, though, is that when conditions arise such that the expected mathematical description no longer applies, the system just does something surprising, rather than something unphysical.)

It can be shown that in the limit of zero resistance that defines ideal MHD, the magnetic flux Φ satisfies the equation

$$\frac{\mathrm{D}\Phi}{\mathrm{D}t} = 0. \tag{1.7}$$

Since its convective derivative is zero, the flux does not change in the frame of the moving plasma. Rather, the plasma and the magnetic flux move together, as illustrated in Figure 1.3. This is known as the ”frozen-in flux” condition. When it is satisfied, there is a great intuitive advantage to thinking of the plasma in terms of its magnetic topology.

1.3.1 Magnetic flux tubes

A magnetic flux surface is determined by tracing out the path of one or more magnetic field lines. In a toroidal system, such as a tokamak or stellerator, some magnetic field lines close upon themselves after traversing the device a finite number of times; the ratio of times a field line is “wrapped” around the major radius to the number of “transits” along the major radius is given by a rational number. Other field lines never close upon themselves; in this case, the ratio of wraps to transits is irrational. A single, nonclosing field line ergodically fills an entire three-dimensional surface; these are called irrational surfaces. Rational surfaces exist between irrational surfaces and are formed from a collection of infinitely many closed field lines. [6]

Both irrational and rational surfaces are *closed flux surfaces*; that is, the magnetic field lines are entirely contained within the plasma volume. *Open flux surfaces*, on the other hand, are character-

ized by magnetic field lines linking the boundary to the plasma volume of interest.[5] Like a rational surface, an open flux surface is formed from a collection of magnetic field lines, typically chosen based on the symmetry of the system.

Magnetic flux tubes are examples of open flux structures, typically defined by the central axis of a "rope" of twisted magnetic field lines, and they can act a conduit for the transportation of particles and energy between the locations at different ends of that rope. That the flux tube is twisted implies that the curl of $\mathbf{B}$ is finite, so magnetic flux tubes also carry finite current.

Since magnetic fields cause charged particles with velocities perpendicular to the field to undergo cyclotron orbits about the direction of the field, these charge carriers are essentially limited to travel along magnetic flux surfaces (to which the magnetic fields are parallel). That is, current flows along flux surfaces.

Depending on the specific orientation of the current and the magnetic field lines, a pressure gradient may exist such that the flux tube is in equilibrium (i.e., $\mathrm{D}\mathbf{U}/\mathrm{D}t = 0$ on the left hand side of Equation 1.3). In the case where the current and the magnetic field are exactly parallel, all the terms in the equation of motion are identically zero. This is a "force-free" flux tube. If, on the other hand, there is a finite angle between $\mathbf{J}$ and $\mathbf{B}$, then this will be balanced in equilibrium by ∇P, and the flux tube can be filled with higher density plasma[6].

1.3.2 Helicity

Another feature of the flux tube that can be important is whether those twisted magnetic field lines defining the flux tube have a right-handed twist or a left-handed twist. If the twist is right-handed, then the curl of the twist points in the same direction along the flux tube as the magnetic field lines themselves. I.e., current and magnetic field are approximately parallel. If the twist is left-handed, then they are approximately antiparallel. The helicity[7] of a magnetic flux tube — and a plasma in general — significantly affects how it interacts with its surroundings. And "the surroundings" of magnetic flux tubes can be quite diverse.

---

[5] A note on terminology: In the solar physics community, the terms "open magnetic field line" and "closed magnetic field line" *both* refer to field lines in the solar corona that connect to the adjacent bounding surface (i.e., the photosphere). The latter return to the photosphere within a solar radius or two, while the former connect to the solar wind, fulfilling the requirement that $\nabla \cdot \mathbf{B} = 0$ somewhere far out into the solar system, or beyond.

[6] In the case of isotropic pressure, the pressure tensor $\mathbf{P}$ reduces to the standard gas pressure P.

[7] Helicity is actually much more complex than just the handedness of the twist. For one thing, helicity is a scalar quantity, defined as $K = \int \mathbf{A} \cdot \mathbf{B}\, \mathrm{d}^3 r$ for systems of closed flux. (For open flux systems, gauge ambiguity results in a need to define a "relative helicity" instead.) Helicity includes not only twist, but also kinks and "linkages" (e.g., two rings linked together). For some plasmas, helicity can be a conserved quantity, which can have very interesting results.

1.4 The use of laboratory experiments to elucidate fundamental plasma physics relevant to solar and astrophysical phenomena

Magnetic flux tubes — and, more generally, magnetic field structures that intercept a boundary — are important to a wide variety of plasma systems. Examples include solar coronal phenomena (e.g., solar coronal loops, coronal mass ejections, and prominences) [7] [8], astrophysical jets [9], spheromak formation[8] [10], and divertors in magnetic fusion confinement devices [11] [12]. Many of these systems can exhibit rapid dynamic evolutions. Many also pose challenges for computer simulations and/or direct observation.

Computational models often assume reduced dimensionality [13] [14], zero velocity at the boundary [15], and/or periodic boundary conditions [16]. By definition, these models cannot investigate boundary interactions other than those which are assumed. Furthermore, questions have been raised about force-free assumptions [17] often used in solar coronal models, and about the mechanisms for transporting magnetic flux into the corona [14] (another aspect of models that tends to be specified, rather than derived).

While theoretical analyses that assume a force-free state or an equilibrium state are invaluable for situations in which that is indeed the case, they necessarily fail to consider phenomena for which it is not. Many cases of interest involve plasma that is neither uniformly distributed nor stationary. As a result, the rich dynamics of this regime can be difficult to capture.

Direct solar observations also have limitations; coronal events are not reproducible and cannot be measured *in situ*. Although advancements have been made in measuring the solar coronal magnetic field [18, 19, 20], the field is typically calculated from models that assume it is potential or force-free above the photosphere [8]; results differ [21] and may not represent the real system [22].

By contrast, laboratory plasmas are diagnostically accessible and can be highly reproducible, allowing systematic study of configurations where field lines intercept boundaries and exhibit, for example, solar-like dynamics [23]. In addition to work at Caltech, such experiments are in operation at Los Alamos National Laboratory [24], UCLA [25], and Princeton Plasma Physics Laboratory [26], to name a few.

[8] Spheromaks are an "innovative confinement concept" for fusion energy and take advantage of the plasma's tendency to self-organize. A spheromak plasma undergoes a relaxation process to form a toroidal structure in its simply connected (spherical) chamber, rather than having that structure imposed by a toroidal chamber (as is done for much more expensive, but also much more developed, tokamak fusion energy devices).

1.5 Overview of this dissertation

This dissertation, of course, is about the progress that has been made at Caltech toward this end. To facilitate future reference to the data presented herein, shot numbers are typically included in captions. To facilitate recognition of symmetries and other important features, plasma loop images are rotated to be apex up — except in discussions of the experiment setup. (Gravity is not a factor in the loops' evolution, but human perception is strongly biased by human eyes' horizontal orientation.)

The story begins with the experiment setup that makes it all possible (Chapter 2), continues through the (dynamic) lives and (brief) times of individual arched magnetic flux tubes (Chapters 3–4), then delves into more complicated arched plasma structures (Chapter 5). Chapter 6 provides a brief summary of the dissertation's findings, as well as suggestions for future work. For those who seek to know more, appendices are provided in abundance.

Chapter 2

Experiment details

> "Experiment can simulate computation: Resolves all scales, includes all correlations, includes all MHD and kinetic effects, "CPU time" $<$ 1 second."
>
> — presentation by physicist Stewart Prager (CMPD/CMSO plasma winter school, 2008)

This chapter describes the experiment setup at Caltech used to create all of the laboratory plasmas that are the topic of this dissertation.

The setup comprised a modestly sized, pulsed-power, magnetized plasma gun; installed in a much larger vacuum chamber; outfitted with a varied — and ever-changing — collection of diagnostics. A fiber optic timing system handled all of the experiment triggers. High-speed data acquisition and several types of computer software were used to acquire, process, and analyze the data.

The resulting plasma structures were typically tens of centimeters in size, and with lifetimes measured in microseconds.

2.1 Vacuum system

The stainless steel vacuum chamber is a total of 2 meters long and 1.5 meters in diameter, making it considerably larger than the plasma. As a result, the plasma effectively exists in a "half infinite space". This is in contrast to plasma confinement devices that traditionally have a conducting wall very close to the plasma (in order to suppress instabilities and maintain steady state operation), and it allows the plasma to evolve dynamically in the ways it "sees fit" to do.

Figure 2.1 shows the scale of the chamber and the electrode of the magnetized plasma gun

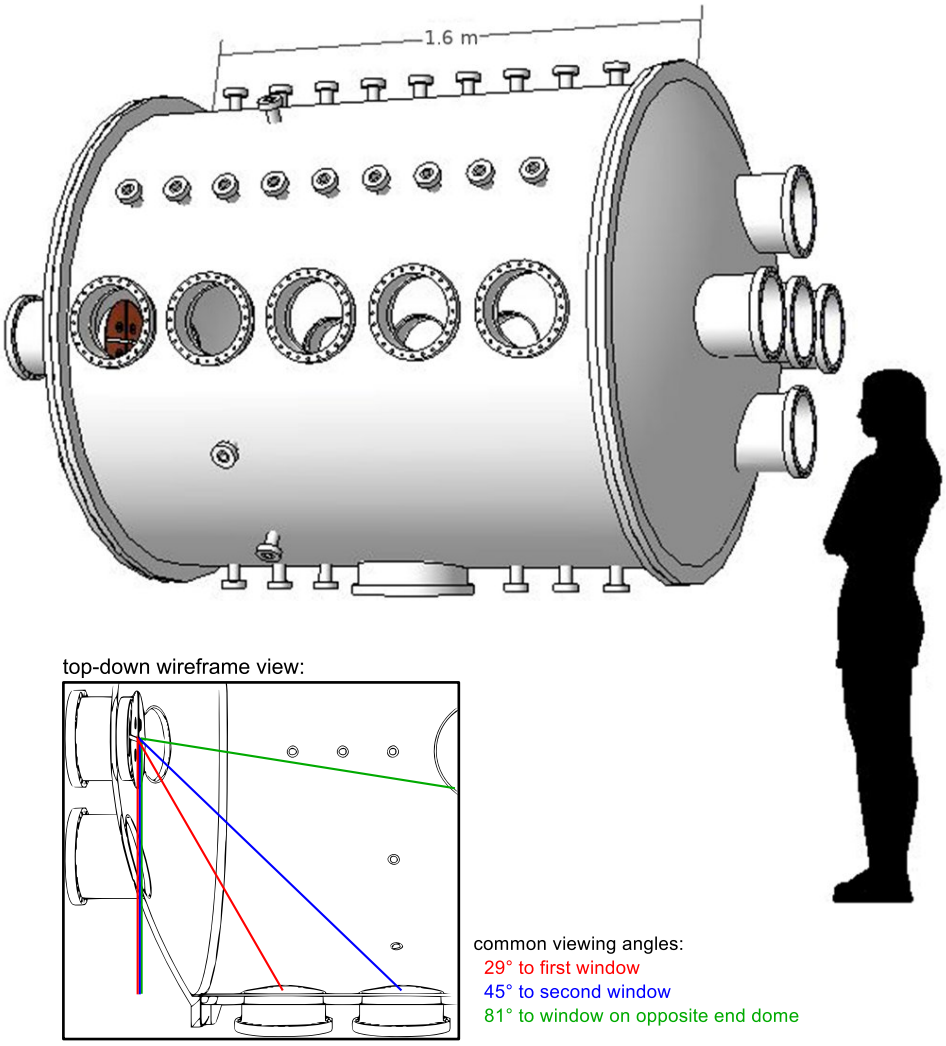

Figure 2.1: Illustration of the vacuum chamber (with a 5' graduate student shown for scale). The inset shows three viewing angles commonly used for photography and spectroscopy of the plasma. (3D model of the vacuum chamber input to Google SketchUp by Gunsu Yun)

(visible through the first window). The figure inset illustrates common viewing angles for the experiment's high-speed cameras and spectroscopic lines of sight.

The vacuum chamber is typically maintained at a pressure of 5×10^{-8} to 3×10^{-7} Torr. The vacuum system is oil-free, so pump oil will not contaminate the chamber. When pumping the chamber down from atmospheric pressure, a Varian Megasorb pump is used down to about 100 mTorr, after which a cryopump[1] takes over, achieving and maintaining high vacuum. The cryopump is connected to the large port on the bottom of the chamber via a gate valve. The gate valve is used to isolate the chamber from the pump for such purposes as regenerating the pump without bringing

[1] An APD-12SC was used until 2010, at which point it was replaced with a Marathon CP-12 cryopump.

the chamber up to atmosphere, measuring gas valve output via pressure increase in the unpumped chamber, and protecting the pump in the event of an unexpected vacuum break.

A Tribodyne pump is used to evacuate the gas lines for the magnetized plasma gun before each set of experiments (prior to their being filled with the gas species of choice for that set). The same pump is also used to evacuate the cryopump after it has been regenerated.

2.2 Magnetized plasma gun

2.2.1 History and overview

The magnetized plasma gun used for these experiments is the fourth "solar" gun at Caltech. It was first installed in the vacuum chamber in 1999 by Freddy Hansen, and was described in detail in Chapter 5 of his thesis [27]. Modifications have been made to its gas and main power delivery systems since, but much of the operation has remained the same.

Its Mark I and Mark II predecessors were installed on the chamber from 1996 to 1997 and 1997 to 1999, respectively. The Mark III gun, similar to the Mark II and originally built to be used in tandem with it, was not deployed until 2011, when it was installed on a smaller vacuum chamber added to the lab that year. A fifth gun is currently under construction; it is scheduled for installation on the main vacuum chamber in 2012, in place of the Mark IV gun.

A different model of plasma gun is located on the opposite end dome of the main chamber. This model has eightfold radial symmetry, with an inner circular cathode and an outer annular anode. Essentially a coplanar spheromak gun[2], it was installed on the chamber in 2001 by Scott Hsu [28]. It replaced a coaxial spheromak gun installed in 1998 by Jimmy Yee [29]. A second coplanar gun was recently installed on the small chamber, opposite the Mark III gun, by Vernon Chaplin.

Thus, by the end of 2012, eight different plasma guns will have been operated in the Bellan Group laboratories over the years.[3] For the most part, all of these guns operate by the same basic sequence:

1. Establish a vacuum magnetic field.

2. Release neutral gas in the vicinity of the magnetic field lines.

[2] As mentioned in Chapter 1, spheromaks are an "innovative confinement concept" for fusion energy and take advantage of the plasma's tendency to self-organize.

[3] The addition of the smaller vacuum chamber allows a maximum of four guns to be installed and ready for use at any given time. Due to shared diagnostics and timing systems, though, as well as high voltage concerns, guns mounted on the same chamber are not operated simultaneously.

3. Apply high voltage across the magnetic field lines to ionize the gas.

The geometry of the gun and the specifics of these three elements, however, yield highly disparate plasmas that may undergo very different physical processes.

The current (Mark IV) gun is shown in Figure 2.2. It is sometimes called a "quad gun" due to the outward fourfold symmetry; the copper electrode at the front of the gun is a circle divided into four quarters, and behind each electrode is an identical set of components. When the main power supply is connected, though, the gun is at most bilaterally symmetric. For all the experiments described there, the top two quarters are electrically connected to one another, together forming a cathode; the bottom two quarters compose the anode.

There is one opening in each quarter of the electrode through which gas may be released into the chamber. Coaxial with each gas nozzle is a coil that can be pulsed to produce a vacuum magnetic field (also known as a "potential field" or a "stuffing flux").

2.2.2 Vacuum magnetic field system

The four magnetic field coils are pulsed with the same two electrolytic capacitor banks that were installed by Hansen. Each bank is equipped with a fast charging unit for convenience. One bank energizes either or both of the two top magnetic field coils. The other bank energizes either or both of the two bottom magnetic field coils.

Each coil can produce a magnetic field pointing in toward or out from the vacuum chamber. This polarity is determined by the polarity with which the coil leads are attached to the capacitor bank cables; switching the leads reverses the direction current flows through the coils and the resulting magnetic field. The leads to a coil can also be detached completely.[4]

The typical magnetic fields produced have a magnitude of 0.3–0.4 T, measured at the electrode surface directly in front of the coil/nozzle axis, and a lifetime on the order of milliseconds. Thus, they are unchanging on the time scale of a microsecond plasma shot. Detailed measurements (of which there are several) of the spatial and temporal properties of the vacuum field, and how they vary with capacitor bank charging voltage, are described in Appendix A.

By adjusting the charging voltage, energizing a different selection of the coils, and/or switching coil polarities, one can create a variety of different magnetic field configurations that in turn guide different plasma structures.

[4] Although this implies that there are 3^4 different coil attachment options, the symmetry of the system results in considerably fewer distinct types of plasma structures.

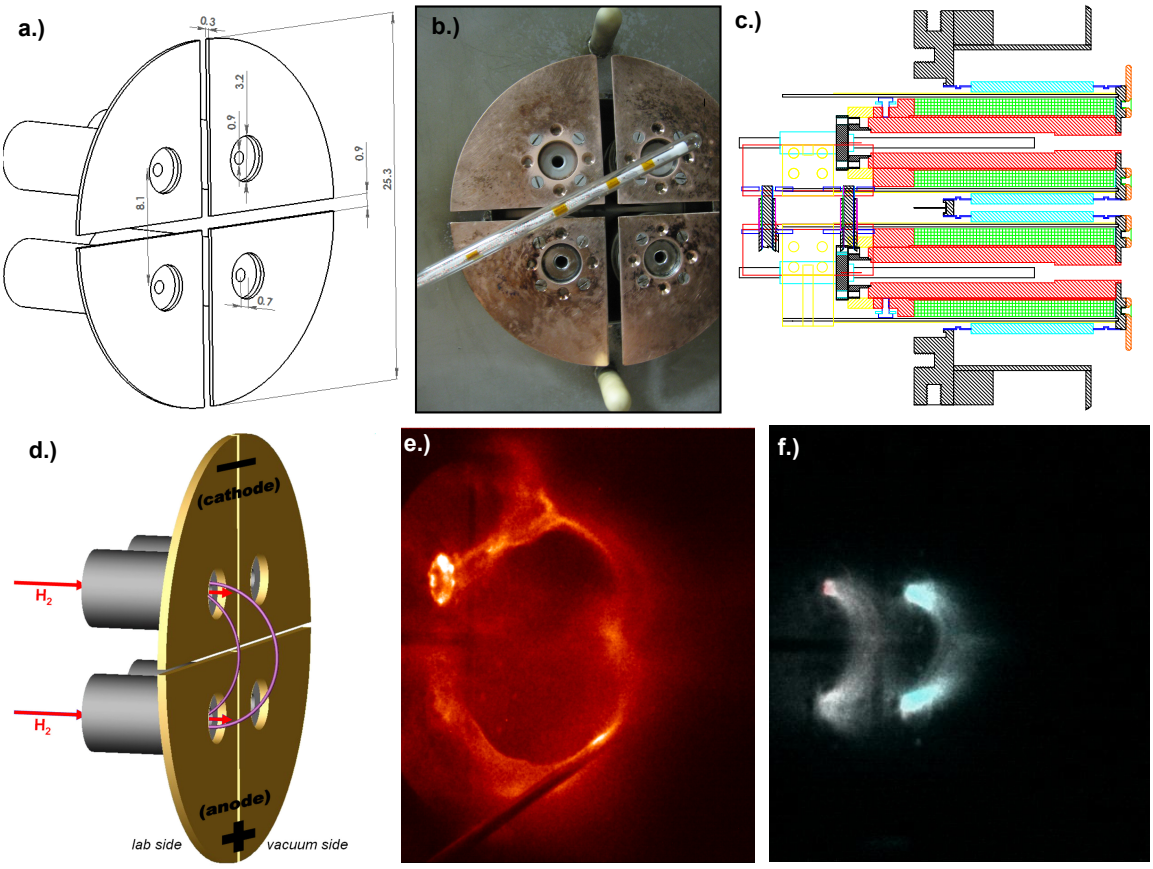

Figure 2.2: A collection of views of the solar "quad" gun:
a.) Electrode dimensions
b.) Photograph of the electrode (focused on the "near" half, as defined by proximity to the side of the chamber from which the plasma is photographed), with an arm that houses an array of magnetic probes in the foreground. This was taken from inside the chamber with a slightly wide-angle lens. (The ceramic bolt covers at the top and bottom of the photo are, in fact, parallel.)
c.) CAD drawing of the internal components of the gun and its position in the vacuum chamber port (created by Paul Bellan and included here with permission). Green sections are magnetic field coils. Red sections are iron. The long, central structures outlined in black are gas lines.
d.) Illustration of the gun, when configured to make a single hydrogen plasma loop; the purple arches represent the vacuum magnetic field lines (though they are not to scale).
e.) A single hydrogen plasma loop, photographed through the first window, just as it reaches the arm of the magnetic probe array. *(shot 5772)*
f.) A hydrogen loop (tinted red) and a nitrogen loop (tinted blue), shown shortly after breakdown during a two-loop (cohelicity) experiment. *(shots 5357, 5360, and 5362)*

The most straightforward setup is to energize a pair of vertical coils with opposite polarities (Figure 2.2d). The resulting field is akin to that of a horseshoe magnet, and may be parallel or antiparallel to the direction of the current, which flows from anode on the bottom to the cathode on the top. When the two are parallel, the plasma will have right-handed helicity; when they are antiparallel, it will have left-handed helicity. These individual loops of plasma are the topic of Chapter 3; an example is shown in Figure 2.2e.

To make a pair of plasma loops, as shown in Figure 2.2f, four coils are energized. This can be done in such a way that two loops have the same handedness (both right or both left) or the opposite handedness (one of each). These are called cohelicity and counterhelicity setups, respectively, and are discussed in Chapter 5, along with other, more "exotic" magnetic field structures.

It is important to note that the correlation between the vacuum field structure and the plasma structure can vary from being very high to quite low, depending on the extent to which the vacuum field is "compatible" with the requirements for plasma breakdown and current conduction — i.e., the presence of neutral gas.

2.2.3 Gas delivery

When high voltage is applied to the electrodes, breakdown occurs via an avalanching of electrons, starting with a few stray "primary" electrons that are accelerated from cathode to anode by the electric field. These electrons can ionize neutrals via collisions, provided they both A.) can gain sufficient energy between collisions, and B.) encounter neutrals before encountering the anode.

Therefore, in order to produce a plasma, neutral gas must be present at an appropriate density in the vicinity of the electrodes of the magnetized plasma gun at the time that high voltage is applied

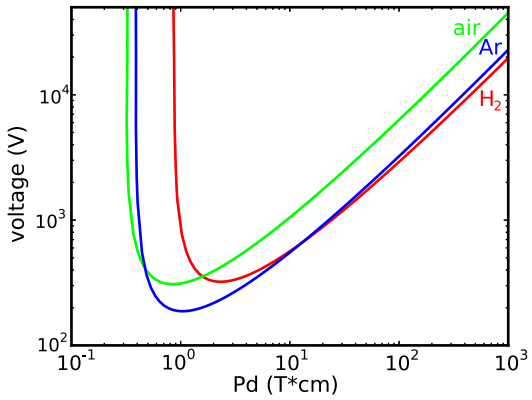

Figure 2.3: Paschen curves for hydrogen, argon, and air

across the electrodes. (In most cases, this is equivalent to the gas being in the vicinity of the arched vacuum magnetic field lines that stretch from one gas nozzle to another.) This requirement is known as the Paschen criterion. More precisely, it states that the voltage required for breakdown is a function of the product Pd where P is the pressure of the gas and d is the distance between the electrodes. This function has the form

$$V_{min}(Pd) = \frac{BPd}{\ln(Pd) + C} \tag{2.1}$$

where B and C are constants that are different for different species of gas [10]. Examples of Paschen curves are shown in Figure 2.3.

In order to satisfy the Paschen criterion without filling the chamber with neutral gas (in opposition to the goal of letting the plasma evolve into a vacuum), gas is supplied to the gun by means of two fast gas valves powered by a pulsed power supply.

Figure 2.4a shows a diagram of the gas valve interior. When the gas valve is closed, the aluminum diaphragm is held against the o-ring underneath it by a combination of the spring and the "back pressure" of the gas supplied to the valve. Gas can flow around the diaphragm into the plenum, but not into the outgoing gas line. To open the valve, a current pulse from the power supply is sent through the coil of wire, inducing a mirror current in the diaphragm and generating a repulsive force

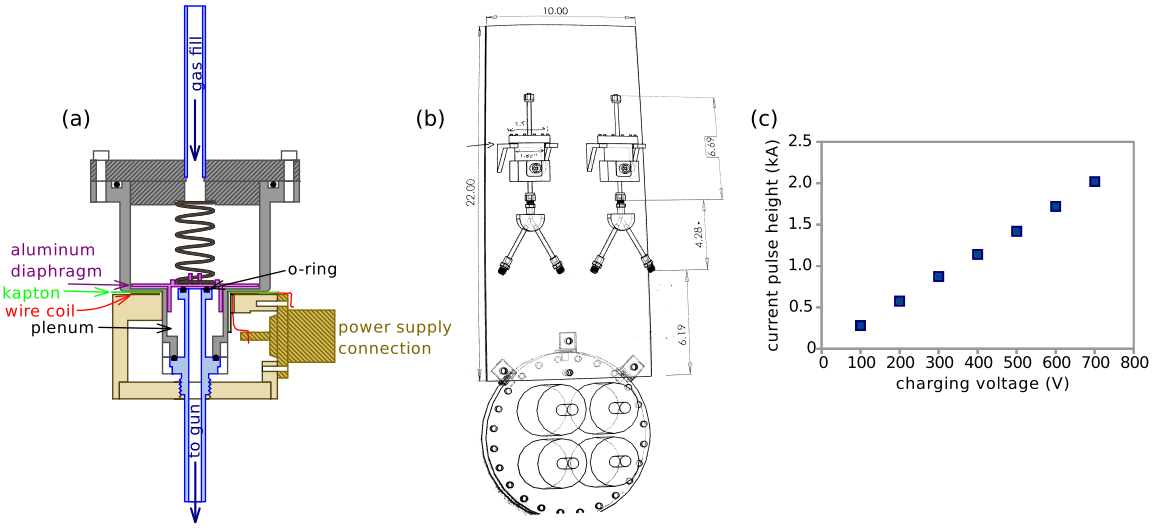

Figure 2.4: a.) Interior structure of a gas valve (adapted from a CAD drawing by Paul Bellan and used with permission). b.) Wire frame view of the new valves, splitters, and mounting arrangement. (Gas lines connecting the splitters to the gun are not shown.) c.) Gas valve power supply output current pulse height versus charging voltage

between the two. The diaphragm jumps up, opening the valve briefly before the spring and/or back pressure pushes it closed again. Gunsu Yun estimated that about one fifth of the molecules in the plenum escape [30], but this depends on the species of the gas and the back pressure.

In 2006, two gas valves of the design in Figure 2.4a were installed on the quad gun, in place of the single older model valve put in by Hansen. The new setup, shown in Figure 2.4b, makes it possible for two different species of gas to be used to make the same plasma, either as two halves of the same loop (Chapter 3) or as two single-gas loops, one of each species (Chapter 5).

The new gas valve power supply, built by Dave Felt, allows the two valves to be triggered individually, so as to accommodate the different sound speeds of different neutral gases and, hence, different travel times between the valves and the gun. It contains two 50 μF capacitors, one for each valve; both charge off a single charging supply, but a second supply could be added to allow the valves to be triggered from different voltages. Shreekrishna Tripathi measured the current pulse height as a function of charging voltage and found it to be very linear (Figure 2.4c). Rory Perkins measured the total amount of neutral gas released per valve per pulse, and found it to be about half that of the previous valve that supplied all four nozzles[5].

More details about gas valve operation can be found in Appendix B.

2.2.4 Main power system

High voltage is supplied from a 59 μF capacitor that is charged to 3–6 kV, then connected to the electrodes via a krytron-switched ignitron and low-inductance cables. The preset timing program ensures that the resulting electric field is set up only after the vacuum magnetic field has been established and neutral gas is present in the vicinity. (An extended description of the timing system, which is shared with the spheromak experiment, is given by Yun [30].)

Breakdown occurs by means of the electron avalanche process discussed in the previous section. This process occurs over one to several microseconds and varies from shot to shot, creating a "jitter" in the time between the application of high voltage and the sequence of steps in the plasma's evolution (which in most cases is very repeatable once initiated). The capacitor then acts as a current source [31], driving a current through the resulting plasma structure (among other paths). A detailed discussion of the current and voltage profiles can be found in the next section.

[5]This measurement was taken at back pressures of 60 psi for argon and nitrogen and 100 psi for hydrogen. It may be different for different back pressures. Moreover, the total gas released is not necessarily proportional to the density of the plasma structure. Both of these topics are discussed in Appendix B.

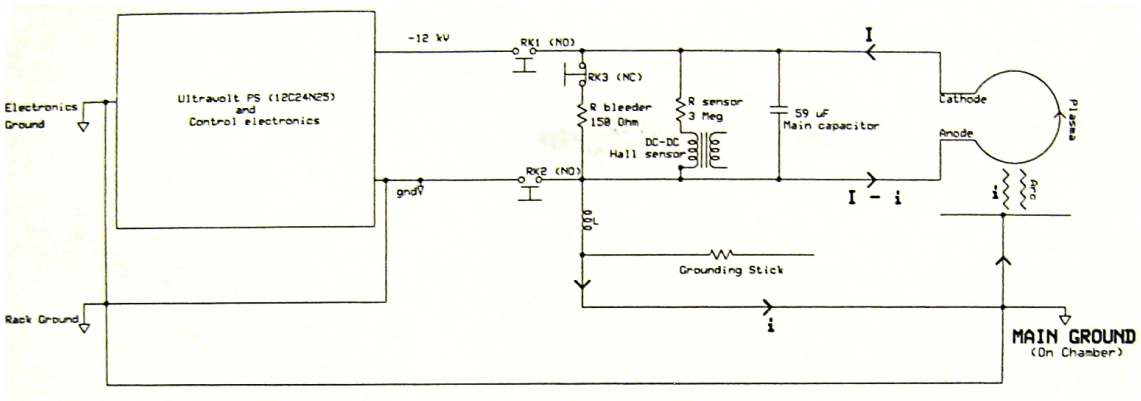

Figure 2.5: Main power system grounding setup, as updated in 2005. (diagram by Dave Felt and Shreekrishna Tripathi; used with permission)

The main power system was repaired/improved in 2005 by Dave Felt and Shreekrishna Tripathi after a short developed in the high-voltage charging supply. An Ultravolt 10 kV supply was installed in place of the faulty unit, and the grounding of the experiment was updated to the setup shown in Figure 2.5.

2.3 Diagnostics

2.3.1 System overview

The vacuum chamber is outfitted with a suite of diagnostics, many of which can be used for either the solar gun or the spheromak gun. Those that are featured prominently in this dissertation are described in detail below. Other available systems include (but are not limited to):

- a 12-channel, high-resolution ($\sim$ 5 pm/pixel) spectroscopic system [30];
- a set of four x-ray photodiodes, three of which are filtered for specific energy ranges (15–62 eV, above 83 eV, above 200 eV) [32];
- a VUV (vacuum ultraviolet) to soft x-ray (SXR) pinhole camera [31];
- an array of broadband EUV (extreme ultraviolet) vacuum photodiodes [32];
- and a heterodyne interferometer (not yet used for the solar experiment, due to the current vacuum port configuration) [31].

Many of these systems are connected to a VME data acquisition system[6], which has 96 channels and is typically run at a 100 MHz sampling rate. Once started, the system takes data continuously until it receives a "stop" signal, at which point it reports the most recent 2^{17} samples per channel with a range of 12 bits per sample — i.e., the last 1.3 ms. Thus, the VME can be triggered off the main timing system used for experiment triggers and still capture all of the data (and more), regardless of the microsecond jitter due to breakdown variation.

Other diagnostics that are more sensitive to that jitter, such as the spectrometer and various imaging systems, were triggered off a second, parallel timing system. This system is a clone of the first, but is initiated by light from a collimator aimed at the electrodes, allowing the diagnostic timing system to be triggered by the formation of the plasma itself. For nearly all applications (the exceptions being studies of the very early times in plasma formation before emission is high enough to trigger the collimator), this is preferable because it allows data from one shot to be almost perfectly synchronized or given a predetermined offset relative to the data from another shot.

2.3.2 Current and voltage

The high-voltage capacitor is equipped with a Rogowski coil that was used to measure its output current. A Tektronix P6015 high-voltage probe was used to measure the voltage across the electrodes. The current and voltage signals were then transmitted to the VME through an optical transmitter and receiver[7], for purposes of electrical isolation.

Sample data are shown in Figure 2.6 for a 4 kV, single-loop hydrogen plasma. Note that the voltage trace has a near-constant slope during the lifetime of the plasma loop (the 5 μs or so after breakdown). This feature is an artifact of an isolation transformer in the circuit between the optical receiver and the VME; this element was added to eliminate a ground loop but resulted in performance limitations at lower frequencies [32]. In fact, the voltage remains nearly constant during this time period. This was demonstrated by Xiang Zhai, who recently built a new high-voltage probe that is optically coupled and totally isolated from earth ground.

Because the capacitor acts as a current source, currents during early times tend to be the same to within 10 percent, even for different species; an example of this is shown in Figure 2.7. There are indications, however, that most of this current does not actually flow through the bright, clearly defined plasma structure.

[6]Components of the VME system are: eight 12-channel DAQ boards (SiS GmbH SIS3300), one control board (SIS3820), and accompanying computer control code that interfaces with IDL.

[7]Model: Analog Modules, part number 732T-2.5-33K-10M

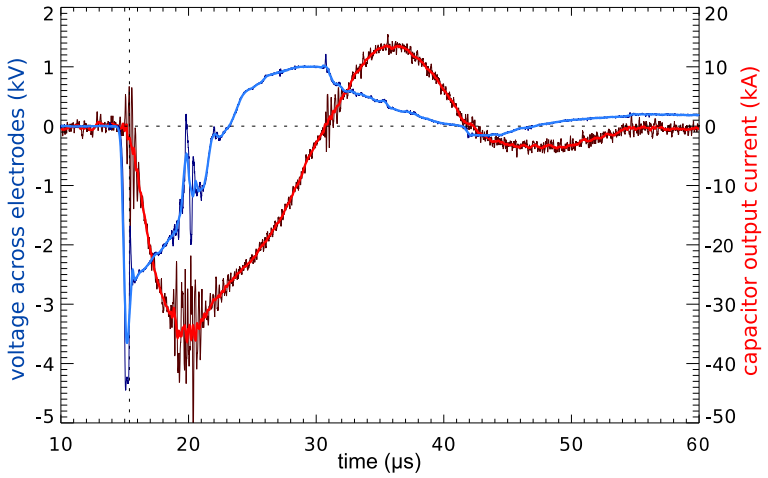

Figure 2.6: Sample IV data for a 4 kV single-loop hydrogen plasma. Smoothed current and voltage traces are shown in light red and light blue, respectively, while unsmoothed traces are shown in the darker colors. Smoothing was done with a boxcar average. The vertical dashed line indicates breakdown time, according to the optical collimator signal. Time is given relative to the entire VME data set. *(shot 9090)*

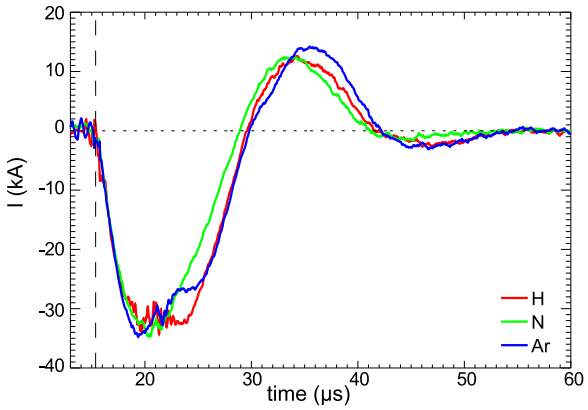

Figure 2.7: Smoothed current traces for hydrogen, nitrogen, and argon single-loop plasmas fired from 4 kV. *(shots 5770, 5932, and 5788)*

Magnetic measurements of single plasma loops (detailed in Chapter 4) find the magnetic field peak magnitude to be 0.1–0.2 T, with the "sine-like" components peaking at 200–350 G. Ampere's law tells us that at the edge of a current channel of radius A,

$$B_{azimuthal} = \frac{\mu_0 I}{2\pi A} = 1750 \text{ to } 3500 \text{ G} \tag{2.2}$$

for $I = 35$ kA and $A = 2$–4 cm. This implies that only about one tenth — and at most one fifth — of the total current output from the capacitor flows through the loop. Similar values can be calculated from magnetic measurements of the spheromak gun plasmas [33, 31], which are measured with a different set of diagnostics.

The hypothesis that only a fraction of the capacitor current flows through the plasma loop is also consistent with the continued ringing of the current even after that loop detaches or is otherwise disrupted. (The elimination of that current path — with its associated resistance and inductance — does not typically appear to impede the overall current flow, nor correspond to an increase in the magnitude of the voltage across the electrodes.) Calculations for the change in magnetic flux due to plasma loop expansion also suggest loop currents on the order of kA, rather than tens of kA (Appendix C).

Somewhat surprisingly, though, the highly consistent scaling of loop evolution with output current (which will be discussed in Chapter 3) seems to suggest this fraction is consistent across different plasma species and different output currents.

2.3.3 Magnetic probe array

The principle of a "B-dot" probe is straightforward: when the magnetic flux Φ through the center of a coil of wire changes, an electromotive force $\mathcal{E}$ is induced in the coil according to Faraday's law:

$$\mathcal{E} = -N\frac{\mathrm{d}\Phi}{\mathrm{d}t} = -N\frac{\mathrm{d}}{\mathrm{d}t}\int_S \mathbf{B}\cdot\mathrm{d}\mathbf{A} \tag{2.3}$$

where N is the number of turns in the coil, S is the surface encompassed by a turn, and $\mathbf{B}$ is the magnetic field through the infinitesimal section of that surface $\mathrm{d}\mathbf{A}$. If S is flat and small enough relative to the scale of the magnetic field that $\mathbf{B}$ is approximately constant over the entire surface, then this reduces to

$$\mathcal{E} = -NA\frac{\mathrm{d}B_\perp}{\mathrm{d}t} \tag{2.4}$$

which can be integrated to find $B_\perp(t)$, the time-dependent component of the magnetic field perpendicular to the coil surface, as a function of $\mathcal{E}(t)$.

Hence, by integrating the voltage measured across the ends of a tiny coil past which a plasma is passing with its frozen-in flux (therefore causing the coil to "see" a changing flux), one can measure the plasma magnetic field normal to that coil. By using three orthogonal coils, one can measure the three-dimensional magnetic field.

A 12-channel probe array was built, installed, and calibrated by Shreekrishna Tripathi, using commercial chip inductors, based on the design by Carlos Romero [34]. The 12 channels are arranged in four clusters of orthogonal triplets, mounted in a plastic tube, which is then housed in a 1 cm quartz tube. This assembly is attached at a 90 degree angle to a metal tube extending from the same end dome as the gun. (This setup allows the probe array to be moved in toward or away from the electrode, as well as rotated in the plane parallel to the electrode.) The signals from the inductors are conveyed to the VME via BNC cables, and thence to the IDL routine that integrates them numerically.

Figure 2.8 provides several views of the magnetic probe array and its orientation relative to the electrode. In order to calculate the probes' location in space, one must also know:

- that the probe arm rotation point is located 43.7 ± 0.4 cm from the center of the electrodes, at a 23 degree angle below horizontal[8], and
- how far from the electrode the probe arm is extended.

The vacuum fittings for the metal tube and the curvature of the end dome limit the probe's travel toward the electrode; the closest it can get is 9.5 cm. It can be moved out away from the electrode many tens of centimeters, and/or rotated up and out of the plasma entirely.

The three orthogonal directions measured by the probe array system are B_r, B_θ, and B_z, using the natural cylindrical coordinate system of the rotating probe arm. (One must be careful, however, not to confuse these with the coordinates relative to the cylindrical symmetry of the chamber.) Since the $r\theta z$ coordinate system rotates with the probe arm, it is preferable to express measured magnetic fields in terms of the Cartesian coordinate system with its origin at the center point of the electrodes, z pointing into the chamber, and x and y being the horizontal and vertical axes, respectively. The magnetic fields measured by the probes in cluster n are then written

[8] This is due to vacuum port positioning, not just a desire to have as little symmetry as possible.

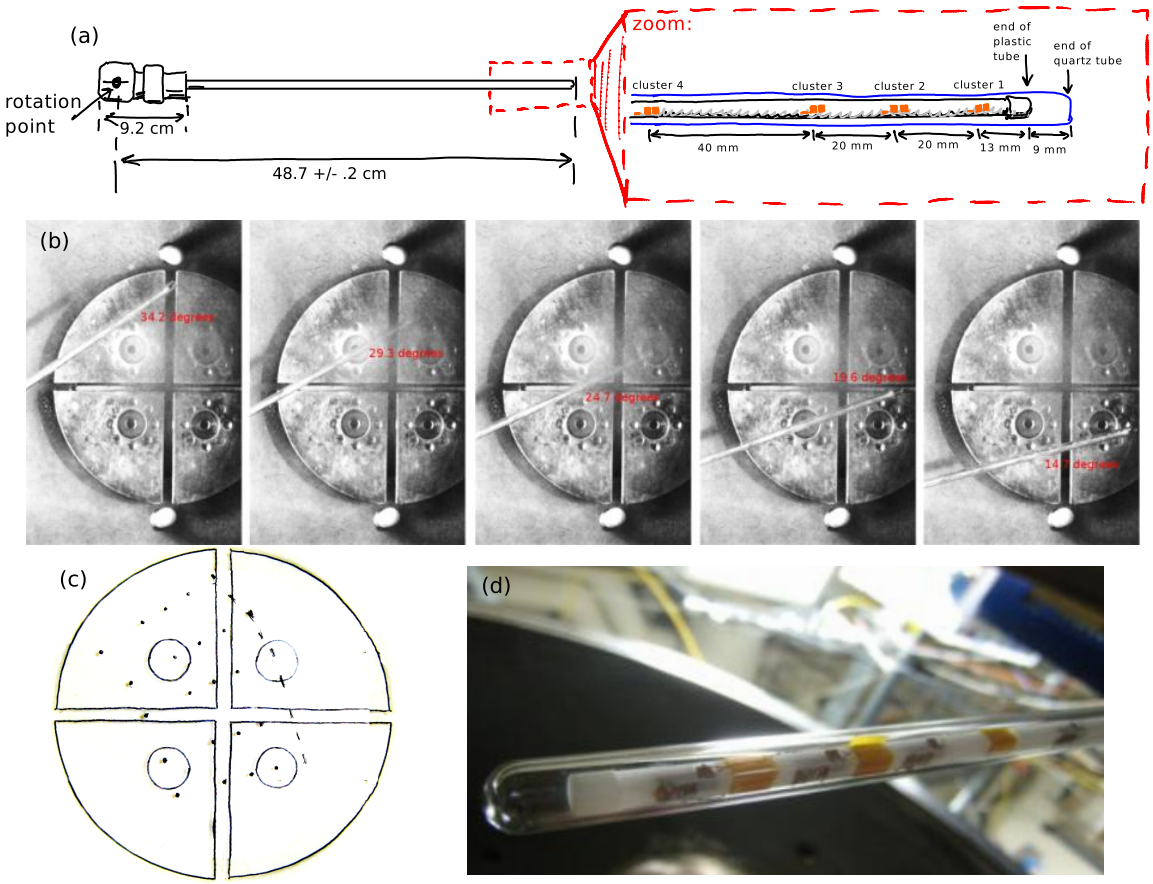

Figure 2.8: Views of the magnetic probe array. a.) Artist's rendering showing the length of the probe arm and the locations of the coils at the end of the arm. b.) Five standard positions for the probe array, ranging from about 15 to 29 degrees above horizontal, as viewed from the window on the opposite end dome. c.) For each of those five positions, probe locations (dots) and the end of the arm (dashed line) are projected onto an outline of the electrodes. d.) Closeup of the end of the probe, viewed from below during a vacuum break. (The orange bands located between the probe clusters are pieces of tape.)

$$
\begin{aligned}
B_{xn} &= B_{rn}\cos\theta - B_{\theta n}\sin\theta \\
B_{yn} &= B_{rn}\sin\theta + B_{\theta n}\cos\theta \\
B_{zn} &= B_{zn}
\end{aligned}
\tag{2.5}
$$

where θ is the angle of inclination from horizontal. These measurements are associated with location

$$
\begin{aligned}
x_n &= -40.2 + l_n\cos\theta \\
y_n &= -17.2 + l_n\sin\theta \\
z_n &= z > 9.5
\end{aligned}
\tag{2.6}
$$

where distances are in centimeters and l_n = [46.3, 44.3, 42.3, 38.3] is the distance from the rotation point of the arm to the midpoint of cluster [1, 2, 3, 4], respectively.

2.3.4 Imaging

Because the plasma lifetime is only on the order of microseconds, meaningful images can only be captured with ultra-high-speed cameras. Three cameras were employed for this work:

Imacon 200: This camera[9] uses an eight-way optical beam splitter to send incoming light to eight high-resolution microchannel plate image intensifiers, each gated with high-speed electronics and coupled to a CCD. Exploitation of a fast charge transfer process allows each intensified CCD to record a second image in quick succession, allowing the system to capture up to 16 frames in less than a microsecond. The images have a 10-bit dynamic range and a 1200 x 980 resolution.

Princeton Instruments cameras: These two identical single-frame, Peltier-cooled gated ICCD cameras[10] are mounted on the same stand, perpendicular to one another. Placing a 50/50 beam splitter at the intersection of their lines of sight enables two captures of the plasma from a single perspective. (This can be used to take simultaneous images using different optical filters, or for creating a two-frame "movie".) Alternately, placing a mirror a few inches offset from the intersection creates parallel lines of sight that can be used to generate 3D pictures. The images have a 16-bit dynamic range and a 576 x 384 resolution.

[9] DRS Technologies

[10] Detector model: ICCD-576-G/RB-E (CCD made by EEV). Controller model: ST-138

wavelength (nm)	bandwidth (nm)	transmission (%)
400	10	50
480	10	46
485	10	50
656.5	1.2	45

Table 2.1: Commonly used static optical filters

Due to its ability to capture short movies of each individual plasma shot, the Imacon is the workhorse[11] of the Bellan plasma lab's main experiment chamber. It is not particularly suitable for quantitative studies, though, due to its signal-to-noise ratio and a variable relative gain among the CCDs that is different each time the camera is powered up. For quantitative measurements, the Princeton cameras' low noise and high dynamic range are ideal; they are also often deployed to capture a second perspective of the plasma in addition to Imacon view.

Typical imaging is done with exposure times of 10–100 ns (depending what lens and whether any optical filters are being used) and an interframe time of 200–400 ns.

2.3.5 Dual-gas plasmas

Creating a plasma from two different species of neutral gas has turned out to be a valuable diagnostic technique. Because different atoms have different atomic transitions, optical filters can be used to selectively image the different plasma species, enabling different sections of the plasma to be tracked from frame to frame. Furthermore, because the experiments are highly reproducible, filtered and unfiltered images can be taken of separate shots and then used together. Figure 2.9 illustrates this with an Imacon frame from three different shots, two with optical filters.

In addition to the static filters listed in Table 2.1, the recent purchase of a VariSpec liquid crystal

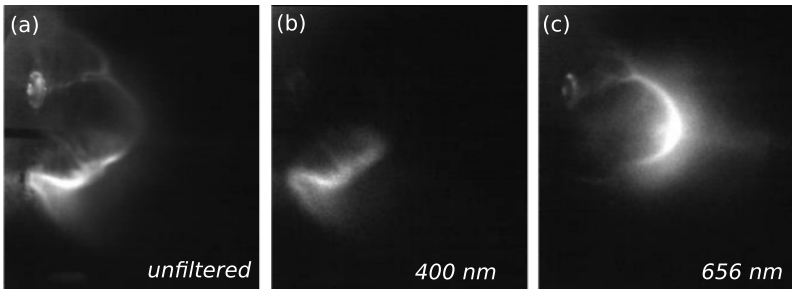

Figure 2.9: Unfiltered, 400-nm-filtered, and 656-nm-filtered images of nitrogen/hydrogen single loops. *(shots 5019, 5027, 5024)*

[11] a purebred workhorse

tunable filter with a 7 nm bandwidth enables a filtered image to be obtained for any wavelength in the visible range.

2.4 Software

As mentioned previously, IDL plays a key role in the acquisition, processing, analysis, and presentation of data from the VME. It has been used to write programs for several other tasks related to the plasma experiment.

2.4.1 Calculations of magnetic field lines

Because the topology of the vacuum magnetic field generated by the gun has such an incredibly important role in the dynamics of the plasma, and because the gun can be operated with such a variety of coil configurations, a program was written that calculates magnetic field lines due to the presence of one or more circular current-carrying wires.

The user specifies the number, radius, current, and locations[12] of the wire hoops, as well as the starting points for any magnetic field lines that are to be drawn. The paths of the field lines are then calculated via the fourth-order Runge-Kutta method[13] [35]:

$$\mathbf{s}_{n+1} = \mathbf{s}_n + \frac{h}{6}(\mathbf{k}_1 + 2\mathbf{k}_2 + 2\mathbf{k}_3 + \mathbf{k}_4) \tag{2.7}$$

where $\mathbf{s}_n$ and $\mathbf{s}_{n+1}$ are adjacent points along the field line, h is the step size between adjacent points, and $\mathbf{k}_1$ through $\mathbf{k}_4$, defined as

$$\begin{aligned}
\mathbf{k}_1 &= \frac{\mathbf{B}(\mathbf{s}_n)}{|\mathbf{B}(\mathbf{s}_n)|} \\
\mathbf{k}_2 &= \frac{\mathbf{B}(\mathbf{s}_n + \frac{h}{2}\mathbf{k}_1)}{|\mathbf{B}(\mathbf{s}_n + \frac{h}{2}\mathbf{k}_1)|} \\
\mathbf{k}_3 &= \frac{\mathbf{B}(\mathbf{s}_n + \frac{h}{2}\mathbf{k}_2)}{|\mathbf{B}(\mathbf{s}_n + \frac{h}{2}\mathbf{k}_2)|} \\
\mathbf{k}_4 &= \frac{\mathbf{B}(\mathbf{s}_n + h\mathbf{k}_3)}{|\mathbf{B}(\mathbf{s}_n + h\mathbf{k}_3)|}
\end{aligned}$$

[12] The hoops' axes of symmetry are all oriented in the same direction, though if there were a need for arbitrarily oriented hoops, this could easily be modified. A stack of coaxial loops can be used to estimate the field of a coil.

[13] The method is implemented just as it is written, rather than used via the IDL routine, due to the programmer's lack of knowledge at the time about how to optimize one's code.

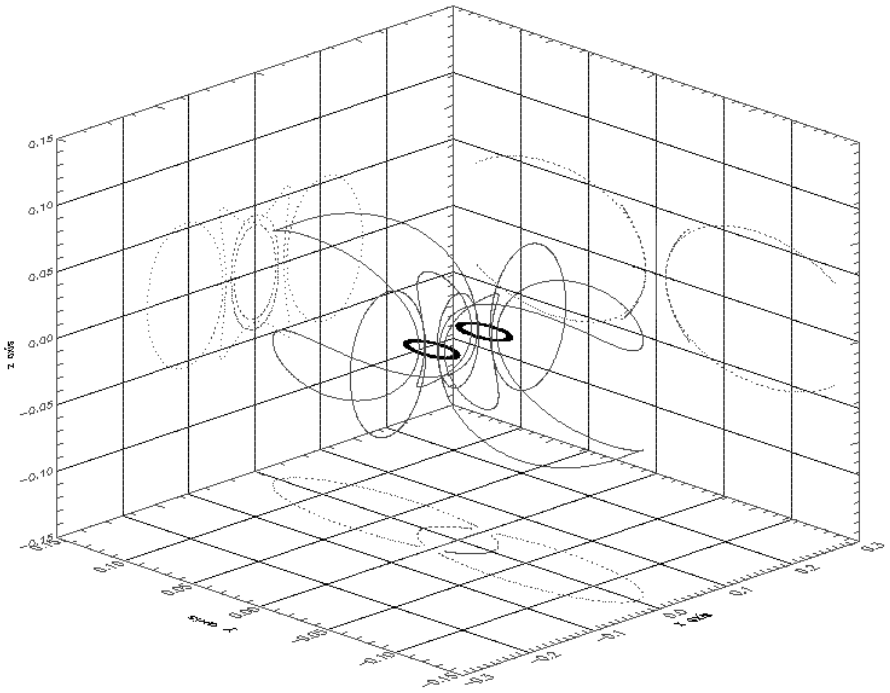

Figure 2.10: Magnetic field due to a pair of adjacent wire hoops carrying oppositely directed currents

are essentially "samples" of slopes in the vicinity of the direction the magnetic field is going (of which a weighted average is taken for the actual "jump" to the next point).

The program successfully produces closed field lines for reasonable step sizes. These can then be plotted in such a way as the user finds enlightening, projected onto various planes, and so on. Figure 2.10 shows an example for a pair of adjacent coils.

2.4.2 Loop-tracing

In order to quantify and compare the evolution of individual plasma loops, IDL routines were written to facilitate image tracking of the loop axis. One routine displays each image in the series taken by the Imacon camera, asks the user to trace out the location of the axis, and records the resulting mouse clicks. Figure 2.11 shows a typical set of traced loop images.

The resulting coordinate locations are then converted to distances based on the 8 cm footpoint spacing and the camera viewing angle (which can be calculated from the aspect ratio of the electrodes). The loop is assumed to be in the vertical plane perpendicular to the electrodes. Appendix D examines the systematic error inherent in this assumption, as well as other potential sources of uncertainty and variation in the loop trace data.

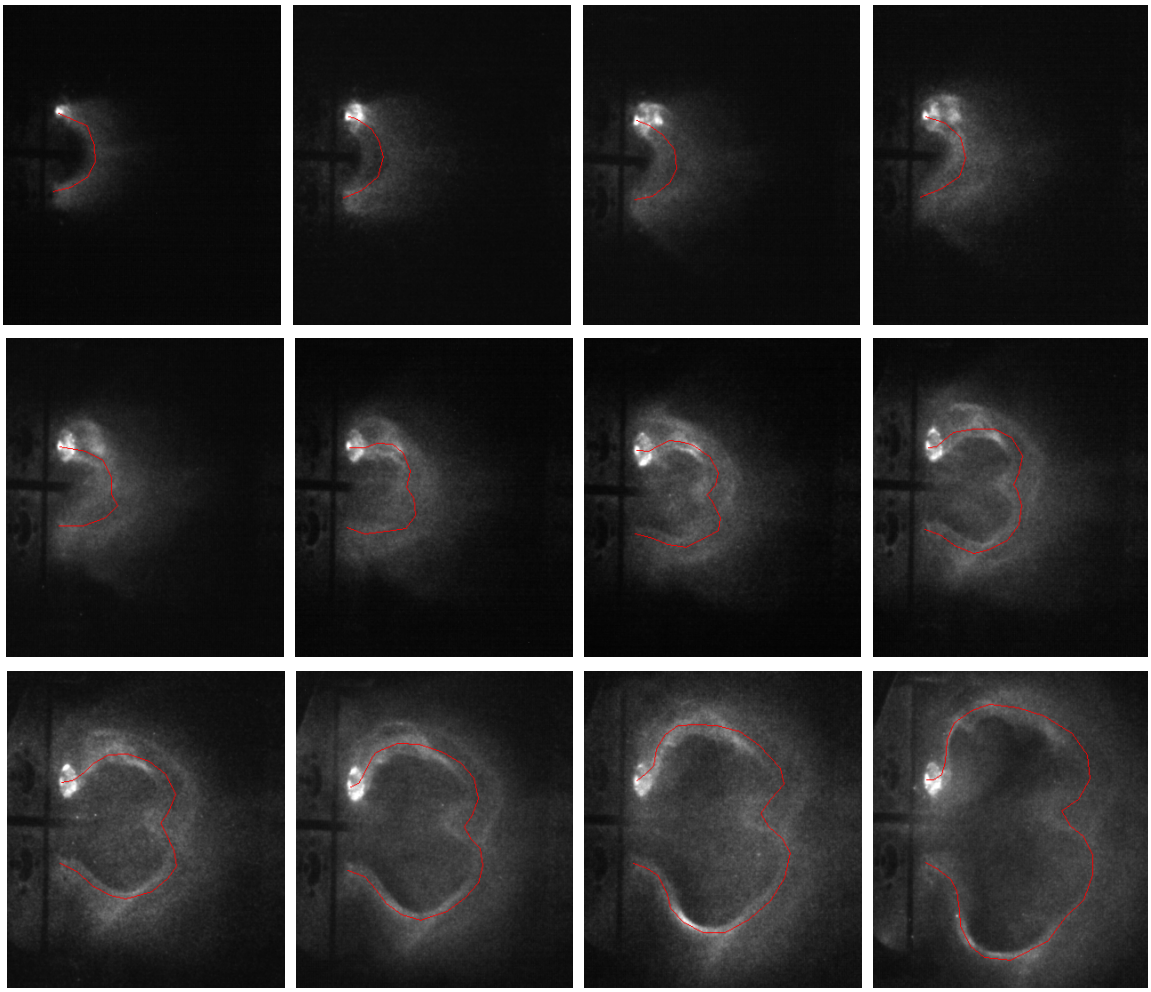

Figure 2.11: Sequence of traced plasma loop images. *(shot 9090)*

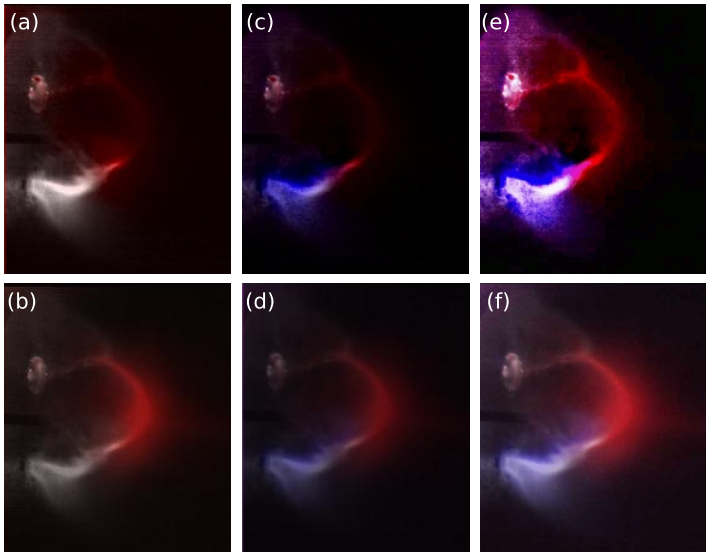

Figure 2.12: The same shots from Figure 2.9, illustrating various image combination methods. First, the red-filtered shot was a.) subtracted from or b.) averaged with an unfiltered shot. Next, both the red- and blue-filtered shots were either c.) subtracted from or d.) averaged with the unfiltered shot. Finally, since averaging or subtracting multiple shots darkens images, the examples from (c–d) were brightened in the GNU Image Manipulation Program to yield the images in (e–f), respectively.

2.4.3 Image processing

IDL was also used to create color images of the plasma from the grayscale camera photos, via color composites, color tables, and various scaling schemes for each of these.

Composites were made from two or more images taken with or without different optical filters, as was done for the dual-gas plasmas in Figure 2.9. There are infinitely many different ways the matrices of pixel values representing the images can be combined. Some of the more useful examples include (in no particular order)

- colorizing an unfiltered image with a filtered image by subtracting the filtered image from one or more of the color channels of the unfiltered image (where the latter was converted to, say, a black and white RGB image),
- combining the same two images by averaging the filtered image with one or more of the channels of the black and white image,
- using one of the above methods, but with one unfiltered and two or more filtered images,
- not using any unfiltered images, but combining multiple unfiltered images by assigning them to different color channels of a “blank” image,

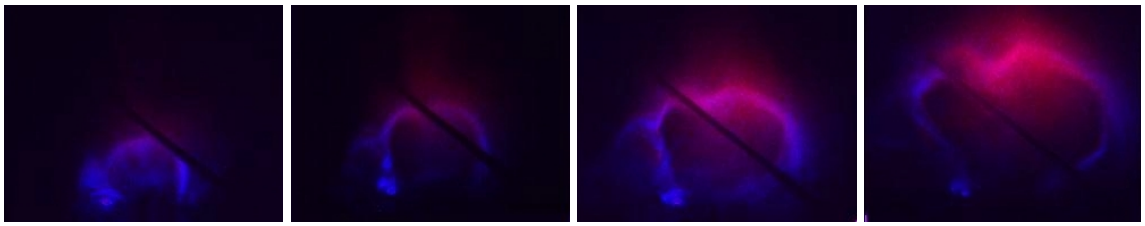

Figure 2.13: A composite of two filtered images of a hydrogen loop, using the H-alpha and H-beta filters. *(shots 5778 and 5780)*

- using weighted averages or otherwise scaling matrices depending on how bright the source images are,

and many more. Some examples are shown in Figure 2.12. Of course, the same techniques can also be applied to multiple images of single-species plasmas taken at various wavelengths, such as the hydrogen loop in Figure 2.13.

While quantitative studies with the Princeton camera have been done, in which pixel values are measured precisely and emission ratios are estimated based on the properties of the different filters that were used, making composite images is usually a matter of finding the most suitable settings to faithfully and effectively communicate the information about the plasma contained in the camera images. Different image combination methods may highlight different parts of that information, while both still being valid.

Even when only unfiltered images have been taken of a particular plasma, there are image processing questions such as how best to translate the 10 or 16 bits of data per pixel into the 8 bits of a standard image. One can use linear scaling or logarithmic scaling. One can use the entire range of data or scale to the middle 90 percent of the pixels (setting the brightest five percent to white and

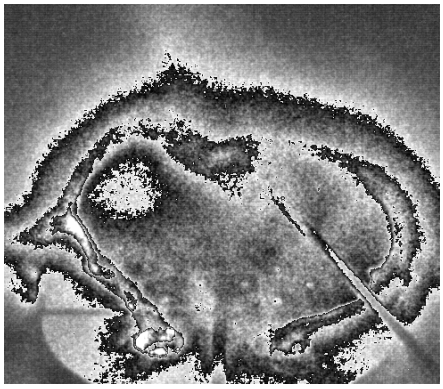

Figure 2.14: A 10-bit Imacon image: informational but in need of interpretation *(shot 5770)*

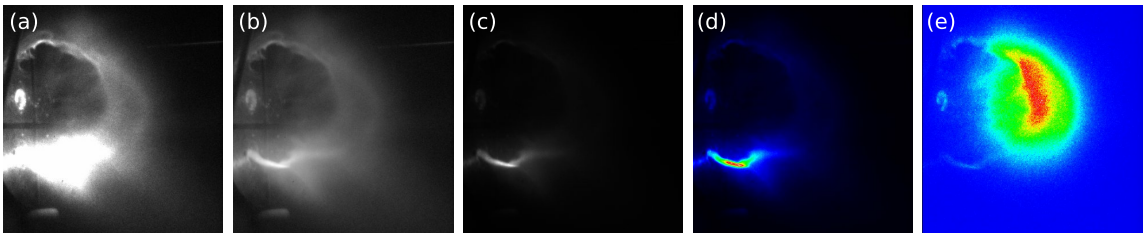

Figure 2.15: Views of the same hydrogen/argon plasma with a.) 5%/95% linear scaling, b.) logarithmic scaling, c.) full range linear scaling, d.) full range linear scaling plus a color table, and e.) the red filter on the second Princeton camera plus full range linear scaling plus a color table. *(shot 5214)*

the darkest five percent to black). One can also apply color tables. Different methods result in an image that enhances or suppresses different parts of the plasma, as illustrated in Figure 2.15.

In addition to IDL and the various programs associated with laboratory instruments (such as the Princeton and Imacon cameras), additional software that has been used to prepare and present the data in this dissertation includes:

- the GNU Image Manipulation Program
- Inkscape
- QCAD, Solidworks, SketchUp
- Mathematica
- LibreOffice, OpenOffice, Microsoft Office
- QtiPlot
- Python and various key libraries (e.g., matplotlib and numpy)
- MikTeX and TeXLive LaTeX 2_ε distributions

Chapter 3

Plasma flows in arched magnetic flux tubes due to MHD forces

"Shield generators?"

"Online."

"Plasma flow?"

"Stable."

"Lunch?"

"Salami sandwiches."

— exchange between Chakotay and Harry Kim (*Star Trek Voyager*)

Magnetic flux tubes are important features in a diverse range of plasma environments, from the solar atmosphere to the interior of a tokamak. The quad gun, operated in "single-loop" mode, produces individual arched flux tubes that are highly reproducible, thereby facilitating quantitative investigations. They are also, unless sufficiently constrained by a strapping field[1] [27], highly dynamic.

The outstanding feature of the dynamics is a dramatic increase in the total length of the flux tube, during which the minor radius of the tube and the plasma density remain relatively constant. The corresponding increase in particle number is, it turns out, made possible by bulk flows that accelerate plasma into the tube from both ends; "color-coded" dual-gas plasmas have shown that the two flows are independent.

Flow speed depends on local mass density ρ and electric current through the plasma. These findings are quantitatively consistent with two interrelated MHD models: the hoop force (which ex-

[1] A strapping field is an overarching, externally generated magnetic field. "Overarching" means that in the Cartesian coordinate system where the plasma arch is in the yz plane, the strapping field would be in the direction of $\pm x$.

plains the lengthening) and the gobble effect (which explains the flows). These forces are expected to drive plasma acceleration in other open flux configurations with arched geometries, such as those found on the solar surface.

This chapter begins with the models, then presents the experimental results, and concludes by putting them all together.

3.1 Model 1: Simplified hoop force model

The "hoop force" — the outward force experienced by a curved, current-carrying flux conserver — is a well-known phenomenon in plasma physics; at least, it is one that second year graduate students in the field are expected to know [36]. It is also a significant concern for anyone working with high current coils, such as the superconducting coils of NMR magnets [37], superconducting magnetic energy storage systems [38], or advanced magnetic confinement fusion technology [39].

Intuitive explanations for the hoop force typically invoke the repulsive force experienced by antiparallel straight wires and/or the concept of a "magnetic pressure" proportional to the square of the magnetic field strength [40, 1]. The analytic expression can be derived elegantly for a toroid via an energy minimization argument, originally devised by Shafranov [41]. Although this derivation assumes magnetic flux to be perfectly conserved (which is not true for experimental plasma loops), comparisons to alternate derivations for loops of other shapes and aspect ratios show that the expression is quite robust.

If one makes a few simplifying assumptions about the plasma loop characteristics, the hoop force can be described by a second-order differential equation. For certain conditions of interest, this equation has an analytic solution that predicts characteristics of experimental loops.

3.1.1 Derivation for a perfectly conducting circular hoop

The energy of a current-carrying hoop is given by

$$U = \frac{LI^2}{2} = \frac{\Phi^2}{2L} \tag{3.1}$$

where Φ is the total magnetic flux enclosed by the hoop, I is the current through the hoop, and $L \equiv \Phi/I$ is the hoop's self inductance. Ultimately, the hoops of interest will be made of plasma, but for now I will use the term "wire" as a general description.

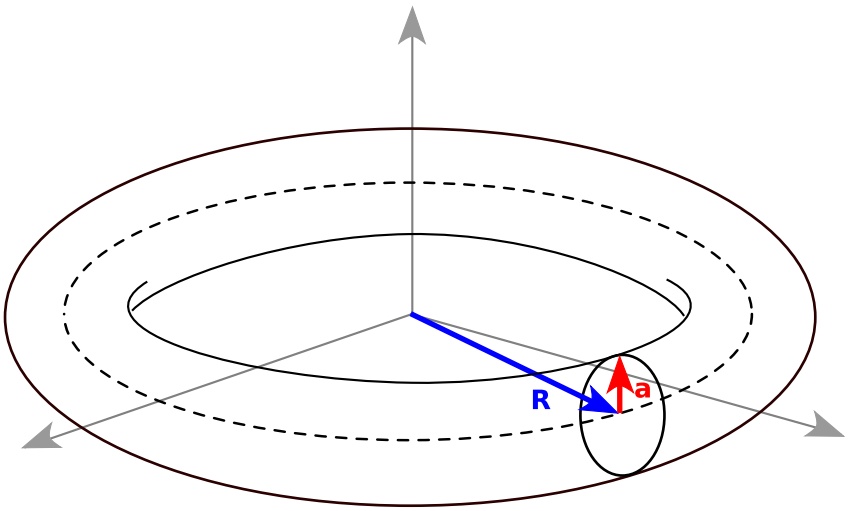

Figure 3.1: A circular hoop with a circular cross section

If the wire is a perfect conductor, it takes no work to move a charge around the hoop, and the electromotive force $\mathcal{E}$ is identically zero. Then, by Faraday's law of induction, the flux through the hoop is constant:

$$\frac{\mathrm{d}\Phi}{\mathrm{d}t} = -\mathcal{E} = 0. \tag{3.2}$$

The total radial force on the hoop can be expressed as the ratio between the infinitesimal decrease in energy due to an infinitesimal increase in the hoop radius R and that infinitesimal displacement:

$$F_{\Sigma hoop} = -\frac{\partial U}{\partial R} = -\frac{\Phi^2}{2}\frac{\partial}{\partial R}\left(\frac{1}{L}\right) = \frac{\Phi^2}{2L^2}\frac{\partial L}{\partial R} = \frac{I^2}{2}\frac{\partial L}{\partial R} \tag{3.3}$$

where the assumption that Φ is constant has been employed. Note that this force is distributed along the entirety of the hoop's circumference; the force per unit length is $F_{hoop} = F_{\Sigma hoop}/2\pi R$.

In the case of a circular hoop with major radius R and minor radius $a \ll R$, the inductance L is given by

$$L = \mu_0 R\left(\ln\left(\frac{8R}{a}\right) - 2 + Y\right) \tag{3.4}$$

where μ_0 is the permeability of free space and $l_i = \mu_0 Y/2\pi$ is the internal inductance per unit length, a constant that depends on how the current is distributed within the wire [41]. In straight wires, if the current is uniformly distributed, $Y = 1/4$; if the current flows entirely on the surface

of the wire, $Y = 0$.[2]

For all $R > a$, L increases monotonically.

$$\frac{\partial L}{\partial R} = \mu_0 \left(\ln\left(\frac{R}{a}\right) + 1.08 + Y \right) \tag{3.6}$$

Hence, the hoop force causes the wire loop to expand. [3]

3.1.2 The "contradiction" of time derivatives

At what rate does the hoop force cause the loop to expand? (This question must be answered for the experiment analysis, in order to compare the relative effects of the hoop force and the axial flows as loop size increases.)

To approach the problem, start with the definition of inductance $L \equiv \Phi/I$, multiply by I, and take the derivative with respect to time.

$$\Phi = LI \tag{3.7}$$

$$\frac{\mathrm{d}\Phi}{\mathrm{d}t} = L\frac{\mathrm{d}I}{\mathrm{d}t} + I\frac{\mathrm{d}L}{\mathrm{d}t} \tag{3.8}$$

If flux is, in fact, conserved, the left side of the equation is zero, and the change in inductance (whose relation to radius has already been established in equation (3.4)) can be expressed as

$$\frac{\mathrm{d}L}{\mathrm{d}t} = -\frac{L}{I}\frac{\mathrm{d}I}{\mathrm{d}t}. \tag{3.9}$$

Meanwhile, using the chain rule, $\mathrm{d}L/\mathrm{d}t$ can be rewritten as

$$\frac{\mathrm{d}L}{\mathrm{d}t} = \frac{\mathrm{d}L}{\mathrm{d}R}\frac{\mathrm{d}R}{\mathrm{d}t}. \tag{3.10}$$

Combining the last two equations produces an analytical expression for the rate at which the hoop

[2] In general, one can calculate l_i by equating two expressions for the magnetic energy inside the wire

$$\frac{1}{2} l_i I^2 = \iiint_{\text{wire volume}} \frac{B^2}{2\mu_0} dV \tag{3.5}$$

where the magnetic field B, of course, depends on the current distribution.

The derivation for Equation 3.4 is interesting but nontrivial [42, 43].

[3] Note that this calculation is for the hoop force alone. Other forces that can balance an outward-directed hoop force, such as those caused by magnetic field line tension and an externally applied strapping field (if one is present), are not included. Nor are other outward-directed forces considered, such as the pressure-driven "tire tube force" [40].

force alone is expected to expand the plasma loop:

$$\frac{\mathrm{d}R}{\mathrm{d}t} = -\frac{\frac{\mathrm{d}I}{\mathrm{d}t}}{I}\frac{L}{\frac{\mathrm{d}L}{\mathrm{d}R}} \tag{3.11}$$

Since both of $I(t)$ and $R(t)$ (upon which L depends) are measured experimentally, this is precisely the expression that was sought.

Upon closer examination, however, one notices that since $L(R)$ is both a.) positive, and b.) monotonically increasing, positive $\frac{\mathrm{d}R}{\mathrm{d}t}$ implies that I and $\frac{\mathrm{d}I}{\mathrm{d}t}$ must have opposite signs. That is, increasing loop size is accompanied by a decrease in the magnitude of the current (i.e., the current is either positive and decreasing or negative and increasing).

In hindsight, of course, this could be figured out from the definition of inductance (restated in equation (3.7)) alone. If flux is constant, then when inductance increases (as it does with increasing radius), current must decrease:

$$I = \frac{\Phi}{L} \tag{3.12}$$

At first glance, the "contradiction" in this is that the typical plasma produced by the experiment is for much, if not most, of its lifetime characterized by radius and current magnitude that *both* increase in time. In fact, however, the electromotive force around the plasma loop is not zero, as assumed in Eq. 3.2; there is a finite voltage measured from one end of the plasma to the other.[4] Appendix C examines in detail the expected magnitude of $\mathrm{d}\Phi/\mathrm{d}t$ and how it is comparable to the voltage measured across the electrodes.

While this explains why Equation 3.11 does not fit the experimental conditions, it also seems to suggest that an expression for the hoop force must be derived some other way. In fact, a derivation without the constant flux assumption yields surprisingly similar results.

3.1.3 Force calculation without constant flux assumption

One cannot calculate the Lorentz force per unit length $\mathbf{F} = I\hat{l} \times \mathbf{B}$ that the entirety of a infinitesimally thin hoop exerts on itself because the expression for $\mathbf{B}$ diverges precisely where you need to evaluate it. One can, however, calculate the Lorentz force per unit length due to the portion of the loop that is "sufficiently far away", if there is a suitable length scale to give that phrase meaning.

[4]The theoretical loop that *does* have zero resistivity retains the curious property that turning up the current is associated with the major radius contracting. No doubt this has been either observed or disproved by those who work with superconductors.

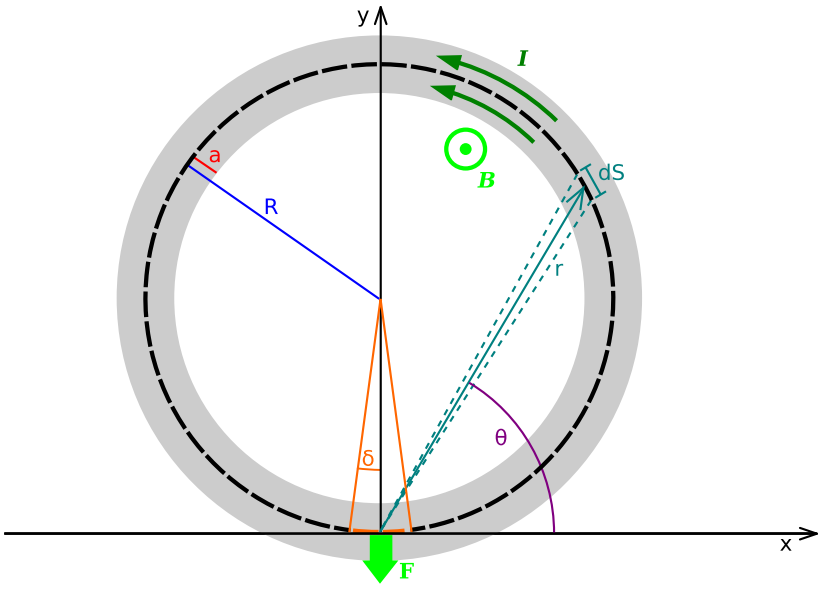

Figure 3.2: Diagram for calculating $\mathbf{F}$, the Lorentz force per unit length experienced by a circular, current-carrying hoop with major radius R and minor radius a

Consider the illustration shown in Figure 3.2 of a current-carrying hoop with a finite minor radius. In order to estimate the Lorentz force per unit length, most of the hoop will be approximated by an infinitesimally thin wire with radius R (indicated by the dashed black line). The section of the wire within one minor radius a of the origin will be neglected.

For convenience, we will place our origin at the point along the wire where $\mathbf{F}$ is to be calculated, such that the loop is in the xy plane and the current I runs counterclockwise along the circle $r(\theta) = 2R\sin\theta$. $\mathbf{B}$ at the origin is given by the Biot-Savart law

$$\mathbf{B} = \frac{\mu_0 I}{4\pi}\int_{\text{hoop}} \frac{\mathbf{r}\times \mathrm{d}\mathbf{s}}{|r^3|} \tag{3.13}$$

where $\mathrm{d}\mathbf{s}$ is an infinitesimal segment of the wire with displacement vector $\mathbf{r}$. Based on symmetry arguments and the right-hand rule, $\mathbf{B}(0,0)$ is out of the page, resulting in a downward force (represented by the large green arrow). The magnitude of $\mathbf{B}$ is

$$\begin{aligned} B &= \frac{\mu_0 I}{4\pi}\int_{\text{hoop}} \frac{r\sin\theta}{r^3}\,\mathrm{d}s \\ &= \frac{\mu_0 I}{4\pi}\int_{\text{hoop}} \frac{\sin\theta}{r^2}\sqrt{(\mathrm{d}r)^2 + (r\mathrm{d}\theta)^2} \\ &= \frac{\mu_0 I}{4\pi}\int_{\theta=\delta/2}^{\theta=\pi-\delta/2} \frac{\sin\theta}{r(\theta)^2}\sqrt{\left(\frac{\mathrm{d}r(\theta)}{\mathrm{d}\theta}\right)^2 + r(\theta)^2}\,\mathrm{d}\theta \end{aligned} \tag{3.14}$$

where $\delta = a/R$ and $r(\theta) = 2R\sin\theta$. This simplifies to

$$\begin{aligned} B &= \frac{\mu_0 I}{8\pi R}\int_{\theta=\delta/2}^{\theta=\pi-\delta/2}\frac{\mathrm{d}\theta}{\sin\theta} \\ &= \frac{\mu_0 I}{4\pi R}\ln\left[\cot\left(\frac{\delta}{4}\right)\right]. \end{aligned} \tag{3.15}$$

When $\delta/4 = a/(4R)$ is small, $\cot\delta/4 \approx 4/\delta$, and the resulting approximation for $F_{hoop} = IB$ is

$$F_{hoop} = \frac{\mu_0 I^2}{4\pi R}\left(\ln\left(\frac{R}{a}\right) + 1.39\right). \tag{3.16}$$

By comparison, the force per unit length calculated from equations (3.3) and (3.6) is

$$F_{hoop} = \frac{\mu_0 I^2}{4\pi R}\left(\ln\left(\frac{R}{a}\right) + 1.08 + Y\right) \tag{3.17}$$

The two expressions are quite similar, surprisingly so considering the approximations made to get Equation 3.16, such as completely omitting the "nearby" segment (which gives rise to the internal inductance contribution that shows up as Y in equation 3.17).

In the context of the larger picture, this shows that the intuitive explanation of antiparallel currents (well, more-or-less antiparallel, depending on how far around the circle the segment in question is from the origin) matches very well *quantitatively* with the standard hoop force derivation.

3.1.4 Effect of hoop shape on inductance

An implicit assumption thus far has been that it is valid to express the inductance of the plasma as that of a circular loop. Hansen supported this assumption with the concept of a three-dimensional "image current" through the copper electrodes [44]. Even in the absence of an image current, though, the precise geometry of the loop axis is not expected to significantly affect the effect of the hoop force on the plasma.

As a case in point, consider the self-inductance of a square loop, which can be written as

$$L = \frac{\mu_0 P}{2\pi}\left(\ln\left(\frac{w/2}{a}\right) - 2 + Y + 1.92\right) \tag{3.18}$$

where a is the minor radius of the wire, w is the width of a side of the square (making $w/2$ roughly comparable to a radius), and $P = 4w$ is the perimeter [43, 45]. For comparison, equation (3.4) can

be written as

$$L = \frac{\mu_0 C}{2\pi}\left(\ln\left(\frac{R}{a}\right) - 2 + Y + 2.08\right) \tag{3.19}$$

where $C = 2\pi R$ is the circumference of the loop. Thus, it is clear that "tweaking" the shape of the loop axis (in this case, from circle to square) has relatively little effect on the inductance.

There is also the question as to exactly what constitutes $R \gg a$, and how far off the inductance will be if R is, say, only two or four times larger than a, rather than an order of magnitude. This question was answered by the numerical investigations of Žic, Vršnak, and Skender into "thick" toroidal currents [46]. For $R \sim 2a$, Equation 3.4 — the "slender torus" approximation — was found to overestimate the toroid's inductance by about 40 percent, while for $R \sim 4a$ it gave an 18 percent overestimate. Even for $R \sim 10a$, Equation 3.4 was 13 percent high.

Žic, Vršnak, and Skender suggest that Equation 3.4 be replaced as the "go-to" expression for the inductance of a toroid with

$$L(\eta) = A' R\left(\ln\left(\frac{8}{\eta}\right) - B'\right) + L_i \tag{3.20}$$

for $\eta = a/R < 0.49$.[5] The constants $A' = 14\ \times 10^{-7}$ Hm^{-1} and $B' = 2.4$ come from numerical fits, and represent changes of about 10 and 20 percent, respectively, from the corresponding constants μ_0 and 2 in Equation 3.4. L_i is the component of inductance internal to the wire (corresponding to the Y term in Equation 3.4), and was unchanged from the slender torus approximation. (It ranged from $1/4$ for a uniform current distribution to $1/2$ for a current with the peaked distribution of a J_0 Bessel function, with a J_1-shaped distribution falling between the two.)

The thick torus expression given by 3.20 is a nonnegligible correction to a widely used approximation, and represents a definite improvement. For plasma loops, however, whose value of η is not precisely known and whose major axis is not a perfect circle, the corrections of 10 to 20 percent can be considered as an afterthought (as in Appendix F).

3.1.5 $R(t)$ predicted by a simplified hoop force model

Having established the robustness of the hoop force, as given by Eq. 3.17 (or something reasonably similar to it, as discussed abve), consider the situation in which F_{hoop} is the dominant radial force. That is, neglect field line tension, centrifugal forces, et cetera. Then, the equation of motion for an

[5] For even thicker tori with $\eta > 0.49$, an entirely different expression for L was required to fit the numerical results.

infinitesimal segment of the hoop with length ds and mass dm is given by

$$F_{hoop}ds = \ddot{R}dm = \ddot{R}m_i n\pi a^2 ds \tag{3.21}$$

where n is number density and m_i is ion mass. R and a remain the major and minor radii, respectively.

Because the term in parentheses in Eq. (3.17), which will be designated α, is nearly constant due to the slowly changing logarithm, most of the dependence is in the R^{-1} factor. Equation (3.21) can then be written

$$\ddot{R}\left(t\right) = \frac{F_{hoop}}{m_i n\pi a^2} = \frac{\alpha}{4\pi^2}\frac{\mu_0}{m_i n a^2}\frac{I(t)^2}{R\left(t\right)}. \tag{3.22}$$

Inspired by experiment observations, the constants n and a are assumed time-independent; the hoop is able to stretch/extend in the major radial direction without changing its minor radius or density.

Consider the case in which the current $I(t)$ rises linearly, as it does in the experiment for early times $t < \tau$. The current can be described by

$$I(t) = I_0\frac{t}{\tau}. \tag{3.23}$$

When this is substituted into Eq. (3.22), the resulting second-order differential equation has an analytical solution

$$R\left(t\right) = \frac{1}{2\pi}\sqrt{\frac{\mu_0\alpha}{2m_i n}}\,\frac{I_0}{a\tau}\,t^2. \tag{3.24}$$

This solution has the following characteristics that will turn out to be noteworthy in comparisons in plasma loop experiments:

1. The radius R depends quadratically on time t.

2. The time-dependent radius $R(t)$ scales with the slope of the current I_0/τ.

3. The rate of expansion $\dot{R}(t)$ scales in proportion to a "toroidal Alfven speed" $B_\phi/\sqrt{\mu_0\rho}$ where $B_\phi(t) = \mu_0 I(t)/(2\pi a)$ and $\rho = m_i n$ is the wire's mass density.

3.2 Model 2: The gobble effect

The "gobble" model[6] was conceived by Bellan [47] with the goal of explaining the unexpectedly high degree of axial uniformity observed in plasma arches, such as the pair of laboratory loops pictured in Figure 3.3(a) and the solar coronal loops in the TRACE[7] image in Figure 3.3(b). Subsequently, Kumar and Bellan further developed the analysis [48].

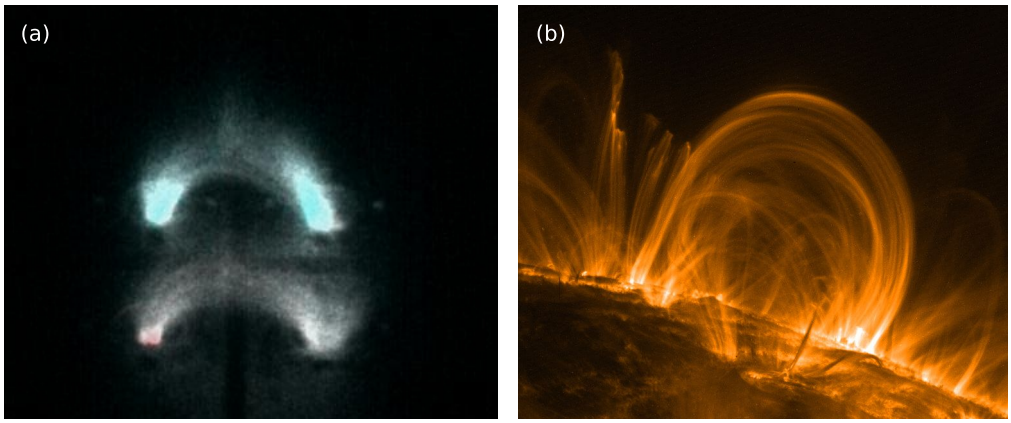

Figure 3.3: Both in the laboratory and in the solar atmosphere, arches of plasma are narrower at their apexes than theory had predicted they ought to be. a.) Two adjacent Caltech plasma loops, one composed of hydrogen (tinted red) and one of nitrogen (tinted cyan). b.) NASA's Astronomy Picture of the Day on 28 September 2000: an image of solar coronal loops taken in the 171 Å band pass by the TRACE spacecraft

Conceptually, the model approaches the question of why these arches are collimated by asking, "What would happen if you *did* have a current-carrying, plasma-filled flux tube with a nonuniform cross section?" The answer is that MHD forces would generate axial flows — an "MHD pumping mechanism" [30] — that would cause the tube to collimate.

3.2.1 Key concepts

"Straightening out" the arch: In order to make the mathematics tractable, the model addresses the problem in a cylindrically symmetrical coordinate system, where z is aligned with the flux tube axis. Instead of an arched flux tube with a wider apex and narrower legs, the corresponding structure is bulged flux tube with a wide middle and narrow ends, as pictured in the first frame of Figure 3.4.

[6]The nickname comes from the paper's title, "Why current-carrying magnetic flux tubes gobble up plasma and become thin as a result."

[7]The Transition Region and Coronal Explorer is a mission of the Stanford-Lockheed Institute for Space Research, and part of the NASA Small Explorer program. Further information about this image, as well as other TRACE data, can be found at *http://soi.stanford.edu/results/SolPhys200/Schrijver/TRACEpodarchive.html*.

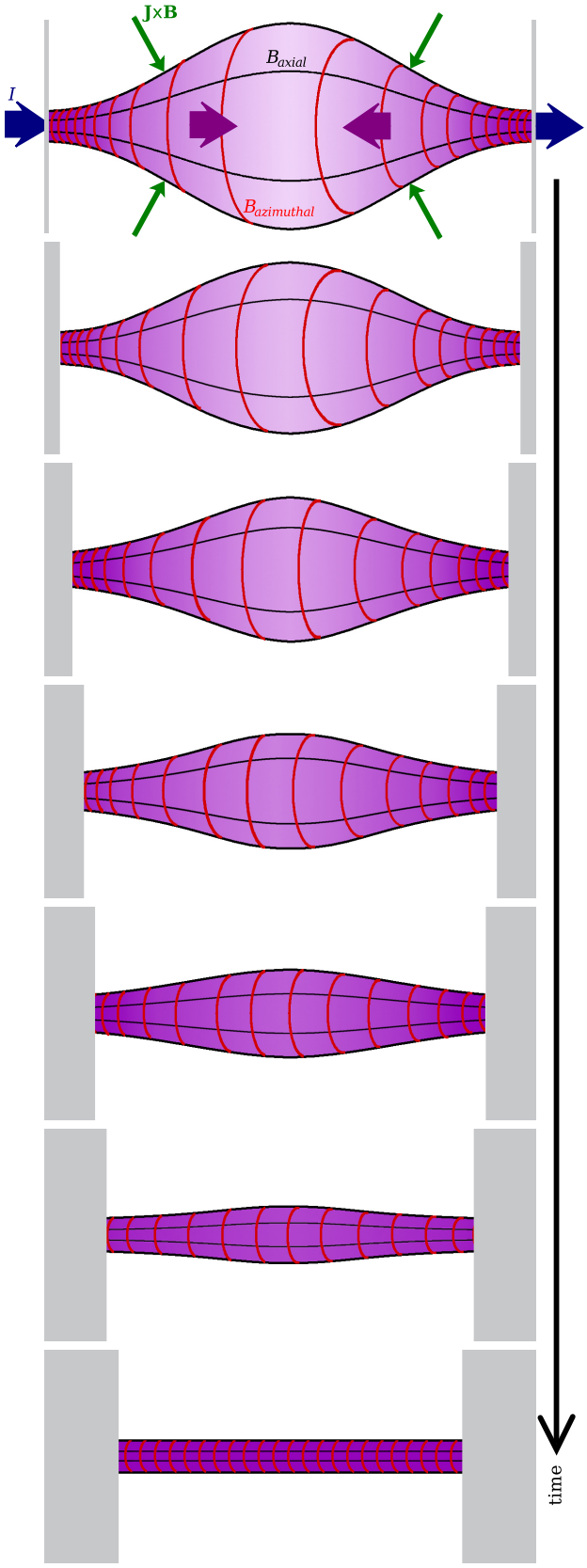

Figure 3.4: Cartoon of the gobble effect

Quasi-equilibrium: One of the main features of the gobble model is that it does not start by assuming force balance everywhere. In fact, this assumption cannot necessarily be made for an arbitrary magnetic field configuration. Mathematically, this can be seen by considering the curl of the force balance equation

$$\mathbf{J} \times \mathbf{B} = \nabla P. \tag{3.25}$$

Whereas the right-hand side $\nabla \times \nabla P$ is identically zero, the left-hand side may be finite. Hence, one can have a magnetic field structure whose $\mathbf{J} \times \mathbf{B}$ forces *cannot* be balanced by *any* pressure gradient, and which therefore cannot exist in equilibrium. The bulged flux tube turns out to be one such structure.

This can be illustrated by starting with an equilibrium in the radial direction — i.e., a local "pinch"[8] — and calculating what this means at different axial locations. The radial component of Equation 3.25 in the cylindrical coordinate system is

$$J_\phi B_z - J_z B_\phi = \frac{\partial P}{\partial r}. \tag{3.26}$$

The axial magnetic field (the black lines in Figure 3.4) is presumed to be externally generated, so $J_\phi = 0$ in the flux tube. The pressure gradient is then balanced by the product of J_z (the z component of the current flowing along the flux surfaces defined by B_{axial})[9] and the axial field B_ϕ (generated by J_z, and shown in the illustration in red). Both of these quantities are larger where the flux tube is constricted and smaller where it is bulged, so $\partial P/\partial r$ follows suit.

Although the exact on-axis pressure depends on the form of the radial current distribution, any number of examples can be used to show that integrating $\partial P/\partial r$ from the edge of the flux tube to the center results in lower pressures in bulged regions than in collimated regions. (When current is distributed uniformly over the radius, $P_{r=0} \sim a^{-2}$ where a is the flux tube radius.)

Flows, flux convection, and collimation: Hence, the quasi-equilibrium of radial force balance implies an axial pressure gradient. There is a higher plasma pressure (indicated in Figure 3.4 by the purple gradient) in the narrower regions of the flux tube. Furthermore, regions of the flux tube

[8] There are multiple classic plasma pinch configurations that for straight cylinders fully satisfy Equation 3.25 everywhere, yielding static equilibria. Unfortunately for those attempting to build magnetic fusion confinement devices based on those pinches, the stability of the equilibria is another matter. [1]

[9] Because the current flows along the flux surfaces, the total current $I(r,z) = \int_0^r J_z(r',z) 2\pi r' dr'$ enclosed by a loop of radius r at axial location z must be a function of the total flux $\psi(r,z) = \int_0^r B_z(r,z) 2\pi r' dr'$ enclosed by that same loop. That is, $I = I(\psi)$.

where the radius is not stationary as a function of z have $\mathbf{J} \times \mathbf{B}$ forces with $\hat{z}$ components. Both of these effects generate axial flows from the ends toward the center of the bulge.

If the resistivity is sufficiently low that the magnetic flux can be considered frozen in, then the axial bulk flows that transport plasma also transport magnetic flux. As B_ϕ increases in the bulge, the pinch force increases. The bulge narrows, causing the current density to increase.

As illustrated in Figure 3.4, the process continues until the flux tube is collimated, at which point the axial pressure is uniform and the $\mathbf{J} \times \mathbf{B}$ forces are purely in the radial direction.

Boundaries: Because material is moving away from the boundaries, one must consider what the boundary conditions are for the flux tube. In the straight, cylindrical geometry, Bellan allows the ends of the flux tube to contract, keeping the total magnetic energy due to the axial magnetic field constant. This corresponds to an arched flux tube decreasing in major radius. In the flux tubes created experimentally (as well as many occurring naturally), there is a source of additional plasma beyond the ends of the original flux tube, and this can allow the flux tube to increase in length.

3.2.2 Predicted flow velocity

Kumar and Bellan found that the final velocity of the axial flow accelerated by a "flared" flux tube (narrow at one end and wide at the other) from the narrow end ($z = 0$) to the wide end ($z = L$) is

$$u_z|_{r=0,z=L} \approx \sqrt{4\kappa L}\,\frac{B_\phi(z=0, r=a_0)}{\sqrt{\rho_0 \mu_0}} \tag{3.27}$$

where $a(z) = a_0\, e^{\kappa z}$ describes the shape of the flux tube, with a_0 equaling the tube's width at its narrowest and κ the characteristic length scale of the widening. The mass density at $r = 0$, $z = 0$ is given by ρ_0. The axial magnetic field and current are assumed to be parallel (i.e., the current flows along flux surfaces), with uniform radial distributions; the magnitude of the proportionality constant $\lambda = \mu_0 J_z / B_z$ is assumed to be $>> 2\kappa$, implying that the pressure profile is predominantly determined by the axial current — or, alternatively, that the toroidal energy density $\beta_\phi \sim 1$.

To summarize, the gobble model applies to dynamic situations where the magnetic flux tube is not in equilibrium due to a nonuniform radius. It predicts plasma flows from narrower regions to wider regions. These flows carry frozen-in flux, ultimately resulting in collimation, and like the hoop force they scale in proportion to the "toroidal Alfven speed".

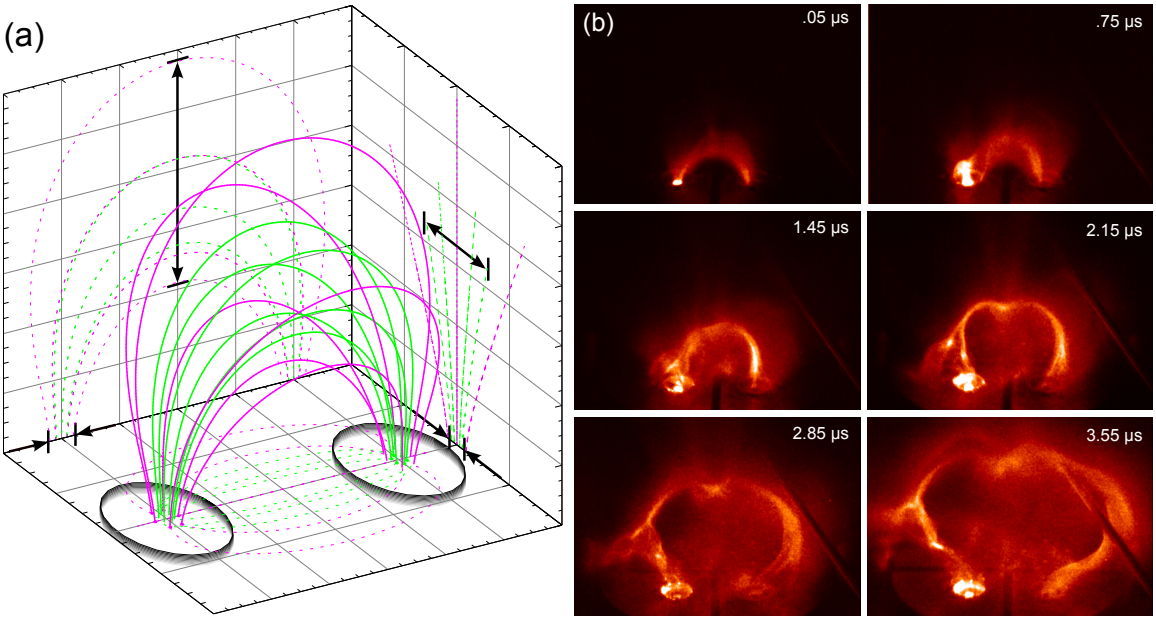

Figure 3.5: (a.) Two sets of vacuum magnetic field lines link a pair of solenoids (only the last few coils of which are drawn). Dashed lines show the projection of the magnetic field lines onto the three orthogonal planes; arrows indicate lines' separation, which is 5 to 8 times greater at the top of the arch than at the footpoints. (b.) A hydrogen flux tube (shown with a red temperature color table) exhibits a comparatively narrow, uniform cross section, both shortly after its formation (0.05 μs) and even as its axis lengthens and kinks at later times. *(shot 5772)*

3.3 Experiments with single plasma loops

Experiments were conducted with both single-species loops (for which one type of neutral gas was supplied to the gun) and dual-species loops (for which two types of neutral gas were supplied).

3.3.1 Creating arched, plasma-filled flux tubes

For each plasma shot, a vertical pair of magnetic field coils (as pictured in Fig. 2.2d) were pulsed to produce an arched vacuum magnetic field (i.e., potential field) akin to that of a horseshoe magnet. Fig. 3.5a shows the magnetic field lines calculated for a pair for current-carrying solenoids. The field strength had a temporal FWHM of 7 ms and spatially varied from 0.35 T near the footpoints to 0.01 T near the apex of the arch. (Details of the magnetic field measurements are described in Appendix A.)

The gas valves supplying the two footpoints were then pulsed, shortly after which neutral gas entered the chamber at each of the footpoints. According to measurements by You [49], the peak neutral density would occur 3 cm from the electrode, beyond which it would fall off exponentially.

(Additional discussions of the gas delivery can be found in Appendix B.)

At this time high voltage from the main capacitor was applied to the electrodes, thereby ionizing the gas to form an initial low-density plasma. This quickly evolved into a current-carrying, plasma-filled flux tube, or "loop". (This evolution process, analyzed in detail by You [49], involves the flux tube narrowing as it fills with bright plasma.)

The capacitor was typically charged to 3–6 kV, resulting in a peak output current of 25–65 kA at ~ 5 μs after initial breakdown, of which approximately one tenth of the total current output flowed through the flux tube (Section 2.3.2). The absence of neutral emission lines in nonhydrogen plasmas [30] indicate that the plasma is almost completely ionized. (In hydrogen plasmas, *only* neutral atoms radiate line spectra.) Plasma densities are 10^{20}–10^{21} m^{-3} inside the flux tube, corresponding to $\beta \simeq 0.01$–0.1. The configuration evolves over 3–5 μs, until the loop detaches from the electrode and/or grows large enough to come in contact with the chamber wall behind the electrode.

Although the plasma-filled loop is semitoroidal when it forms, magnetic forces drive a rapid evolution toward more complex structures, as shown in Fig. 3.5b. Two parameters characterize the loop geometry: the flux tube minor radius and the locus of the flux tube axis. Plasma is confined inside the minor radius, corresponding to a force balance condition. By contrast, the axis is observed to evolve dramatically, increasing to as much as 10 times its initial length and undergoing a kink instability. (The observation of the kink instability suggests that the evolution of the loop structure is slower than the Alfven velocity.)

During this process, the minor radius remains relatively constant and the entire loop remains bright, indicating that the loop density and cross-sectional area are independent of time. Previous investigations of these loops demonstrated that bright areas are regions of high plasma density [49] [30]. MHD simulations by Arnold et al. also support this conclusion [15]; among current structures predicted from a variety of conditions, including fixed uniform density and an ionization/recombination model, those most resembling experimental loops were achieved when the density was set to be greater in the flux tube than in the surrounding volume.

Because the flux tube volume increases substantially while the emission intensity (brightness) remains approximately constant, material must be entering the plasma structure. If this were not the case, the tenfold increase in loop length would produce a tenfold decrease in loop density, and optical emission intensity, proportional to the square of density [30], would drop 100-fold.

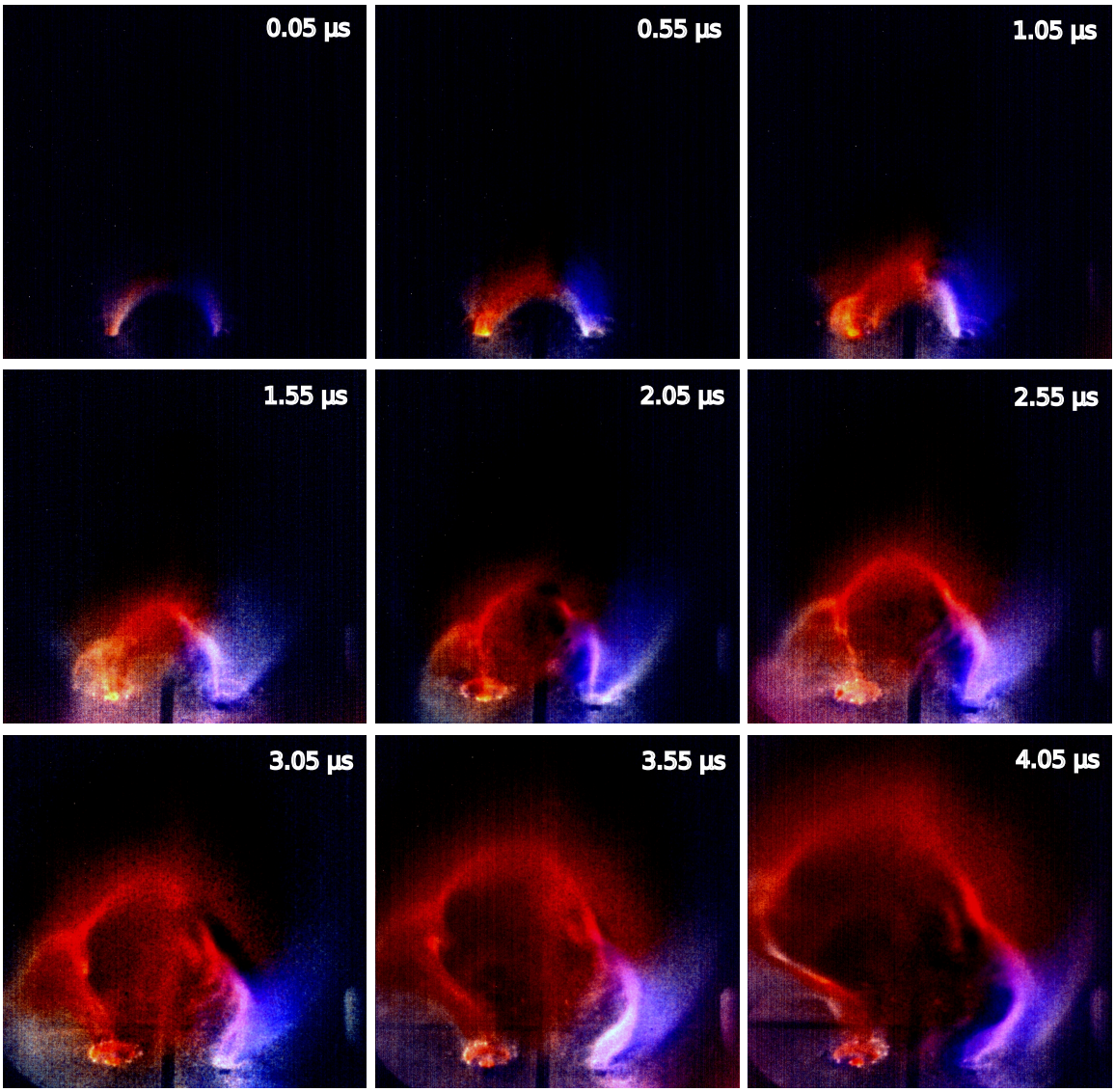

Figure 3.6: A hydrogen/nitrogen plasma loop at nine consecutive times. Color pictures were produced by combining images from three different shots using the "subtraction" method (described in Section 2.3.5). Nitrogen sections of the plasma are tinted blue and hydrogen sections of the plasma are tinted red. *(shots 5019, 5027, and 5024)*

3.3.2 Visualizing flows with dual-species loops

To determine the source of material entering the plasma loop, experiments are performed using a different gas at each of the two-footpoint nozzles. Because the experiment is highly reproducible, subsequent plasma shots can be photographed with optical filters chosen to transmit only the optical line emission of one species, then combined digitally (as described in Section 2.3.5). Figure 3.6 presents typical images produced by this color-coding technique. These images indicate that plasma flows into the loop from both footpoints, and that the flow dynamics depend strongly on the mass density.

To quantify the flow dynamics, image sequences (interframe time 200–400 ns) are made for various combinations of gas species. The locus of the flux tube axis is manually traced out in each frame, as is the fraction of the loop length occupied by each species. Examples of the resulting sets of traces are shown in Figure 3.7.

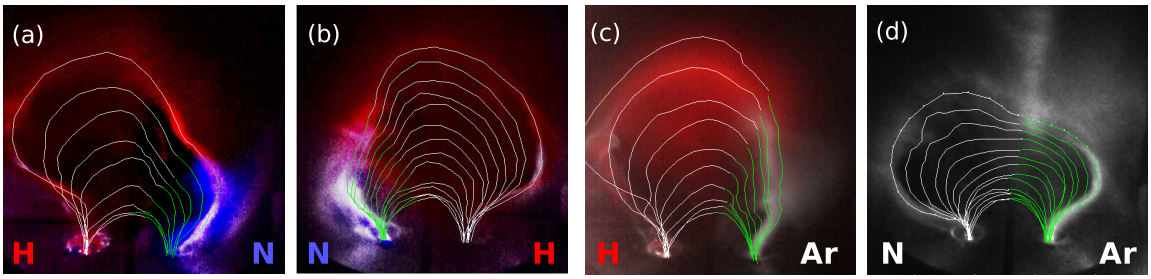

Figure 3.7: a.) Traces of the loop axis for each of the frames shown in Figure 3.6, all overlaid on top of the last frame. Thin white and green contours indicate the hydrogen and nitrogen sections of the loop, respectively. b,c,d.) Similar collections of curve traces for other dual-gas plasma combinations. In the case of the N/Ar combination (d), appropriate optical filters for "color coding" were not available, so the boundary between the two species is chosen based on the "cusp" that forms there. *(shots 5019/5027/5024, 5268/5269/5271, 5052/5051, and 5278)*

The spatial dimensions of the curve traces were then scaled to the nozzle spacing and adjusted for the camera viewing angle. The resulting measurements of the time-dependent loop length indicate the plasma flow speeds along the loop axis.

Figure 3.8 gives a compilation of these measurements, made from plasma shots taken on different days and with different gas species combinations (e.g., supplying hydrogen to the cathode and nitrogen to the anode (a), nitrogen to the cathode and argon to the anode (d), etc.). All shots had the same 4.0 kV capacitor charge and the same vacuum magnetic field charging voltage (200 V).

An important conclusion is that the length of each subsection of the loop is nearly independent of the other subsection. For example, the nitrogen section of a nitrogen/argon loop (shown in Figure

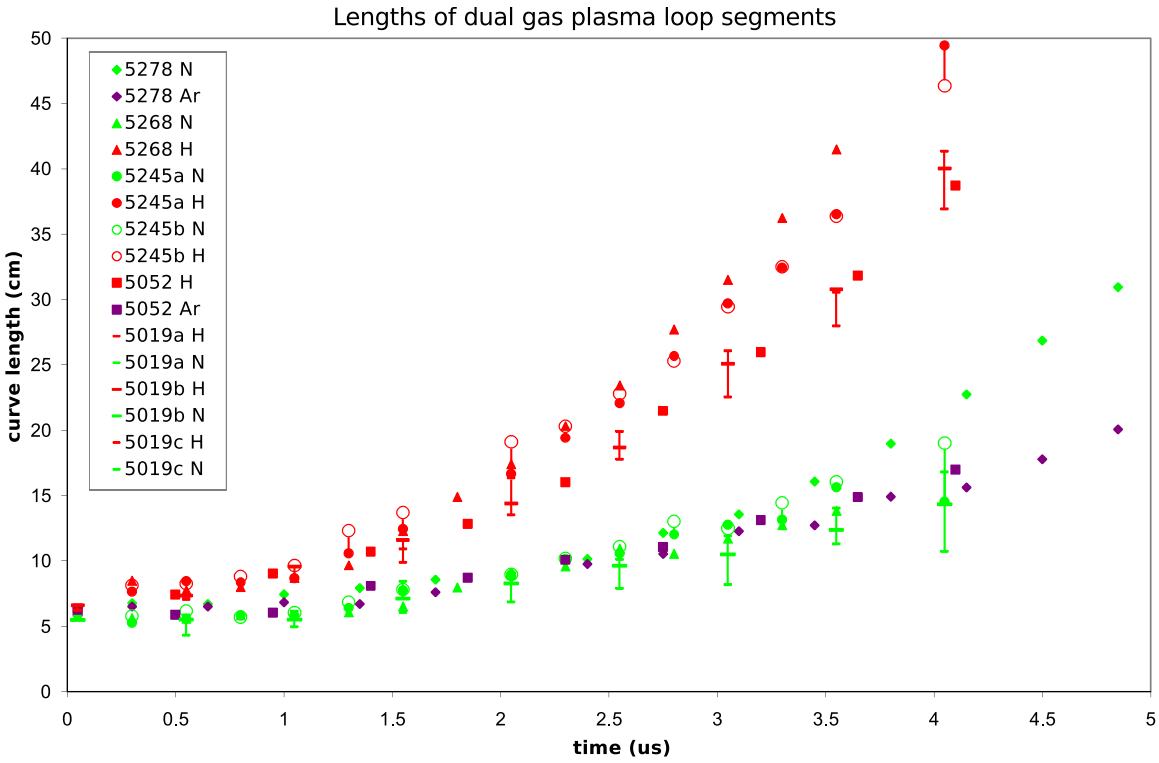

Figure 3.8: Curve length measurements from a number of different dual-gas plasma images, including those in Figure 3.7. Each image compilation is represented by a different shape, and denoted with the shot number of the unfiltered image. There are multiple sets of curves for shots 5245 and 5019 because the same set of shots was traced multiple times, using different methods of combining the images and/or judging the location of the boundary between the two species; the spread of the resulting measurements is indicated by the vertical error bars. (For more details on the error and uncertainty of loop traces, see Appendix D.) That both the hydrogen and nitrogen segments of 5019 are lower than average suggests that this shot might have had a lower-than-average plasma current for the charging voltage.

3.7d) increases in length at a rate comparable to that of the nitrogen section of a hydrogen/nitrogen loop (shown in Fig. 3.7a–b), even though the axis loci of the two sections evolve differently, as do the total loop lengths. Each species flows from a footpoint into the flux tube at a particular speed. (The two flows butt up against each other and, being connected in series, conduct the same total plasma current.)

Thus, any given loop is a sum of two independent plasma flows, each originating from its respective footpoint. Figure 3.9 expresses this in cartoon form.

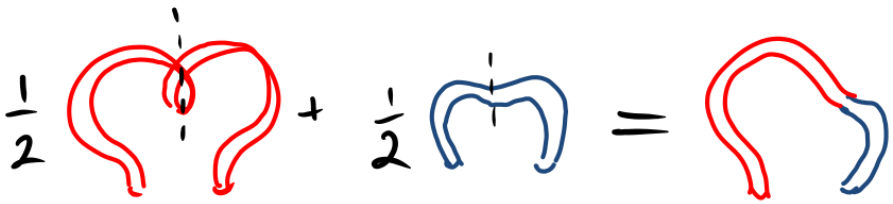

Figure 3.9: Loop addition

3.3.3 Getting more quantitative with single-species loops

Single-gas loops were used to determine the relationship between loop dynamics and electric current. (A single-gas loop comprises two sections of the same species and is hence twice as long as the sections shown in Figure 3.8.) Increasing the capacitor charge voltage increases both the electric current and the rate at which the plasma loop lengthens/expands. The results are shown in Figure 3.10.

For each species (hydrogen/nitrogen/argon), the first panel (a/d/g) plots the loop length versus time for plasmas loops fired from charging voltages of 3.0–6.0 kV.[10] The second panel (b/e/h) shows the corresponding capacitor output currents I_{cap} versus time for the same set of shots. (Recall that magnetic probe measurements indicate current through the flux tube $I(t) \approx I_{cap}(t)/10$.) The third panel (c/f/i) shows a parametric plot of the time derivatives of the quadratic fits shown in (a/d/g) versus the simultaneous current values shown in (b/e/h), demonstrating a single proportionality constant at early times.

At all charging voltages, the loop length grows in proportion to time squared; quadratic fits for

[10]Note that many loops have a small initial "dip" in length, appearing to shorten/contract slightly before they begin to lengthen/expand. This is consistent with the gobble model prediction that inflows would cause an initial decrease in end-to-end flux tube length. Another possibility is that the loop is rotating/twisting in the very early stages of a kink, angling it out of the plane perpendicular to the camera and therefore making it appear shorter.

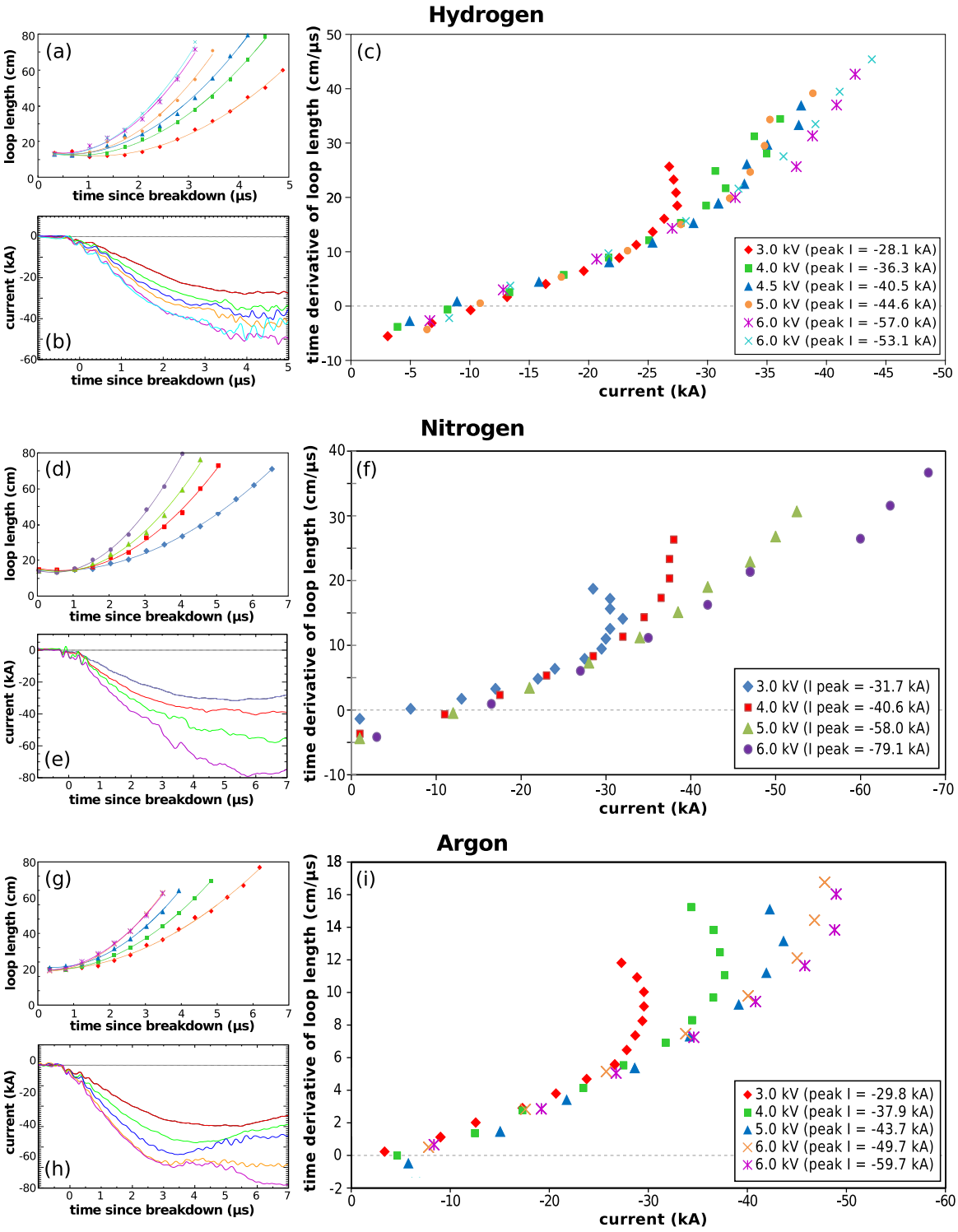

Figure 3.10: Dependence of flow speed on current: plots of loop length $s(t)$ versus time, capacitor output current $I_{cap}(t)$ versus time, and the parametric plot $\dot{s}(t)$ versus $I_{cap}(t)$ for each species of single-gas plasma loops. The legend for each trio of plots is given in the lower-right-hand corner of that section. Note that plots of the same quantity for different species do not necessarily have the same scale. *(hydrogen shots: 9098, 9090, 9102, 9105, 9112, and 9114; nitrogen shots: 5927, 5920, 5939, and 5945; argon shots: 9059, 9054, 9071, 9078, and 9084)*

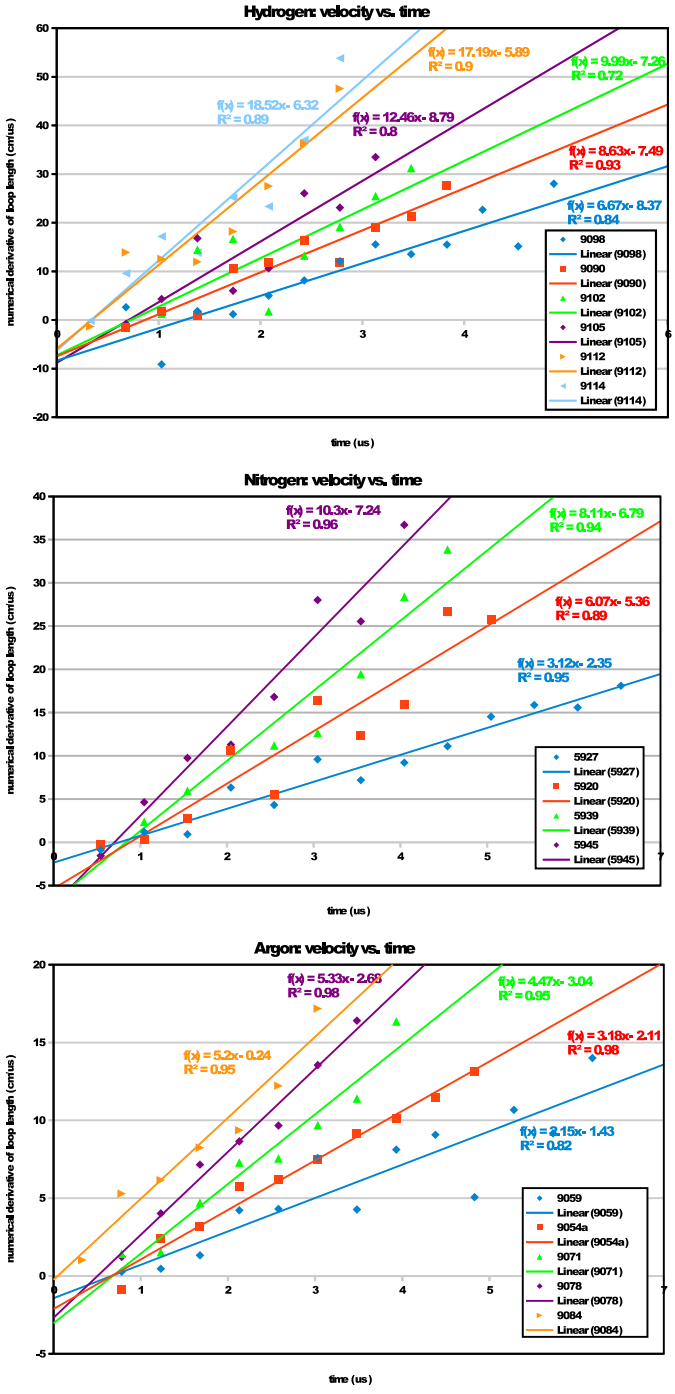

Figure 3.11: Numerical derivatives of the loop length data in Figure 3.10, though scattered, appear to increase linearly in time.

the data in Figure 3.10a/d/g are shown, and the numerical derivatives plotted in Figure 3.11, though noisy, suggest that quadratic fits are indeed warranted.

Furthermore, the constant acceleration of each loop is directly proportional to the initial rate at which the electrical current increases, with the same proportionality for all loops of a given species. Figure 3.10c/f/i are parametric plots showing this result. In each, the shared slope at low electrical currents (corresponding to early times) indicates that all of the loops have the same $\ddot{s}(t)/(I_0/\tau)$ where $\ddot{s}(t)$ is the second derivative of the loop length with respect to time and I_0/τ is the initial slope of the electrical current $I(t)$.

3.4 Analysis

Any theory that proposes to explain the dynamics of the experimental plasma loops (i.e., arched, plasma-filled flux tubes) must address the following features:

- a flux tube maintains its density and minor radius even as its axis grows substantially;
- material is observed to enter the flux tube from both footpoints;
- the speed of these flows depends on plasma species and electrical current;
- the two flows add linearly to form the total length of the loop;
- the axis — and, hence, major radius — grows quadratically in time;
- the constant acceleration experienced by a loop is, at early times, directly proportional to the rate at which the electrical current increases;
- all loops of a given species exhibit the same proportionality between acceleration and current.

This can be done by combining the hoop force model and the gobble model.

3.4.1 Hoop-force-driven expansion

The hoop force is an obvious candidate for explaining the loop's axis expansion. The simplified model presented at the end of Section 3.1 yields an analytic solution for $R(t)$ (Equation 3.24) that includes quadratic time dependence, proportionality with electric current, and an inverse square root dependence on hoop mass density. In order to address experimental plasma loops, however,

this analytic solution must be replaced by a numerical solution that accommodates finite major radii at $t = 0$.

Toward this end, Equation (3.22) can be written as

$$\ddot{R}(t) = \kappa \frac{I(t)^2}{R(t)} \quad \text{where } \kappa = \frac{\alpha \mu_0}{4\pi^2 m_i n a^2} \tag{3.28}$$

and numerically integrated. This was done for each plasma shot shown in Figure 3.10 via the fourth order Runge-Kutta method [35], by means of a program that used the built-in IDL function RK4. $I(t)$ was represented by a sine function fitted to $I_{cap}(t)$ (an example of which is shown in Figure 3.12) and then scaled by $f = 1/10$ (the fraction of capacitor current flowing through the loop itself). $R(0)$ was taken from the measured first frame loop length. $\dot{R}(0)$ was assumed to be zero.

The numerical solutions $s_{num}(t) = \pi R(t)$ (approximating the loop as a semicircle) were fit to experimental data by finding the value of κ for each shot that maximized R-squared.[11] Results are shown in Figure 3.13. The numerical solutions do not fit the data quite as well as the parabolic curves shown in Figure 3.10a/d/f, but this is not a fair comparison because the parabolic fits had three free parameters, while the numerical fits had just one.

Particularly for hydrogen, and to a lesser extent for nitrogen, κ exhibits a trend across the set of shots. This means that the constant κ does not quite correspond to the proportionality con-

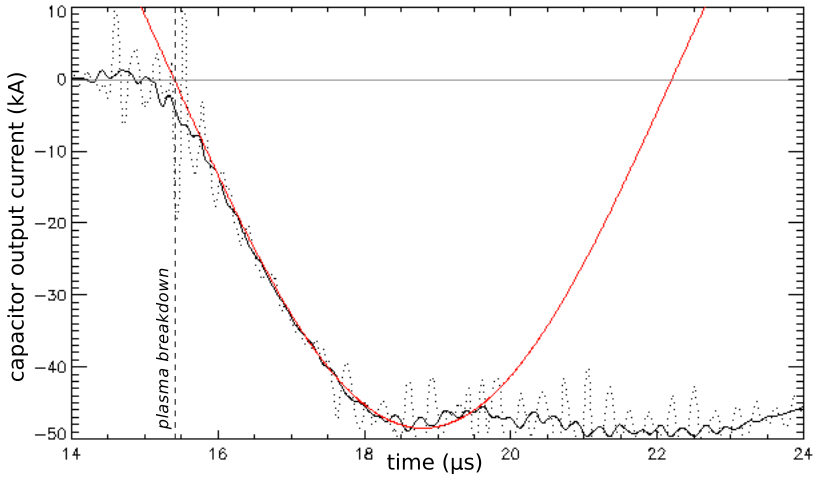

Figure 3.12: An example of the capacitor output current (dashed black line), the capacitor output current with smoothing (solid black line), and the sinusoidal function $I(t) = I_0 \sin(t/\tau)$ (red line) chosen to represent $I_{cap}(t)$ for the purpose of numerical integration. *(shot 9078)*

[11] The coefficient of determination R-squared is defined as $\sum_i (s(t_i) - s_{num}(t_i))^2 / \sum_i (s(t_i) - \bar{s})^2$ where $\bar{s} \equiv \sum_i s(t_i)/n$ and all sums are taken over the number of frames n. The "R" in "R-squared" is not the radius R.

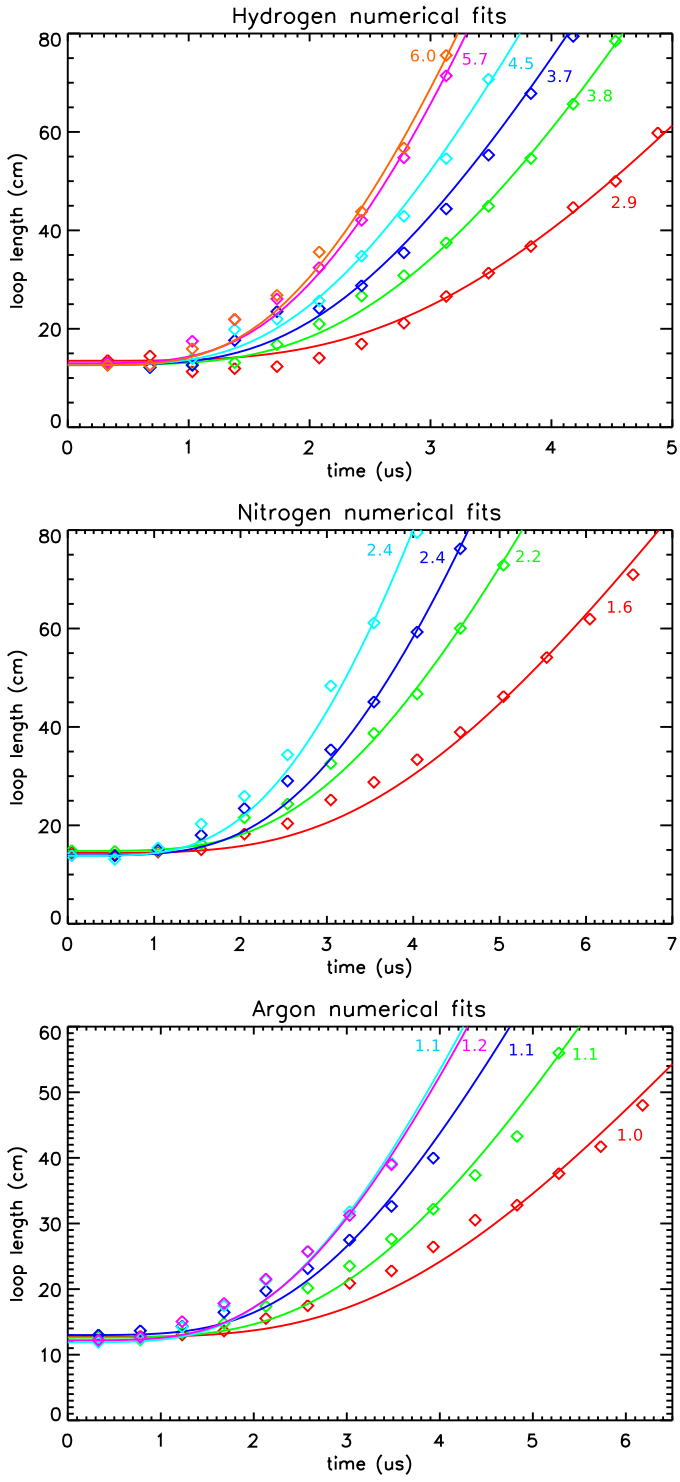

Figure 3.13: Numerical solutions $s_{num}(t)$ (solid lines), calculated from the simplified hoop force model, with the experimental data from Fig. 3.10 to which they were fit. Adjacent numbers indicate the value of κ for each fit, in units of $m^2/(sA)^2$.

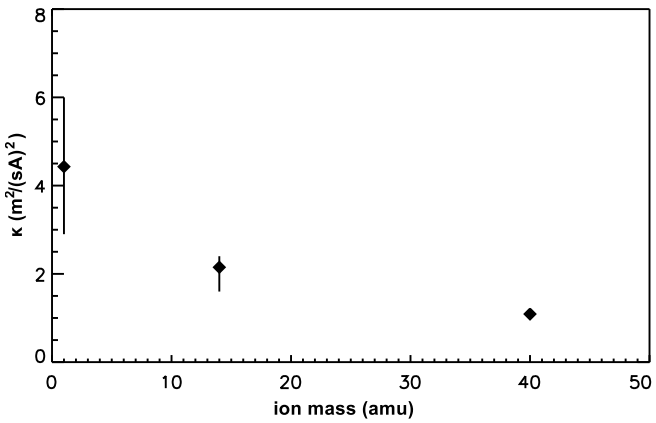

Figure 3.14: Dependence of κ on ion mass; error bars indicate variation in κ within each species.

stant between acceleration and the electrical current at early times, which experiments found to be consistent for all loops of a given species. (This is because $R(t)$ does not have a quadratic time dependence for $R(0) > 1$.) Furthermore, it suggests that either A.) the plasma parameters that κ includes (number density and minor radius) are somewhat different for faster, higher-current loops than they are for slower loops, or B.) the equation of motion for $\ddot{R}$ in Equation 3.28 does not fully capture the physics of the loop expansion (as measured by the curve lengths of loop traces).

To address the second possibility, other forms for $\ddot{R}$ were tried, but the resulting fits to the data were poorer than those for Equation 3.28 and the trend in κ remained. (Details of these investigations can be found in Appendix F.) While the simplified hoop force model may not be exact, it nevertheless provides a reasonably good fit — based on a well-established physics — to the data sets, which themselves are not exact representations of the plasma loop length. (Errors due to projection effects are considered in Appendix D.)

Figure 3.14 shows the values for κ from the fits in Figure 3.13. From these values, one can estimate a number density per unit length using Equation 3.28. Linear number densities and corresponding volume number densities for minor radii of $a = 1$ or 2 cm are shown in Table 3.1[12].

	$\pi n a^2$ (m^{-1})	n (m^{-3}) for $a = 1$ cm	n (m^{-3}) for $a = 2$ cm
hydrogen	4.1×10^{17}	1.3×10^{21}	3.3×10^{20}
nitrogen	5.9×10^{16}	1.9×10^{20}	4.7×10^{19}
argon	4.1×10^{16}	1.3×10^{20}	3.3×10^{19}

Table 3.1: Plasma densities calculated from κ

[12]For hydrogen and argon, the number densities calculated for $a = 1$ are comparable to those recently obtained by Vernon Chaplin with Stark broadening measurements. Stark broadening suggests that nitrogen densities are about an order of magnitude higher, but this is not corroborated by the brightness of nitrogen plasma in images, nor has any

That the hydrogen plasma density is higher than the nitrogen or argon plasma density may be due to mass-dependent variations in the gas delivery system (Appendix B).

3.4.2 Gobble-driven flows

While the hoop force model explains the rate at which the loop axis lengthens, it does not explain the observed inflows entering the flux tube from both footpoints. Without inflow of new material, the density would drop as the loop lengthened. Not only would this increase the hoop force acceleration, but combined with the frozen-in flux constraint, it would also require the minor radius to increase. This is not observed; both the loop brightness and the minor radius stay approximately constant as the loop lengthens.

The speeds of the inflows are significant, which suggests they are driven by MHD, rather than gas dynamics. Table 3.2 shows that both the speed of the neutral gas from which the plasma is formed and the ion thermal velocity $v_{Ti} = \sqrt{2kT/m_i}$ are quite a bit smaller than the observed flows, even for the overly high estimate of $T_i = 10$ eV. Conversely, one can calculate the temperatures associated with ion thermal velocities comparable to the observed flow speeds and observe that they are significantly greater than the experiment's $T_i \leq 4$ eV (determined from Doppler broadening measured in impurity lines [30]). For example, a nitrogen ion moving at a speed of 24 km/s corresponds to a temperature of 42 eV.

The flow speeds predicted by the Gobble model, on the other hand, are comparable to the inflow speeds. Equation 3.27 describes velocities proportional to a toroidal Alfven speed (i.e., calculated from B_ϕ), which for magnetic fields of a few hundred Gauss and plasma densities of $10^{20} - 10^{21}$ m^{-3} are indeed in the tens of kilometers per second. (Plots of Alfven velocity contours in Appendix G can be used to estimate quantitative values for each species at a given magnetic field and number density.) In arched plasma loops, such axial flows would carry plasma and frozen-in azimuthal flux from the footpoints toward the apex, in proportion to the speed at which the loop lengthens.

	neutral gas sound speed (m/s)	v_{Ti} at 1 eV (km/s)	v_{Ti} at 10 eV (km/s)
hydrogen	1310	13.9	44.0
nitrogen	353	3.7	11.7
neon	435	3.1	9.8
argon	323	2.2	7.0

Table 3.2: Neutral gas velocities and ion thermal velocities

mechanism been proposed that would produce such an effect.

3.4.3 Complementary forces with comparable scaling

Both the hoop force model and the gobble model are MHD effects that scale with the toroidal Alfven velocity — or, equivalently, with the plasma current. One must note, though, that scaling in the same fashion does not imply that two things change at the same rate. Suppose, for example, that the volume of the flux tube increased at a rate of $k_1 I(t)$, while the plasma entered the flux tube at a rate of $k_2 I(t)$. Although both quantities would scale linearly with $I(t)$, the density of plasma in the loop could still be increasing or decreasing, depending on the relative values of k_1 and k_2.

Equation 3.24 can be used to calculate that the rate at which the hoop force increases the loop length (and hence the plasma volume) is

$$\dot{s} = \pi \dot{R} = \sqrt{\frac{\mu_0 \alpha}{2\rho}}\ \frac{I}{a}, \tag{3.29}$$

while Equation 3.27 for the flow from each footpoint can be expressed as

$$u_z \approx \sqrt{\frac{\kappa L \mu_0}{\pi^2 \rho_0}}\ \frac{I}{a_0}. \tag{3.30}$$

If we take a in Equation 3.29 to be the final width of the flare along which plasma is accelerated in equation 3.30, so that $a = a_0 e^{\kappa L}$, the ratio between the two inflows and the rate of flux tube lengthening can be written:

$$\frac{2u_z}{\dot{s}} \approx \frac{2}{\pi}\sqrt{\frac{2\ln\left(a/a_0\right)}{\alpha}}\ \sqrt{\frac{\rho}{\rho_0}}\frac{a}{a_0}. \tag{3.31}$$

If we assume that $\rho/\rho_0 = a_0^2/a^2$ (as in the case of a pinch with uniform current density) and $\alpha \sim 3$, the ratio comes out to 0.43. Given the competing mitigating factors that $\dot{s}$ is inflated compared to $\dot{s}_{num}$ (as detailed in Appendix F), but that u_z acts to decrease a/a_0, a result of order unity is satisfactory indication that the two effects have comparable scaling.

Hence, together the hoop force and gobble effect can explain the observations of collimated expansion with constant, species-dependent current proportionality.

3.4.4 Implications for other systems

Because MHD has no intrinsic length scale, the flow dynamics reported here are likely to be present in many other situations governed by MHD. The solar atmosphere contains dynamics described by the hoop force [50], as well as numerous examples of plasma flows. These include material

"spurting" up into the corona toward the end of a failed eruption (31 October 2002, 17:50–18:08) [51], coronal heating via upflows of chromospheric plasma [52], and larger-scale chromospheric jets [53].

Chapter 4

Magnetic measurements of individual flux tubes

> "The mind is its own place, and in itself can make a heav'n of hell, a hell of heav'n."
>
> — Satan (in John Milton's *Paradise Lost*)

In the previous chapter, it was assumed that the plasma loop had the magnetic structure of an arched flux tube. This was a well-justified assumption, due to the preponderance of circumstantial evidence. To name just a few examples:

- Magnetized plasma guns are a well-established method for creating plasmas whose magnetic field is a combination of the vacuum field and the field generated by the plasma current. For the geometry of the quad gun, this means an arched flux tube.
- The bright, high-density loop implies a ∇P that must be balanced by the appropriate $\mathbf{J} \times \mathbf{B}$ forces.
- Ejection of plasma from loops in the kinetic jet regime is consistent with ions failing to satisfy a stability condition for confinement in an arched flux tube [5].

One of the benefits of laboratory experiments, though, is being able to back up the circumstantial evidence with direct measurements. The chapter presents measurements of the loop's magnetic structure, which is found to be consistent with that of nested, helical magnetic fields.

4.1 Measuring the three-dimensional magnetic field

The magnetic field is measured with the array of B-dot probes described in Section 2.3.3. Figure 4.1 shows an example of the data collected for a left-handed and for a right-handed nitrogen loop. In

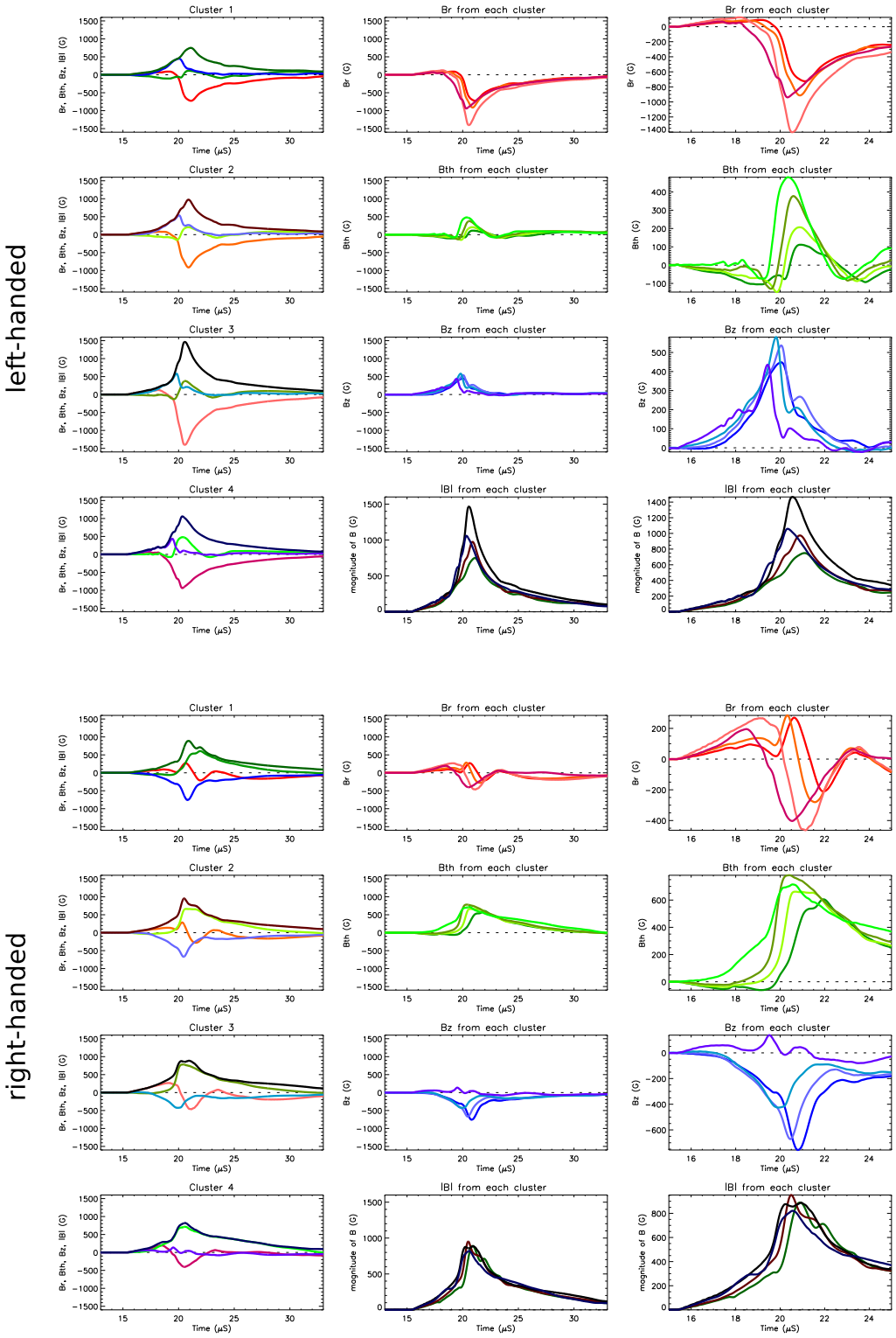

Figure 4.1: Magnetic data for a single nitrogen loop — left-handed (top) or right-handed (bottom) — taken with probe in the uppermost of the five standard positions *(shots 5892 and 5896)*

the first column, the traces are grouped by probe cluster. In the second column, they are grouped by component (in the probe's $r\theta z$ coordinate system). The third column replots the arrangement of the second column with auto-scaling of the vertical axes. The same color scheme is used throughout, with the B_r components in shades of red, the B_θ components in shades of green, the B_z components in shades of blue, and the magnitude of total magnetic field $|B| \equiv (B_r^2 + B_\theta^2 + B_z^2)^{1/2}$ shown in darker colors.

With a bit of foresight, the following features can be noted:

- Different traces tend to exhibit different degrees of unipolar "sine-like" and bipolar "cosine-like" character.
- Within any given component, there are clear quantitative trends from cluster to cluster, while the qualitative character tends to be similar across the clusters.
- The B_r components of the right-handed loop resemble the B_θ components of the left-handed loop, but opposite in sign, and vice versa.
- The left-handed loop has positive B_z traces while the right-handed loop has negative B_z traces (except for cluster 4).

Since the probe arm was up in front of the cathode, this last feature in particular lends itself to a ready explanation: the z-component probes detected part of the axial magnetic field of the loop (provided by the vacuum field and then frozen into the plasma), which would be pointing away from the cathode for a left-handed loop and toward the cathode for a right-handed loop. (Cluster 4 appears to have been directly in the path of the right-handed loop's local maximum distance from the electrode — i.e., the "hump" on that side of the kink — and therefore experienced almost no magnetic field in the z direction.)

The sign-flipped "swapping" of the B_r and B_θ components is attributable to the kinked structure. Naively, one would expect reversing the vacuum field to flip the sign of cosine-like traces (presumably associated with the axial field) and leave unchanged sine-like traces (presumably associated with the current, which always flows in the same direction). Due to the kink instability, however, reversing the vacuum field also changes the position of the loop axis in space — by, it appears, about 90 degrees.

Figure 4.2a–b illustrates this with sketches of the "mirror S" and "S" shapes associated with "top down" views of the axes of left-handed and right-handed loops, respectively. Alongside each

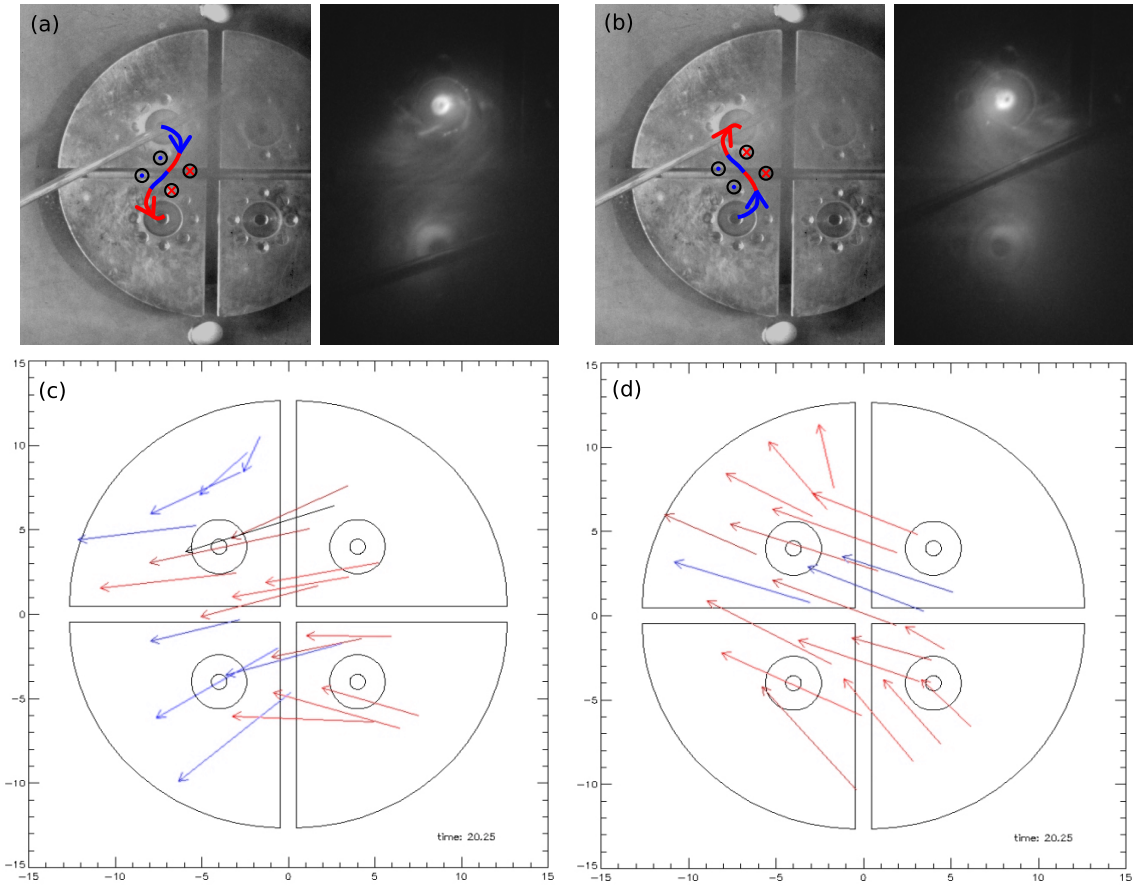

Figure 4.2: a–b.) Sketch and photo of a left-handed nitrogen loop and a right-handed nitrogen loop at $\sim$ 1.5 μs after breakdown *(shots 5863 and 5907)*. Within each sketch, sections of the axis are colored red/blue to indicate where the axial field will have a z component toward/away from the electrode. (The "color-reversed" middle section of each axis indicates the kink.) The blue dots and red Xs alongside the axes indicate out-of-plane and into-plane azimuthal magnetic field (produced by a current flowing from anode to cathode along the axis). c–d.) Planes of corresponding magnetic measurements taken $\sim$ 4.88 μs after breakdown (about when the total magnetic fields are at their maxima). Each vector field combines data from five shots. *(shots 5891, 5888, 5887, 5882, 5874; shots 5894, 5897, 5902, 5920, 5923)*

sketch is a "top down" image of the plasma (taken from the window in the opposite end dome) that displays striations with the same shape.

Recall that the data in Figure 4.1 incorporate the angle of the probe arm, which A.) can be changed, and B.) is not aligned with the midplane of the electrodes). To obtain a more objective picture of the spatially dependent magnetic field of plasma loops, data were taken for five positions of the magnetic probe, each set of magnetic data was transformed into the xyz coordinate system of the electrodes (using Equations 2.5 and 2.6), and the time-dependent quantities were displayed as vector animations to illustrate how they change over the course of a plasma loop's evolution.

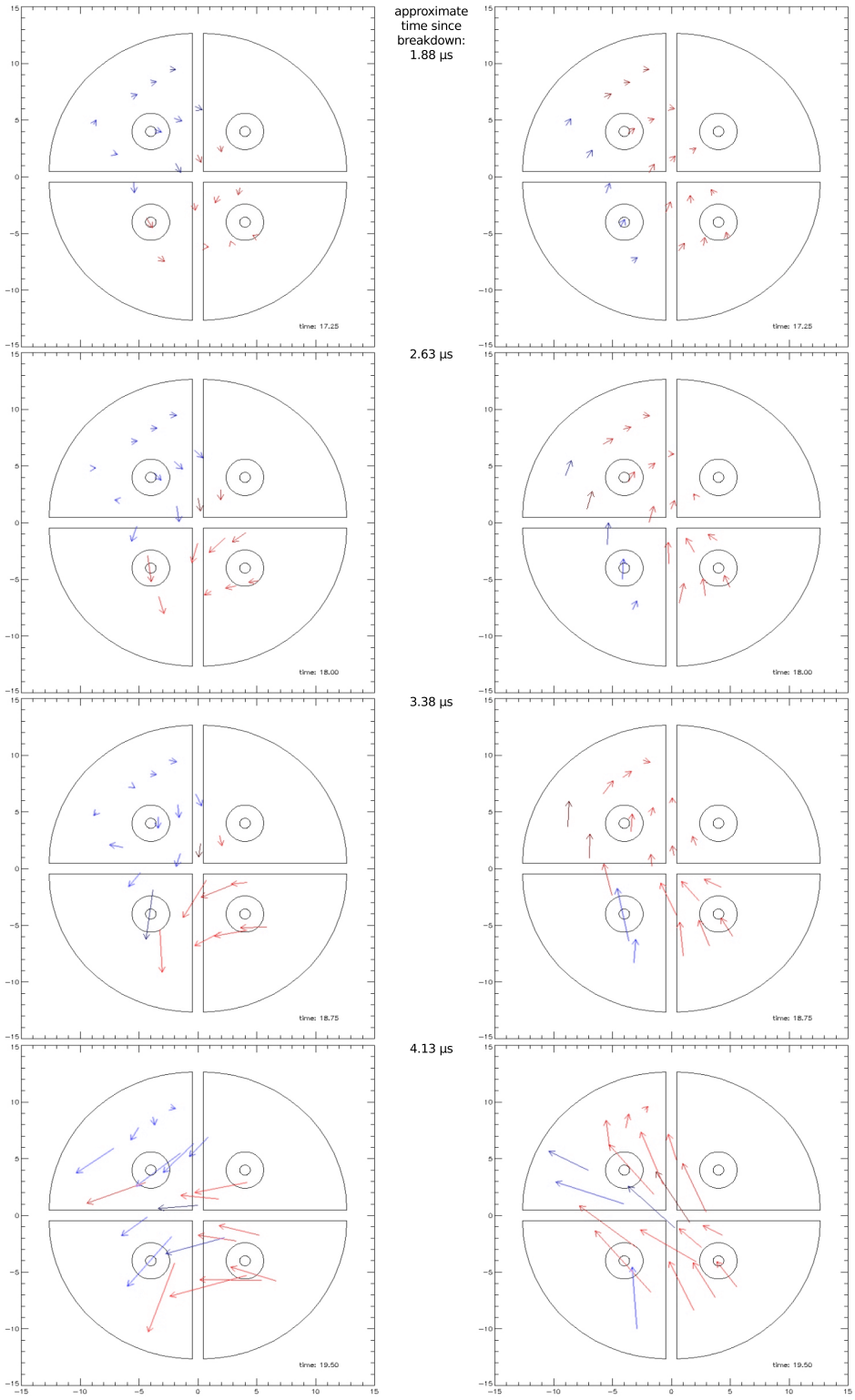

Figure 4.3: Earlier frames in the vector field animations shown in Figure 4.2c–d

Figure 4.2c displays one frame from the animation for a left-handed nitrogen loop, and Figure 4.2d displays the corresponding frame for a right-handed loop. Each arrow is positioned with its midpoint at the center of its associated probe cluster. The arrow's dimensions are proportional to that cluster's B_x and B_y measurements, and the color indicates B_z via a logarithmic scale in which bluer arrows indicate larger B_z pointing away from the electrode (out of the page) and redder arrows indicate larger B_z pointing toward the electrode (into the page). The frame time is such that the magnetic field magnitudes B_n ($n = 1, 2, 3, 4$) were near their maxima — i.e., when the flux tube was passing the probe arm. For comparison, Figure 4.3 shows frames in the same vector field animations from earlier times.

The vector fields for the left-handed loops are not perfect mirror images of the vectors for the right-handed loops. One major reason for this is that the probes' locations are not symmetric with respect to the horizontal plane across which one would expect the loops' axes to exhibit mirror symmetry (as shown in the sketches in Figure 4.2a–b).

Once this aspect of the measurement is taken into account, many elements of the expected symmetry can, in fact, be identified. For example, the dividing line between blue and red arrows at early times (1.88 and 2.63 μs after breakdown) is at about a 45-degree angle with horizontal for the left-handed loop, and about 135-degree angle with horizontal for the right-handed loop. These are along the lines of one would expect to see for the azimuthal field of a current with a "mirror S" or an "S" shape, respectively, whose axis is still located some distance from the probe centers. (Compare to the blue dots and red Xs in the sketches in Figure 4.2a–b.)

As one final example of the vector plane representations, Figure 4.4 shows four frames in the animation of magnetic fields for a right-handed hydrogen loop. Interesting features include:

- a dearth of blue arrows at the time when fields are largest ($\sim$4 μs), indicating that the axis is off to the side of the probe area
- subsequent ($\sim$5 μs) red/blue division suggesting a kinked structure
- back-and-forth oscillations of the arrows at later times (5-6 μs), during or after which the plasma ceases to have a single clearly defined loop structure in images

This last feature is of particular interest for future study, considering plasmas' infamous propensity to host a variety of different types of waves.[1] It has been observed only in hydrogen loops, for rea-

[1] One visitor to a conference poster that included plots of magnetic field traces such as those shown in Figure 4.1 claimed to be able to see Whistler wave vortices in the data.

sons that have not yet been determined. (For additional information about the variation in magnetic measurements from one species of plasma loop to another, see Appendix E.)

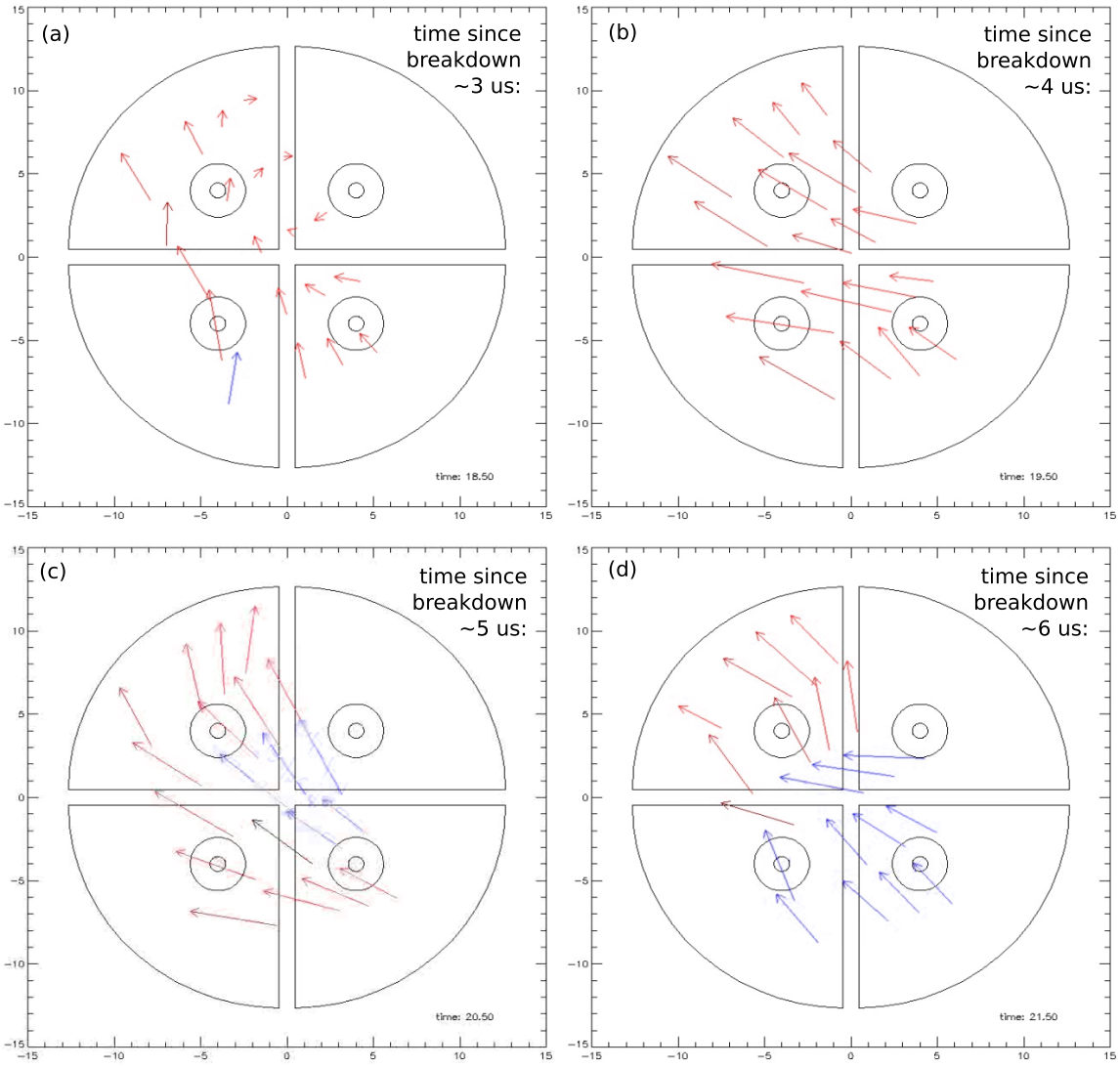

Figure 4.4: Evolving plane of magnetic field vectors measured from right-handed hydrogen loops. *(shots 5774, 5766, 5760, 5770, and 5772)*

4.2 Comparison to a force-free cylinder

Given the inherent difficulties in interpreting the experiment's magnetic data and in trying to predict what the data "should" look like, based on the not-fully-known shape and position of a growing, kinked loop . . . consider a simpler model. A much simpler model, in fact: an infinitely long, perfectly cylindrical, force-free flux tube — a situation examined by Lundquist in 1950 [54].

Recall that force free is not the same as force balanced (i.e., equilibrium). Whereas force balanced means $\mathbf{J} \times \mathbf{B} = \nabla P$, force free means that both $\mathbf{J} \times \mathbf{B}$ and ∇P equal zero. Pressure is uniform throughout, current flows precisely along magnetic field lines, and

$$\nabla \times \mathbf{B} = \lambda \mathbf{B}. \tag{4.1}$$

The plasma loops against which the model is to be compared are not force free. However, the force free model provides an elegant analytical solution, while offering qualitative similarity to other current distributions that need not be force free (a topic to be addressed in more detail later).

In a cylindrical coordinate system ($r\phi\, z$), Equation 4.1 is solved by

$$\begin{aligned} B_z &= B_0\, J_0(\lambda r) \\ B_\phi &= B_0\, J_1(\lambda r) \end{aligned} \tag{4.2}$$

where B_0 is a constant and J_0 and J_1 are Bessel functions of the first kind (see Figure 4.5a).

This solution represents nested coaxial current channels with helical currents of varying inclination. For example, consider the case of constant $\lambda > 0$ (that is, $\mathbf{B}$ and $\mathbf{J}$ are parallel, rather than antiparallel) and $B_0 > 0$ (the magnetic field is in the $+z$ direction at $r = 0$). For $\lambda r < j_{01}$ (the first zero of J_0), the axial current J_z is positive. For $j_{01} < \lambda r < j_{02}$, J_z is negative, and so on.

Applying the boundary conditions that $B_0 > 0$; that the axial current J_z only flows in one direction ($J_z \geq 0$ for all r or $J_z \leq 0$ for all r); that the current channel has radius A, at the edge of which J_z (along with B_z) goes to zero; and that B_ϕ is continuous at $r = A$, Equations 4.2 yield

$$\begin{aligned} B_z &= \begin{cases} \frac{\mu_0 I}{2\pi A J_1(j_{01})} J_0(\frac{j_{01} r}{A}) & \text{for } r \leq A \\ 0 & \text{for } r > A \end{cases} \\ B_\phi &= \begin{cases} \pm\frac{\mu_0 I}{2\pi A J_1(j_{01})} J_1(\frac{j_{01} r}{A}) & \text{for } r \leq A \\ \pm\frac{\mu_0 I}{2\pi r} & \text{for } r > A \end{cases} \end{aligned} \tag{4.3}$$

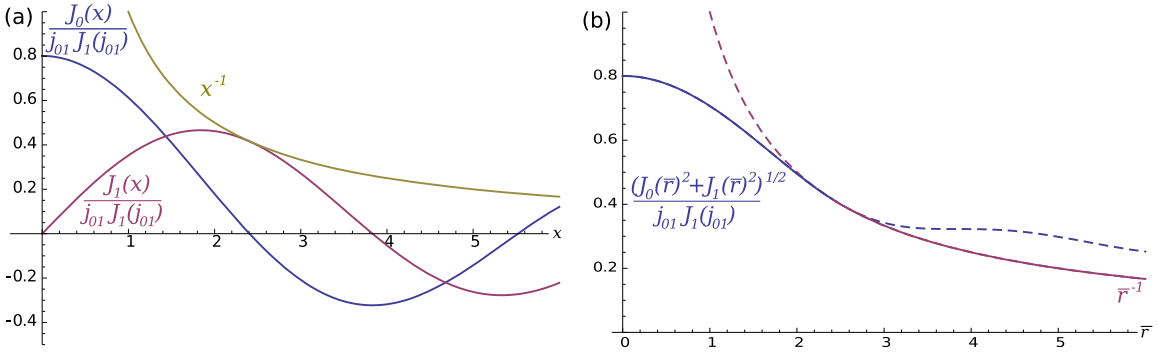

Figure 4.5: a.) Plots of scaled Bessel functions and $1/x$. b.) $|\bar{B}(\bar{r})|$ (solid line) and the discarded portions of its component functions, as given by Equation 4.4

where the sign of B_ϕ corresponds to the sign of λ. Ampere's law was used to solve for the magnetic field outside the current channel, and $I = \int_0^A |J_z| \mathrm{d}r$ is the magnitude of the total axial current flowing through the channel (i.e., the cylinder). $J_1(j_{01})$ is a constant approximately equal to 0.52. Expressed in dimensionless variables, this becomes

$$\bar{B}_{\bar{z}} = \begin{cases} \frac{1}{j_{01}J_1(j_{01})} J_0(\bar{r}) & \text{for } \bar{r} \leq 1 \\ 0 & \text{for } \bar{r} > 1 \end{cases} \qquad (4.4)$$

$$\bar{B}_{\phi} = \begin{cases} \pm\frac{1}{j_{01}J_1(j_{01})} J_1(\bar{r}) & \text{for } \bar{r} \leq 1 \\ \pm\frac{1}{\bar{r}} & \text{for } \bar{r} > 1 \end{cases}$$

where $\bar{r} = j_{01}r/A$ and $\bar{\mathbf{B}} = 2\pi\mathbf{B}/(\mu_0 I j_{01}/A)$.

In order to "take data" from this model, a virtual "magnetic probe" is moved through (or past) the flux tube[2]. How the probe is oriented and what path it follows relative to the flux tube's natural coordinate system must be taken into consideration. As shown in Figure 4.6, the probe might not pass through the center of the flux tube, and its coordinate system might not line up with the flux tube's coordinate system.

The probe might also follow a path that is not perpendicular to the flux tube axis (i.e., going through at a slant). Since the flux tube is infinitely long, however, the probe cannot distinguish between going through at a slant and going through perpendicularly but more slowly. One $\bar{z}$ coordinate looks the same as any other, and only velocity in directions perpendicular to the flux tube axis is detectable. Therefore, assume that probe moves in a path perpendicular to the flux tube axis.

[2]The choice has been made to move the probe relative to the flux tube rather than moving the flux tube relative to the probe. The two approaches give equivalent results (the relative velocity is all that matters), but the infinitely long flux tube seemed like it would be a bit more unwieldy.

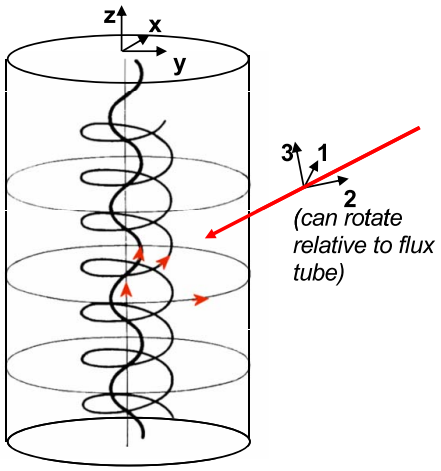

Figure 4.6: "Taking data" from an infinite, straight flux tube

The introduction of the possible offset (or impact parameter) between the probe path and the flux tube axis breaks the cylindrical symmetry of model and suggests a new coordinate system. Let $-x$ be the direction in which the probe is traveling, making y be the direction in which the probe path is offset by a distance b to the "right" of the flux tube axis (which will be rechristened z sans bar[3]), where all distances are understood to be in dimensionless units. In the Cartesian coordinate system, the dimensionless magnetic field is given by

$$\begin{aligned} B_x &= \frac{y}{\rho}\bar{B}_\phi \\ B_y &= -\frac{x}{\rho}\bar{B}_\phi \\ B_z &= \bar{B}_{\bar{z}} \end{aligned} \tag{4.5}$$

where $\rho = (x^2 + y^2)^{1/2}$ and $\bar{B}_\phi$ and $\bar{B}_{\bar{z}}$ are given by Equations 4.4.

Last but not least, $\mathbf{B}(x, y, z)$ must be transformed into the probe coordinate system $\mathbf{B}(r_1, r_2, r_3)$, as illustrated in Figure 4.6. The relationship between the two is given by

$$\begin{bmatrix} B_1 \\ B_2 \\ B_3 \end{bmatrix} = \mathbf{R} \begin{bmatrix} B_x \\ B_y \\ B_z \end{bmatrix} \tag{4.6}$$

[3]To be clear, z and B_z are being *redefined* as dimensionless versions of their former selves. Take care not to confuse the old z and B_z (which had dimensions) and the new ones (which do not).

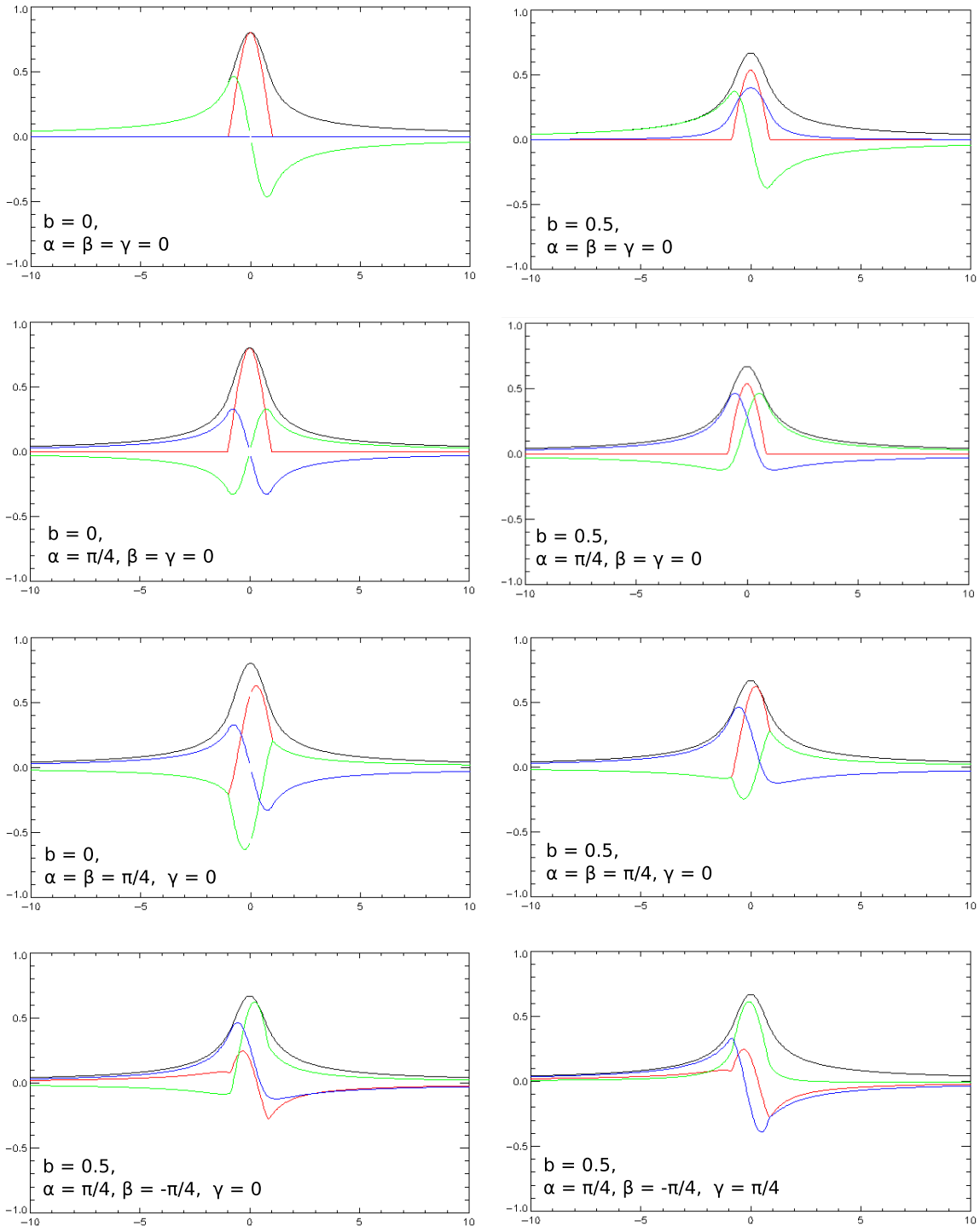

Figure 4.7: "Walking through" a flux tube at various angles and impact parameters. The components B_1, B_2, and B_3 are shown in blue, green, and red, respectively. The horizontal axes are in units of time (or, equivalently, position).

where

$$\mathbf{R} = \begin{bmatrix} c_\beta & c_\alpha s_\beta & s_\alpha s_\beta \\ -c_\gamma s_\beta & c_\gamma c_\alpha c_\beta - s_\alpha s_\gamma & c_\gamma s_\alpha c_\beta + s_\gamma c_\alpha \\ s_\gamma s_\beta & -s_\gamma c_\alpha c_\beta - s_\alpha c_\gamma & -s_\gamma s_\alpha c_\beta + c_\alpha c_\gamma \end{bmatrix} \tag{4.7}$$

represents a rotation α about the x axis, followed by a rotation β about the new z axis, followed by a rotation γ about the new x axis (with abbreviations used for all of the sines and cosines of the three angles).

Figure 4.7 shows virtual data for the probe moving with constant velocity $v = 1$. Lacking any other definition for it, $t = 0$ is defined as the time at which the probe passes closest to the flux tube axis. An impressive variety of magnetic traces can be achieved from only a few options for the parameters.

Of particular note are the two plots in the top row. They illustrate how, even without any rotation, a finite impact parameter makes axial magnetic field "look like" azimuthal magnetic field (in that it shows up as a unipolar signal in B_x). Therefore, when examining magnetic data, one cannot identify axial field based on signal polarity alone.

The most significant differences between the model and the magnetic traces are due to the model using a constant current. To better compare the two, let

$$I(t) = -I_0 \sin\left((t - t_{on})2\pi/\tau\right) H(t_{on}) \tag{4.8}$$

where the Heaviside step function $H(t_{on})$ "turns on" a sinusoidal current profile with amplitude I_0 at time $t = t_{on}$. I_0 instead of I will now be used for the dimensionless scaling of $\mathbf{B}$. Time now has a scale (that of τ, the period of the current profile), but $t = 0$ is still the time of closest approach.

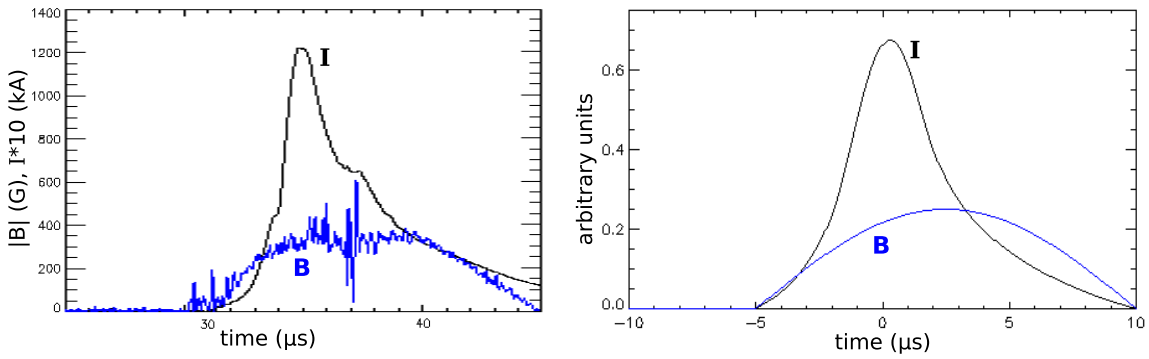

Figure 4.8: Plots of data (left) and model (right, with $\tau = 30$ μs) current and magnetic field magnitude versus time *(shot 5734)*

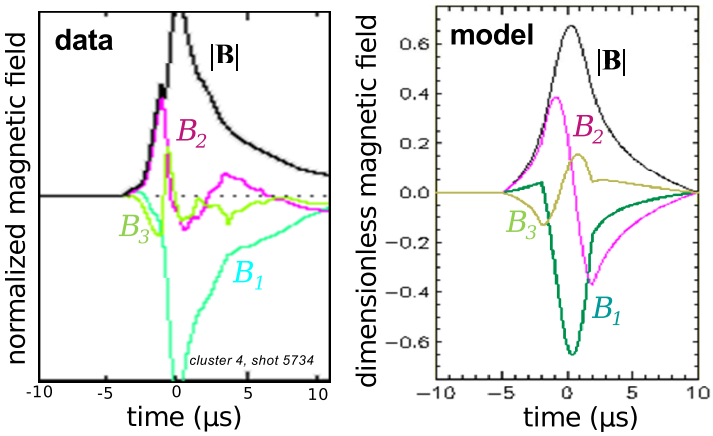

Figure 4.9: Flux tube experimental data and model (v = -0.5, b = 0.25, α = -2π/3, β = -π/5, γ = 3π/4). Note that the bright, collimated plasma loop is present only for the first 5–6 μs after breakdown, when the agreement is most pronounced. *(shot 5734)*

Figure 4.8 shows how this change gives the model's total magnetic field $|\mathbf{B}|$ the same faster rise and slower fall off that is characteristic of the experimental data. Figure 4.9 further shows that, by using that same $I(t)$ and then adjusting the parameters (angles, velocity, and offset), a very good qualitative match can be found for experimental data.

Hence, the plasma loop does indeed seem to have a magnetic structure of nested helices with the character — if not the exact form — of a force-free flux tube.

4.3 Calculation of current channel width from magnetic data

Having matched the experiment data to the flux tube model, one can estimate the size of the current channel by converting from the dimensionless units of the model to real distance.

From the period of the sine function, the model time is already measured in microseconds, and the definition of the problem stated that distances are normalized to the flux tube radius A. Velocity is therefore measured in tube radii per microsecond, so if the velocity of the flux tube in the laboratory is 50 km/s, while the velocity in the simulation is 0.5 tube radii per second for a good match, that means that

$$\begin{aligned} .5\ A/\mu\text{s} &= 50\ \text{km/s} \\ A &= (50 \times 10^3\ \text{m/s}) \times (10^{-6}\ \text{s})/.5 \\ &= 10\ \text{cm}. \end{aligned}$$

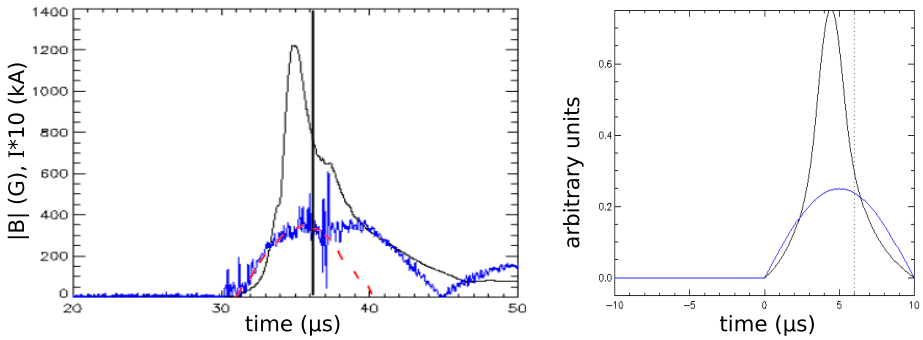

Figure 4.10: Proposed next refinement for flux tube model: ignore the later times after the clearly defined plasma loop is no longer present and fit the model to the early times (before the vertical black line in the left panel displaying the experiment data. The right panel shows $|\mathbf{B}|$ and I using this approach, and the narrower B peak shows promise.

This seems unreasonably large, and given how much wider the model $|\mathbf{B}|$ peak is than the corresponding data peak (as is especially evident in Figure 4.8), it seems likely that the model has room for quantitative improvement in this regard. Figure 4.10 suggests a modified approach that might yield better results.

A second estimate can be made by comparing the length of time between positive and negative peaks of bipolar magnetic traces to the rate of nitrogen loop major radius expansion, as calculated from the loop length expansion rate $\dot{l}(t)$ at the time when the loop encounters the probe arm. (Note that although a finite offset b can allow azimuthal field to "masquerade" as axial field, the same is not true in reverse.) This gives the flux tube diameter as

$$2A \approx \frac{\dot{l}(t = 5\ \mu\text{s})}{\pi} t_{reversal} = \frac{26.1\ \text{cm}/\mu\text{s}}{\pi}(1.3\ \mu\text{s}) = 10.8\ \text{cm}$$

which implies a radius of half the first estimate.

A third estimate can be made by considering cluster-to-cluster variations. For example, in the left-handed loop shown in the top section of Figure 4.1, the maximum total magnetic field was recorded at cluster 3. Cluster 2, which is 2 cm away, experienced at most about two thirds as large a field. Clusters 4 and 1, both 4 cm away, experienced about two thirds and about half, respectively, of the total magnetic field measured at cluster 3.

These values may be used as a alternate method to convert the horizontal axis of $|B_3|$ (in the vicinity of the peaks) from units of time to units of distance (assuming, that is, that the flux tube is not significantly "squashed" — i.e., narrower in one direction than the other). Since $|B_3(t)|$ is at two thirds its maximum about 0.5-0.75 μs before/after its peak, this suggests that a window of 1.0-1.5

μs corresponds to a distance of 2-4 cm. Recall that this was the size of time window associated with the reversal of the bipolar magnetic field components; hence, this estimate suggests that A = 2-4 cm, which is close to the size of the bright, collimated region observed in images.

4.4 Non-force-free current profiles

Two of the three estimates for the current tube minor radius are significantly greater than the observed radius of the bright loop. It is quite possible, though, for the radial extent of the current to be greater than the radial extent of the bright core.

In contrast to the force-free model that has uniform pressure everywhere, consider the radial pressure profile associated with a simple cylindrical pinch with radius A carrying uniform current density $J_z = I/(\pi A^2)$. If there is no axial field, the pressure gradient is given by

$$\begin{aligned} -\frac{\partial P}{\partial r} &= J_z B_\phi \\ &= \left(\frac{I}{\pi A^2}\right)\left(\frac{\mu_0 I}{2\pi A^2}\right) r \end{aligned} \tag{4.9}$$

which integrates to give

$$P(r) = \mu_0 \left(\frac{I}{2\pi A^2}\right)^2 (A^2 - r^2) \tag{4.10}$$

if $P(A) = 0$. The full width at half maximum (FWHM) of $P(r)$ is only 0.7 A. Furthermore, brightness scales as the square of the density[4]. Therefore, the radial profile of the brightness would would be proportional to $(1 - r^2/A^2)^2$, which has a FWHM of 0.54 A. Barely halfway out to the edge of the current channel, the brightness has already dropped by half.

For a pinch with a peaked current profile, the effect is even more dramatic. If the current density has a quadratic dependence $J_z = 2I/(\pi A^2)(1 - r^2/A^2)$, then the pressure profile is the rather unattractive

$$P(r) = \frac{\mu_0}{2}\left(\frac{4I^2}{\pi^2 A^4}\right)\left(\frac{5A^2}{24} - \frac{r^2}{2} + \frac{3r^4}{8A^2} - \frac{r^6}{12A^4}\right) \tag{4.11}$$

which already has a FWHM $\sim$ 0.5 A, so the density FWHM would be even narrower. Conversely, a "skin" current concentrated along the outer surface of the flux tube results in a uniform pressure profile inside.

[4]The physical mechanism for line emission involves collisions. Doubling the density, for example, doubles both the number of target particles (ions or neutrals) and the number of incident particles (electrons). Hence, it results in a fourfold increase in emission.

One might note that the force-free model has a peaked axial current profile not unlike that of the quadratic pinch . . . yet no pressure difference at all. The difference, of course, comes from the other component of ∇P. The pinches considered above do not have an axial field gradient (and associated azimuthal current), but the force-free model does; its $J_\phi B_z$ provides an outward contribution to the pressure gradient that exactly cancels out the inward contribution from the axial current and azimuthal field.

Theoretically, one could specify some axial magnetic field profile and then calculate the associated outward force $B_z(r)(\partial B_z/\partial r)/\mu_0$. In practice, a plasma tends to "decide" whether it want so be paramagnetic or diamagnetic and J_ϕ responds accordingly [1].

4.5 Summary

Even for the simplest case of individual plasma loops, the magnetic probe array measurements have a mesmerizing quality to them. Both the traces themselves and the vector animations generated from them contain a wealth of information in their dips, wiggles, and trends, suggesting the experimenter need only look carefully and cleverly enough to extract the entire picture.

They can be difficult to interpret, though — far more so than one might think they ought to be, given the deceptively simple picture of a single rope of helical magnetic fields. Even a perfectly straight flux tube carrying a time-independent current can yield "measurements" with dramatic asymmetries due purely to the offset and angles from which the fields are measured. The introduction of a curved, kinked axis would only be expected to further complicate matters.

Nevertheless, a straight force-free flux tube model using a time-dependent current produced a very good qualitative match to experiment data, indicating that the plasma loops are not inconsistent with a flux tube structure.

Calculations based on the magnetic measurements range from indicating a very wide current channel to suggesting one with a radius close to that of the bright region. It would not, however, be inconsistent to think of the plasma as having a dense core with minor radius a that may be half (or less) the size the current channel minor radius A.

Chapter 5

Beyond the individual arched flux tube, more and less

> "The most exciting phrase to hear in science, the one that heralds new discoveries, is not Eureka! (I found it!) but rather, 'Hmm... that's funny...'"
>
> — Isaac Asimov

Although a single arched flux tube is the most easily quantifiable structure that can be produced with the quad gun, there are a variety of other configurations that merit examination. These include single loops that aren't formed with a "proper" horseshoe shaped axial field, structures with three footpoints, and pairs of loops interacting with one another.

5.1 Single loops with unusual vacuum field configurations

Even from the very first image after breakdown, plasma arches emphatically display the vacuum magnetic field in which they are formed. Figure 5.1 shows this initial frame for four different magnetic field configurations. For the standard horseshoe vacuum field, the arch is already looking collimated, with the plasma confined inside. This is not the case for the other three, and the areas above the arches are brighter.

There are arch-like structures, though. In all three cases, the plasma does still stretch between the two electrodes — rather than extending straight out into the chamber. This is not surprising, given the large voltages involved. And each has distinct characteristics nevertheless.

The plasma for which only one coil was energized looks fairly normal at that footpoint, while at the other footpoint the hydrogen plasma is blob-like, rather than sleek. The plasma created without energizing any coils appears to already be kinking significantly. The plasma for which the two coils

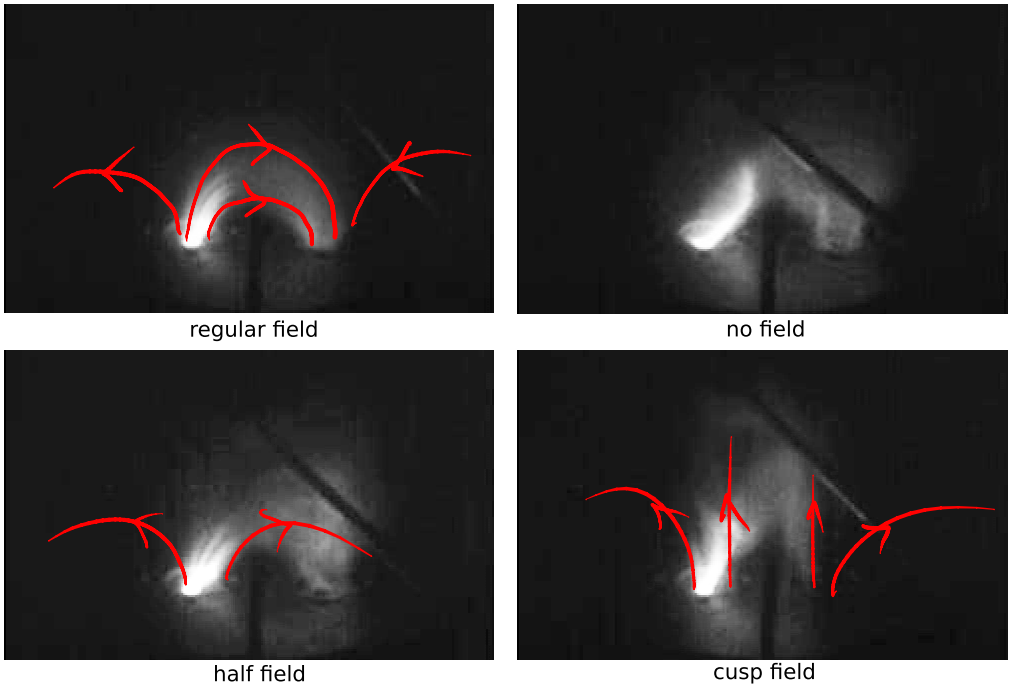

Figure 5.1: Initial arched plasma for different magnetic field configurations of an argon/hydrogen plasma *(shots 5732, 5750, 5742, and 5756)*

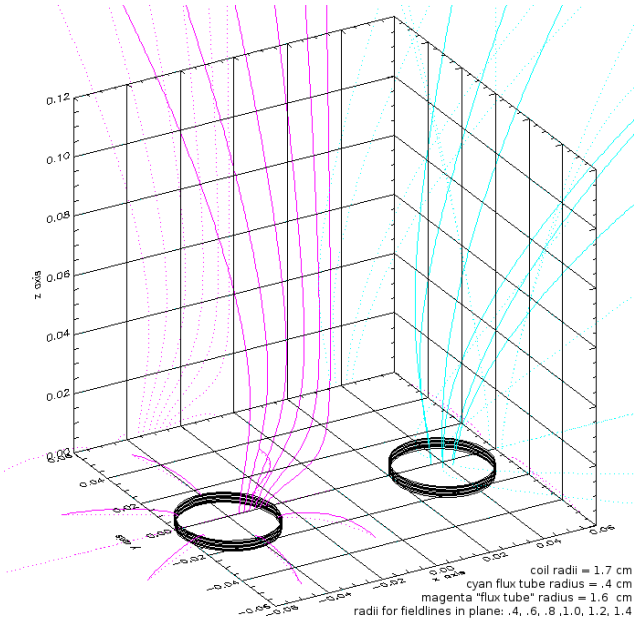

Figure 5.2: Magnetic field lines due to a pair of adjacent solenoids energized with the same polarity

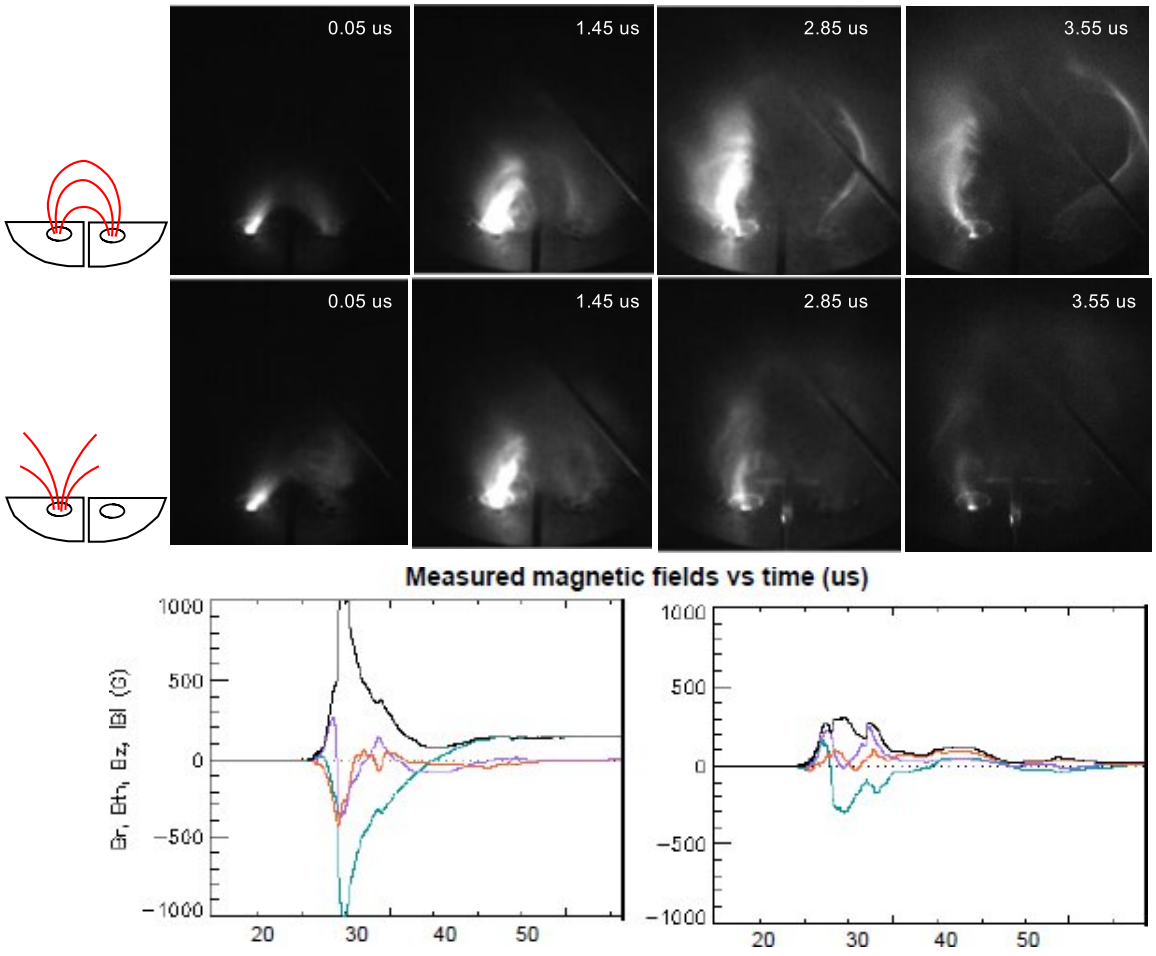

Figure 5.3: Evolution of an argon/hydrogen plasma arch with a standard vacuum field (first row; peak $I_{cap} = 35.4$ kA) and a "half" field (second row; peak $I_{cap} = 53.4$ kA) *(shots 5737 and 5739)*

were energized with the same polarity displays a cusp at its apex. (Note the similarity between its lower boundary and the shape of the rightmost magenta vacuum magnetic field line shown in Figure 5.2 that starts from a few millimeters inside the edge of the coil.) Plasma still appears to follow the magnetic field until it gets close enough to bridge the gap.

As these pseudo-arches evolve, most of them result in fairly diffuse plasma clouds, like the one shown in the second row of Figure 5.3. These structures tend to evolve more slowly than magnetic flux tube-equipped loops but have the same or larger capacitor currents. They are also significantly more variable in how rapidly that evolution occurs. Hence, the current proportionality and guarantee of image overlay feasibility are lost. The evolution is still very reproducible spatially, though.

Loops created without any vacuum field whatever are particularly unstable. The plasma arch in Figure 5.4, for example, appears to first pinch off at the hydrogen footpoint (frames 5–6), then

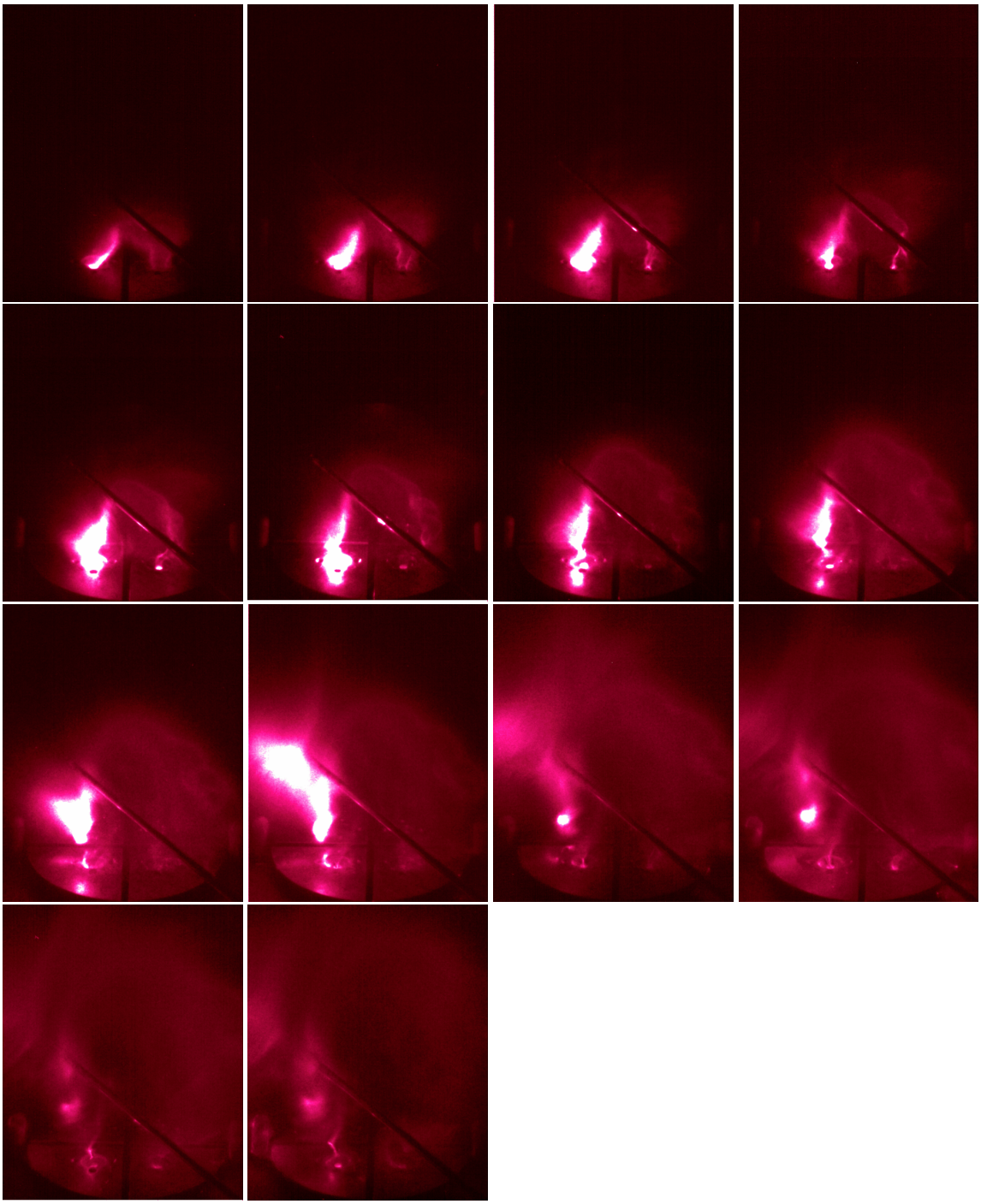

Figure 5.4: Plasma is ejected from an argon/hydrogen plasma for want of an axial magnetic field. *(shot 5749)*

pinch off at the argon footpoint (frames 8–9), then eject a large amount of argon via a kinetic jet (frames 9–11). In its wake, a helical structure seems to form, connected to the cathode by a very narrow, bright filament. Amazingly, this was not a one-time thing. The same sequence was repeated for every single zero-field shot in that sets of experiments.

Given axial magnetic fields' extensive contributions to the stability of magnetized plasmas[1], it should not be surprising that removing or otherwise tampering with the axial field can have consequences for the plasma dynamics. Nevertheless, it speaks to the importance of the magnetic flux tube structure of standard loops that its absence has such dramatic results.

5.2 Three-footpoint structures

On the sun's surface, active regions often involve pairs of sunspots: adjacent areas of opposite magnetic polarity that initially emerge together through the photosphere, each with highly concentrated magnetic flux. As an active region ages, though, the trailing sunspot will often spread out, so the magnetic flux from the leading sunspot now links to multiple smaller regions.

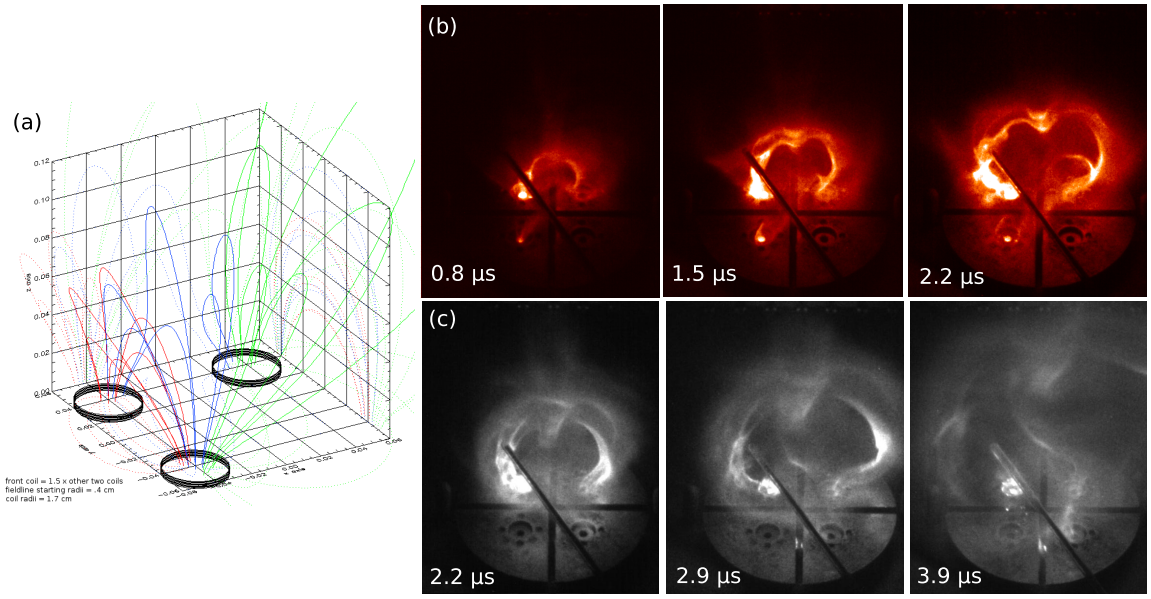

Figure 5.5: Three-footpoint structures: a.) Magnetic field line calculations provide an indication of to what extent the third coil can link with its diagonal neighbor. b.) An example of diagonal linkage occurring from very early times. c.) A configuration in which the third footpoint does not appear to get involved until later in the plasma shot *(shots 7876 and 7846)*

[1]In general, perturbing a plasma with an axial field requires more work than perturbing one without, due to the magnetic field line tension. The MHD kink and sausage are two prime examples of instabilities that can be stabilized by an axial field.

With these types of structures in mind, experiments were conducted to find out whether the quad gun could produce plasmas that linked one footpoint on one electrode to both footpoints at the other. The answer was "yes", with two distinct manifestations observed. Figure 5.5a shows an experiment in which bright plasma is seen spanning the diagonal from very early times. A fainter diagonal loop grows alongside the primary loop, with the branch uniting the two traveling up the leg of the structure from the anode.

In Figure 5.5b, on the other hand, the connection to the third nozzle is ambiguous at best, until much later in the shot when a bright tendril becomes visible in the center of the image. This tendril appears to link the apex of the loop to that third footpoint, where a thick column becomes the plasma's primary connection to the electrode as the original two legs dim/disconnect. When viewed as an animation, the plasma seems to "step" onto a new location.

5.3 Pairs of loops

Although pairs of plasma loops have been an ongoing topic of inquiry with the quad gun [55, 32], neither magnetic measurements nor dual-gas techniques (in which each of the two loops is made of a different species) had yet been brought to bear. Doing so both supported and extended past studies on loop interactions.

Results are shown in Figures 5.6 and 5.7. Along the left side of each figure are cartoon versions of the plasma configurations; these have been rotated by 90 degrees from the lab perspective so as to better match the images. Hence, the cathode is on the left, and the anode is on the right.

Cohelicity pairs of loops in which one loop was composed of hydrogen and the other from either nitrogen or argon tended to end with a conical-looking hydrogen cloud proceeding outward from the middle of the interaction region, while the loop made of the heavier species dispersed (Figure 5.6a-b)[2]. Broadened magnetic field traces were also observed (Figure 5.7b). The two loops definitely interacted, but appeared to do so comparatively "gently" (to the extent that multithousand amp currents can be called gentle).

The two different counterhelicity pairs, on the other hand, exhibited two extremes. In the configuration where the loop on the near side was right handed and the loop on the far side was left handed, so that their point of closest approach was near the anode, the loop made of the heavier species (either nitrogen or argon) brightened as it was split in half by the hydrogen loop as the two

[2]In nitrogen/neon pairs, nitrogen was the identified as the emitting central species. (Thus, even though individual neon loops appear faint and uncollimated, interaction with the adjacent nitrogen loops still occurred.)

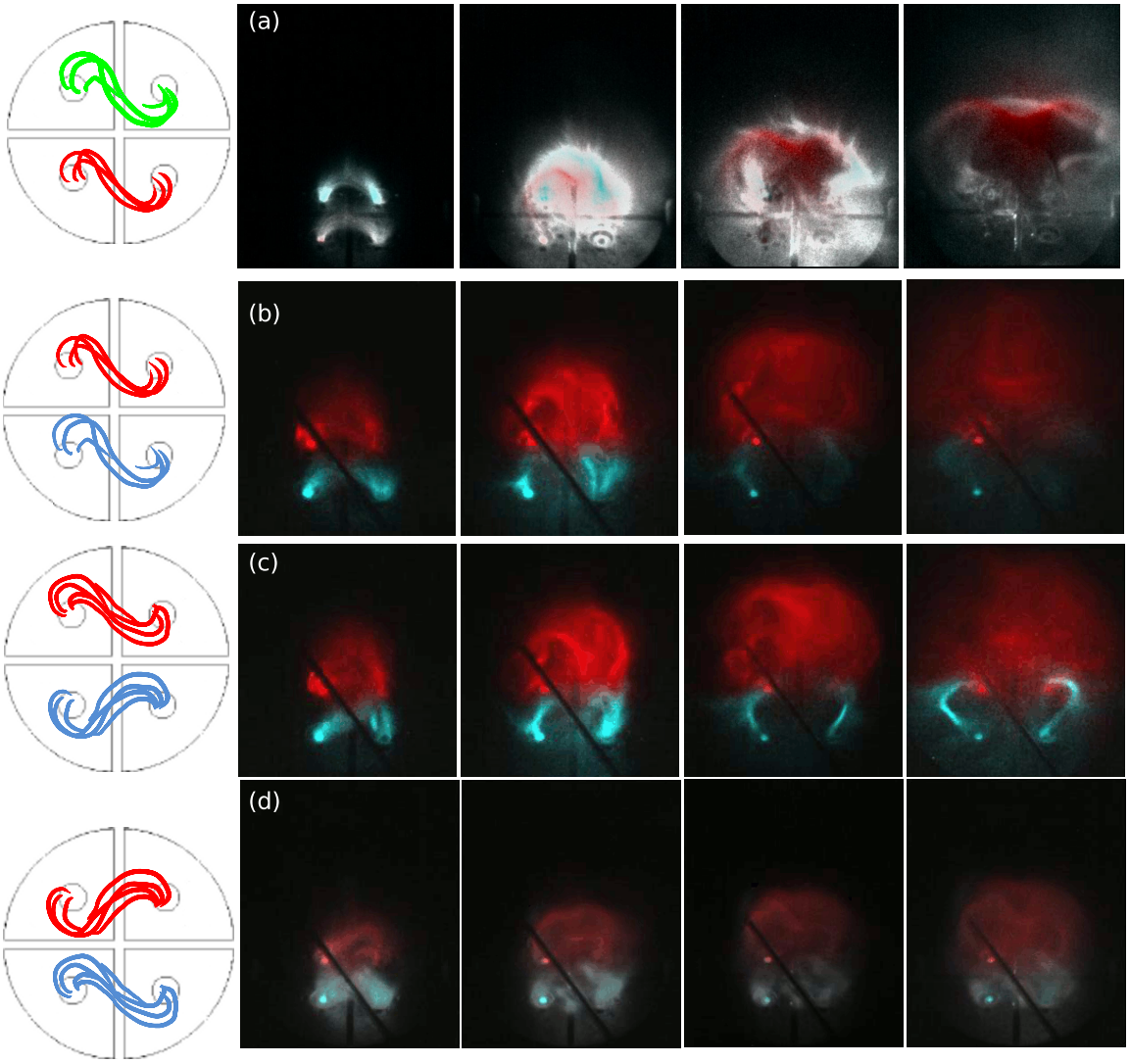

Figure 5.6: Pairs of loops of different species: one hydrogen/nitrogen pair and three argon/hydrogen pairs of various helicities *(shots 5357/5362/5360, 7716/7714, 7724/7726, and 7693/7703/7708)*

loops merged together (Figure 5.6c). Magnetic measurements were amplified and narrow (Figure 5.7c).

In the other counterhelicity configuration (where the loop on the near side was left handed), magnetic fields were barely detectable (Figure 5.7d), and the two species appeared to stagnate beside one another (Figure 5.6d). Somehow, this magnetic field configuration seemed to "short circuit" the normal plasma evolution. The disparity between the behavior of the two counterhelicity configurations had been identified before, but not quite so dramatically.

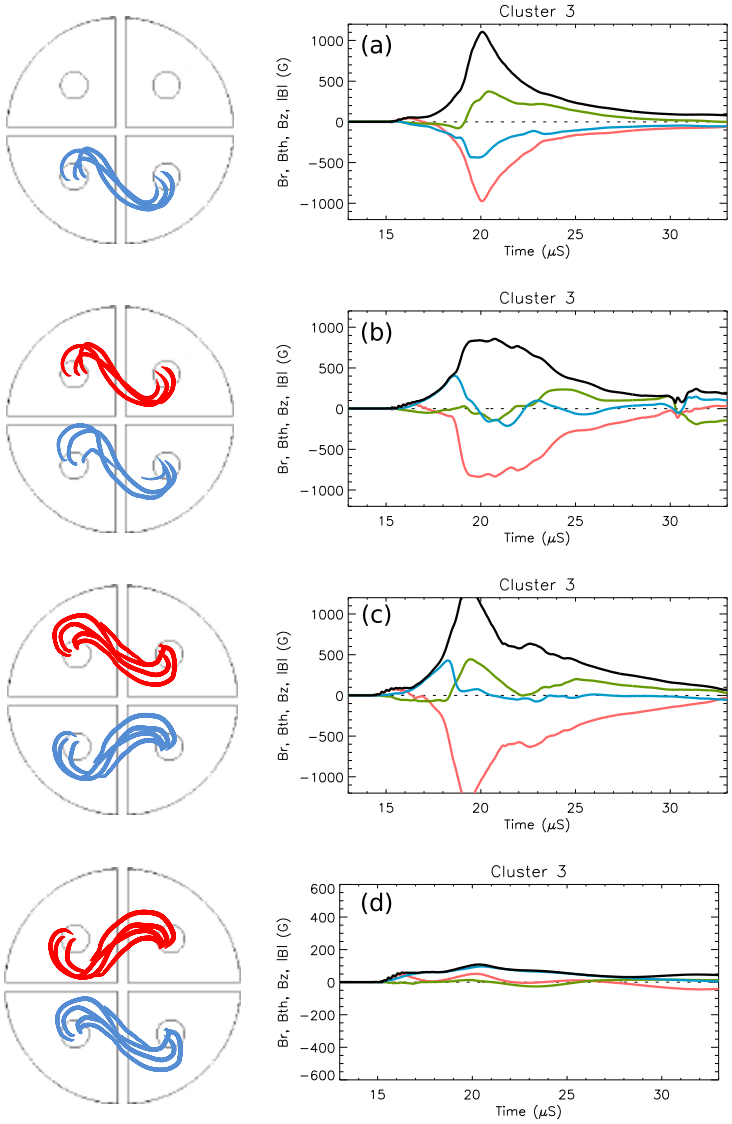

Figure 5.7: Magnetic fields of argon/hydrogen loop pairs, with argon single-loop data for reference *(shots 7695, 7719, 7727, 7693)*

Chapter 6

Conclusions and future work

> "Here there be dragons."
>
> — phrase allegedly designating areas on a map beyond the known world[1]

This dissertation offers experimental evidence that magnetohydrodynamically driven flows are an important mechanism for the transport of plasma and frozen-in magnetic flux in arched plasma structures in general, and plasma-filled magnetic flux tubes in particular. These structures are prominent features in plasma systems of significant interest, such as the solar atmosphere and magnetic fusion devices. As such, an understanding of the fundamental physics of their nonequilibrium dynamics comes with the promise of valuable practical applications in areas such as solar weather forecasting and fusion science.

The purpose of this chapter is to provide a brief summary of the work presented in this dissertation, as well as a discussion of new questions that have been raised and ideas for future work.

6.1 Summary of contributions

Experiments were conducted on the Mark IV solar gun in the Bellan plasma laboratory at Caltech (Chapter 2). Among the techniques newly brought to bear on this system were:

- the creation of dual-species plasmas,
- highly quantitative analyses of the parameters driving loop dynamics,
- 12-channel magnetic measurements of the three-dimensional magnetic field for a variety of plasma structures,

[1] Probably actually more historical fiction than historical fact, but worth perpetuating nonetheless.

- calculations of "virtual" magnetic flux tube data,
- the development of new software (e.g., image processing and tracking routines, calculations of magnetic field lines for various vacuum configurations, and many other data analyses),
- and the exploration of "exotic" magnetic field topologies.

Extensive measurements were made of individual plasma loops. The magnetic structure (Chapter 4) of the loops was found to be consistent with that of a flux tube, and their evolution (Chapter 3) was found to be in agreement with two interrelated MHD theories: a simplified hoop force model of axis expansion and the "gobble" model [47] of collimation.

Multifootpoint plasma structures (Chapter 5) may at first glance appear more chaotic than their high-contrast cousins. However, for any given vacuum field, the resulting plasmas were found to be quite consistent in what they did (if not necessarily how fast they did it). The dual-gas "plasma color coding" technique and the B-dot probe data provided new and interesting perspectives on these experiments.

In the course of this work, many parameters of the system were observed, measured, analysed, and/or calculated. Included in the appendices are reports on the vacuum magnetic field (Appendix A), fast gas valve operations (Appendix B), some of the system's circuit parameters (Appendix C), potential sources of uncertainty in the loop tracing method (Appendix D), species-dependent variations in single gas loops (Appendix E), alternative numerical integration schemes that were considered (Appendix F), and a statistical survey of important times in a plasma loop's evolution (Appendix H).

6.2 A shot illustrating the significance of the magnetic field topology

It has been argued throughout this dissertation that the magnetic field topology is very important. As one final illustration of this, consider the anomalous plasma experiment shown in Figure 6.1. The experiment setup was intended to be for a traditionally magnetized single loop, but one that spanned the diagonal of the gun instead of being confined to one half. By mistake, though, gas was released at only the footpoints where the vacuum field coils were *not* energized.

Breakdown occurred, but despite the 5 kV across the electrodes, it took the plasma almost 3 μs (quite a long time!) before it was able to form a cohesive-looking arch. The moral of the story is that the current may eventually find a path, regardless of the vacuum magnetic field configuration.

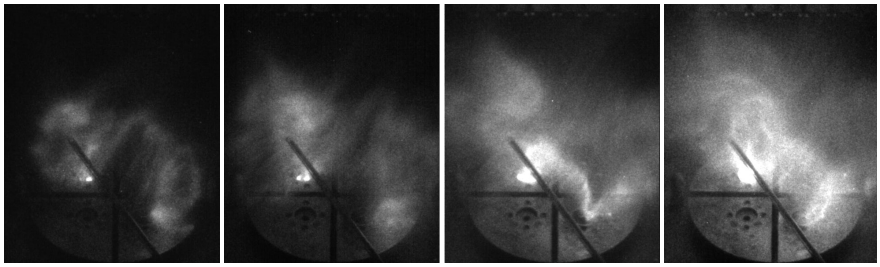

Figure 6.1: Evolution of the plasma that formed when gas was accidentally released from nozzles perpendicular to the magnetic field. (The vacuum field coils in the lower left and upper right quadrants of the image were energized, but gas was released from the nozzles in the upper left and lower right quadrants.) *(shot 7788)*

However, a strategically placed magnetic flux surface can make its life quite a bit easier, inducing it to follow a "straight and narrow" path (which may sometimes be rather kinked).

6.3 Future work

The most striking question that was raised as a result of the work in this dissertation is the mystery of where the majority of the main bank capacitor current flows.

In the case of single plasma loops (which lend themselves most readily to quantitative measurements), only about one tenth[2] of the total current flows through the bright, collimated flux tube. This estimate is in agreement with the magnitude of magnetic fields measured (Chapter 4), with the rate of loop expansion (Chapter 3), and with the voltage drop across the electrodes (Appendix C). Assuming that most of the current flows through the loop, by contrast, results in estimates for all three of these quantities that significantly disagree with measurements. The more complex topologies show no indications of carrying a significantly larger fraction of the capacitor current than do the single loops.

One promising explanation is that there is a low current density being conducted by the low-ρ plasma surrounding the bright, high-ρ structure. Because this low density current may be present over a much larger volume than the main plasma structure, it could in total conduct the bulk of the current while having little effect on the overall system dynamics.

Some preliminary evidence in support of this hypothesis comes from measurements of the vac-

[2]One tenth was the intermediate value predicted by Equation 2.2 and the measured magnetic fields. By choosing high estimates for both the loop's azimuthal field and its minor radius, one can calculate the fraction of the capacitor current flowing through the loop to be as high as one fifth, which would still leave 80 percent of the capacitor current unaccounted for.

uum magnetic field at the electrode surface (Appendix A). The magnetic flux through an entire quarter of the gun was found to be 2-3 times greater than the flux through the circular hole, 1.6 cm in radius, that is coaxial with the vacuum field coil and gas inlet. Thus, if current flowed in equal proportion along all magnetic field lines intersecting the front surface of the electrode, less than half the current would flow through that circular region. Of course, if the ratio of current density to magnetic field density were different for the low-ρ and high-ρ regions, that fraction could be higher or lower. Regardless, a relationship between current density and magnetic flux density would help to explain why the ratio of current through the loop appears to be approximately the same across different charging voltages and different plasma species.

There is also past precedent for fringing fields carrying significant amounts of current. For the Mark I gun, only at very early times did the plasma exhibit a bright arch at all; shortly thereafter, the structure bifurcated into twisted secondary structures that appeared to follow fringing fields for the rest of the experiment duration [56]. Although the newer gun designs produce plasma structures dominated by arches, it is possible that fringing fields through low-ρ plasma still conduct substantial current to the chamber walls.

Investigations into the amount of current flowing along fringing fields and/or other paths should be feasible, and should be able to resolve this question. A possible experimental strategy would be to ceramic covers over the electrodes, with 1- to 3-cm holes (allowing current to flow through) located only at the footpoints. Other approaches for tracking down the missing current may include:

- use of an individual prominence current system (IPC) composed of Rogowski coils that measure how much current flows through each side of the electrode (left versus right);
- solving for the electrostatic fields produced by applying voltage to the copper electrodes (and comparing these to the magnetic fields produced by the vacuum magnetic field coils);
- measuring the amount of current that flows to a copper plate installed over a port of the chamber, and/or
- disconnecting one half of the electrode from the main bank and then using it as a "copper plate" for a similar measurement.

Besides addressing the mystery of the missing current, there are several other avenues of inquiry suggested by this dissertation that may also be of interest:

1. Investigation into the differences observed between the two counter-helicity configurations.

2. Quantitative analyses of pairs of loops and other more-complicated structures with image-tracking methods akin to those used for the single loops.

3. Detailed, quantitative comparisons to specific solar features.

4. Continuing regular use of the magnetic probe array and efforts to deconvolve the data, with the goal of uniquely identifying flux tube properties from magnetic traces alone.

5. Using the Princeton cameras in their 3D imaging configuration again. This should be a valuable tool for combating the deceptive combination of projection effects and optical thinness.

Finally, it should be emphasized that analyses of arched plasma structures are greatly facilitated by examining images of the structures with their apex "up" — i.e., toward the top of the page/screen. (Presumably, "down" would work equally well.) By taking advantage of humans' inherent bias for horizontal symmetry, this approach allows the plasmas' symmetries and asymmetries to be more readily identified, investigated, and — ultimately — explained.

Appendix A

Measurements of the vacuum magnetic field

The vacuum magnetic field for the magnetized plasma gun is created by the iron-core coils described in Chapter 2. Several sets of measurements have been made of the field (three of which are described here). It can be illustrative to compare them to one another, as well as to iron-free solenoid calculations, toward the goal of getting a fuller picture of the magnetic environment in which the plasma forms.

A.1 Magnetic flux at the electrode surface

One measurement, done with Rory Perkins, used eight loops of wire on clear plastic sheet. Four loops traced out the outer edges of the circular openings in the electrode. The other four traced out quarter circles around each quadrant of the electrode. (This gave them areas of 8×10^{-4} m^2 and 110×10^{-4} m^2, respectively.) Voltages induced in the loops when the magnetic field coils were energized were read via the VME and numerically integrated to get measurements of magnetic flux.

Results for a standard single-loop configuration (one coil on top and one on bottom, each pulsed from a charging voltage of 200 V) are shown in Figure A.1a. The flux is concentrated in front of the nozzles, as one would expect; the large loops on the same side of the gun as the energized coils experienced only 2–3 times as much flux as the small loops, despite having almost 14 times the area. The loops on the opposite side of the electrode experienced very little flux.

Figure A.1b shows how the magnetic field varied in time as a function of charging voltage for one of the small loops in front of an energized coil. Experiments are nearly always done with stuffing bank firing voltages of 200 V, but it is important to be aware that upping the voltage should

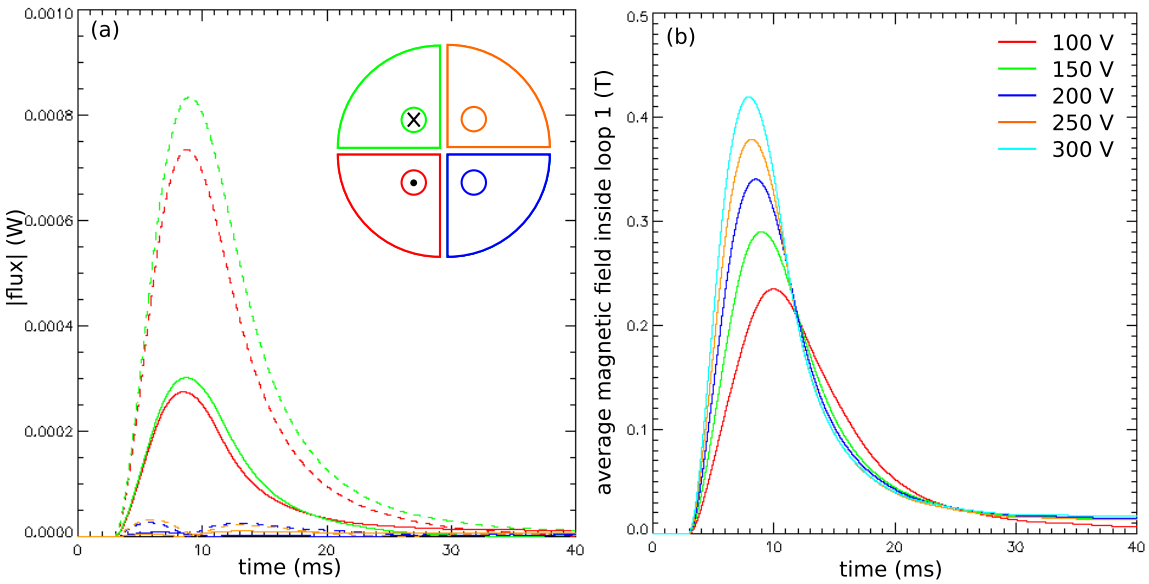

Figure A.1: a.) Flux magnitude versus time for each of the eight wire loops, when pulsed from a charging voltage of 200 V. Large loops are plotted with dashed lines, small loops with solid lines; both are colored by quadrant according to the inset diagram. Inset: The eight wire loops that were used to measure the vacuum magnetic field, as viewed from inside the chamber. The magnetic field, indicated by the black dot and X, was generated by energizing the two coils on the near side with a "right-handed" field. b.) Average magnetic field (flux divided by area) versus time for the small red loop, shown for a range of stuffing bank charging voltages

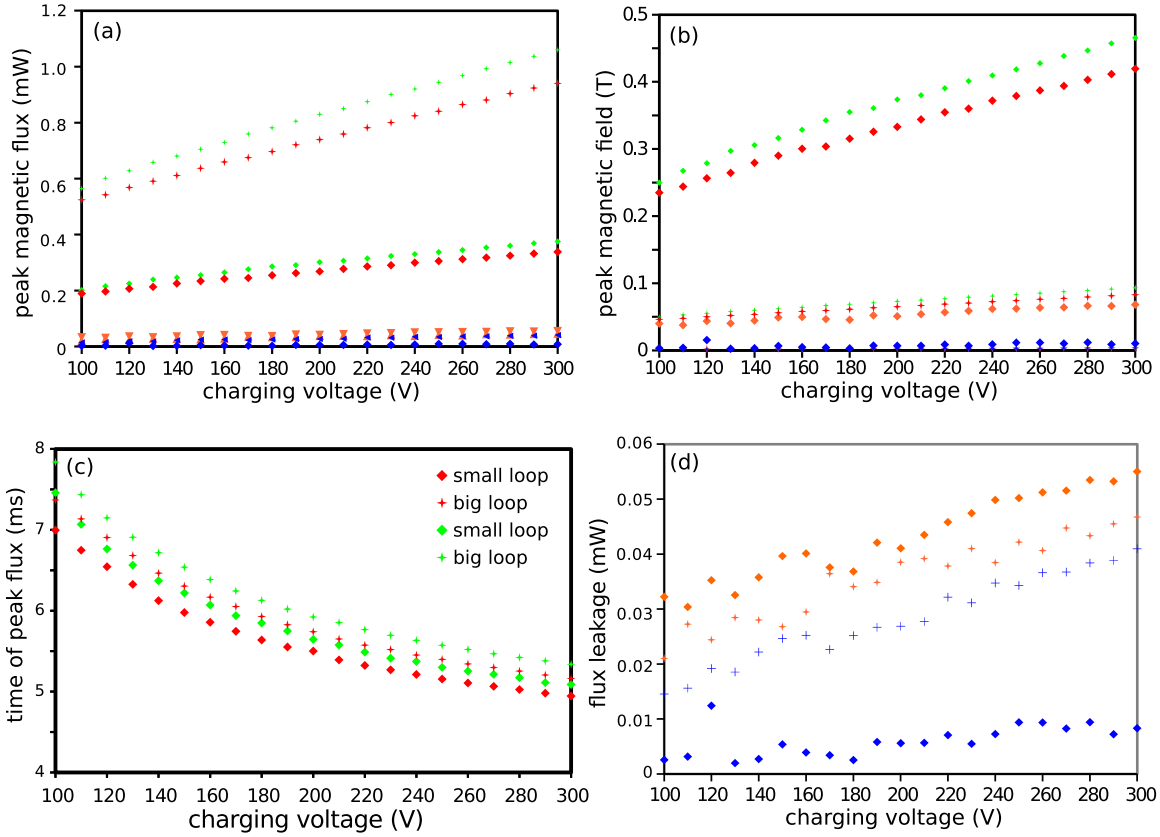

Figure A.2: Additional data from the same measurements described in Figure A.1, is plotted according to the eight loops' peak magnetic flux (a) and peak magnetic field (b). Colors are the same as in Figure A.1; small loops are indicated with diamond symbols and large loops with plus signs. c.) Time from when the flux first started to rise until it hit its peak, for the large and small loops in front of the coils that were energized. d.) The fluxes experienced by the loops in front of the coils that weren't energized. The specific values are somewhat questionable as the signals were noisy enough to confuse the numerical integration routine, but the bottom line is that they are negligible.

coincide with a decrease in the preprogrammed delay between the magnetic field timing and the high voltage timing.

Additional data from the same setup is shown in Figure A.2. In particular, panel (b) illustrates that the magnetic field is ~ 0.3 T at the footpoints of the arched vacuum field and quite low elsewhere in front of the electrode. Notably, this is little more than half that reported for the quad gun's Mark II predecessor (0.59 T), which had the same power supplies and coils [27]. However, the Mark II gun did have extra iron connecting the two cores in the coils, which could be at least part of the explanation. Panel (c) shows the dependence of vacuum field rise time on charging voltage; the result for 200 V is in agreement with the 5.6 ms previously reported [27].

The upper coil seems to produce a field that is 10–15 percent stronger than the lower coil; the

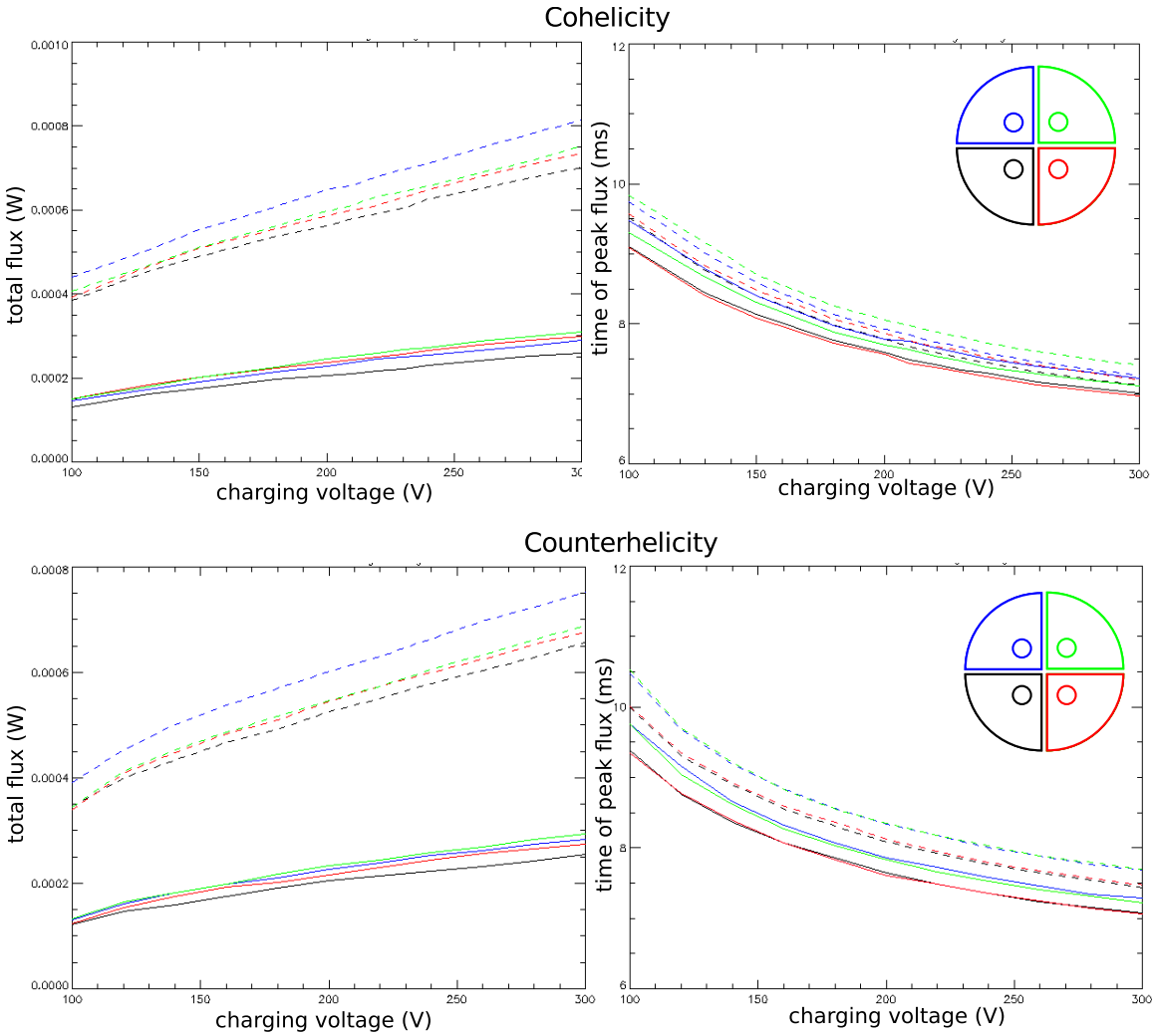

Figure A.3: Plots for a cohelicity and a counterhelicity configuration of the vacuum magnetic field coils analogous to Figure A.2's (a) and (c). Small loops are plotted with solid lines, and large loops with dashed lines; colors are assigned according to the inset diagrams. The times reported here are not adjusted for the delay between when data collecting was initiated and when the coils were energized; rise times can be calculated by subtracting those three milliseconds (see Figure A.1a). These data were taken and plotted by Rory Perkins, and are included here with his permission.

reason for this is unknown, but could perhaps be uncovered by examining the electrical properties of the two power supplies.

Rory Perkins also used the same setup of eight wire loops on a clear plastic sheet to take similar measurements of the flux produced when all four coils were energized, either in a cohelicity or counterhelicity configuration. For completeness, the data for these are shown in Figure A.3.

A.2 Vacuum field measurements with the magnetic probe array

While the wire loops described above were effective for measuring the magnetic field at the electrodes, where their geometry is appropriate, they would not provide much useful information if used farther out into the chamber. The magnetic probe array, on the other hand, has the spatial resolution to do this, and in addition provides data about the direction of the field.

Initial measurements were taken with Shreekrishna Tripathi shortly after the probe array was built. The two coils on the "near" side of the electrode were energized, each from a charging voltage of 200 V. The signal from one component at a time of probe cluster 2 was sent to an amplifier-integrator[1], since the signals would otherwise have been too small to measure. (The magnetic probes are typically used for the microsecond-scale changing fluxes of the experiment instead of the millisecond-scale changing vacuum magnetic field.) The amplifier output was then measured with

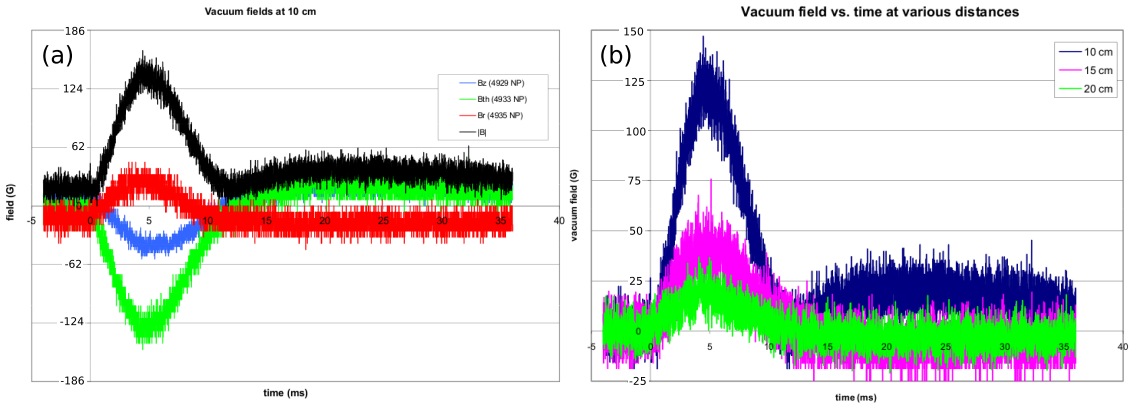

Figure A.4: Vacuum field measured with cluster 2 of the magnetic probe array, which was angled such that the arm intersected the horizontal midplane of the electrode directly in front of the midpoint between the two coils. a.) The total magnetic field and its three orthogonal components, plotted versus time, measured at 10 cm from the electrode. b.) The total magnetic field as a function of time, measured at increasing distances from the electrode. *Note: Compared to more recent data, these data are high by about a factor of two, most likely due to a calibration error.*

[1]Specs were as follows: LM 741 op-amp, 47 Ω resister, 0.2 μF capacitor, measured $V_{out} = -5 \times 10^5 \int V_{in} dt$.

an oscilloscope and converted to gauss when it was plotted.[2]

Results, shown in Figure A.4, suggested that the total magnetic field due to the energized stuffing flux coils falls off to $\sim$ 120 G (a little more than 3 percent of its strength at the footpoint on the electrode) by 10 cm into the chamber, and drops further to $\sim$ 40 G at 15 cm and $\sim$ 20 G at 20 cm. (Measurements could not be taken any closer to the electrode than 9.5 cm, the limit of the probe arm travel in that direction.) This is similar to measurements made on the Mark II gun [27].

Later, when it was established that cluster 2 would have been somewhat offset from the region directly in front of the energized coils, a second set of measurements was taken. The probe arm angle was very slightly higher, so that cluster 4 was precisely in the midplane between the electrodes (Figure A.5a). Data was recorded from all 12 probes in the array. A new amplifier-integrator was built using nearly identical components (A.5b), this time installed in a small aluminum enclosure to improve the signal-to-noise ratio. Results are shown in Figure A.6.

The new data led to the discovery of a sign error in the earlier measurement, as well as an apparent miscalibration of the first amplifier-integrator. Thus, the data in Figure A.6 are smaller in magnitude and the components opposite in sign compared to those in Figure A.6a. The former implies that the field of the Mark IV gun at 10–20 cm from the electrode, like the field at the electrode surface, is about half that of the Mark II gun.

Now that the locations of the magnetic probes in space had been established (something that was not yet done when the first set of data was taken), it became clear that while the B_θ traces in Figure A.6 have the expected sign, B_r and B_z do not. As it turns out, two of the three sets of probe coils are installed "backwards" (relative to the probe's natural/intended coordinate system). This is,

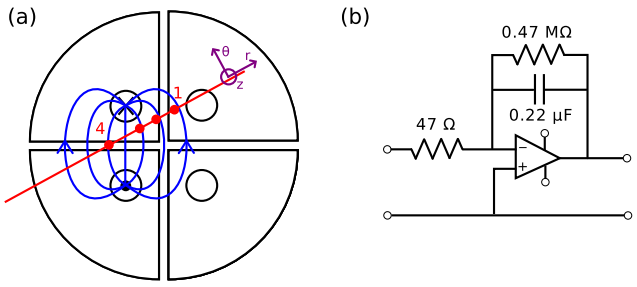

Figure A.5: a.) Cartoon of the approximate probe arm and probe cluster locations with respect to the electrodes and vacuum magnetic field. The coordinate system indicates the directions in which B_r, B_θ, and B_z were measured. b.) Circuit diagram for the amplifier-integrator

[2]According to Faraday's law, $B(t) = -\frac{1}{NA}\int V_{\text{probe}} dt = \frac{RC}{NA} V_{\text{output}}$ where V_{output} is the output from the amplifier-integrator. A value of $NA = 1.21 \times 10^{-4}$ m^2 was previously measured for this model of coil [34].

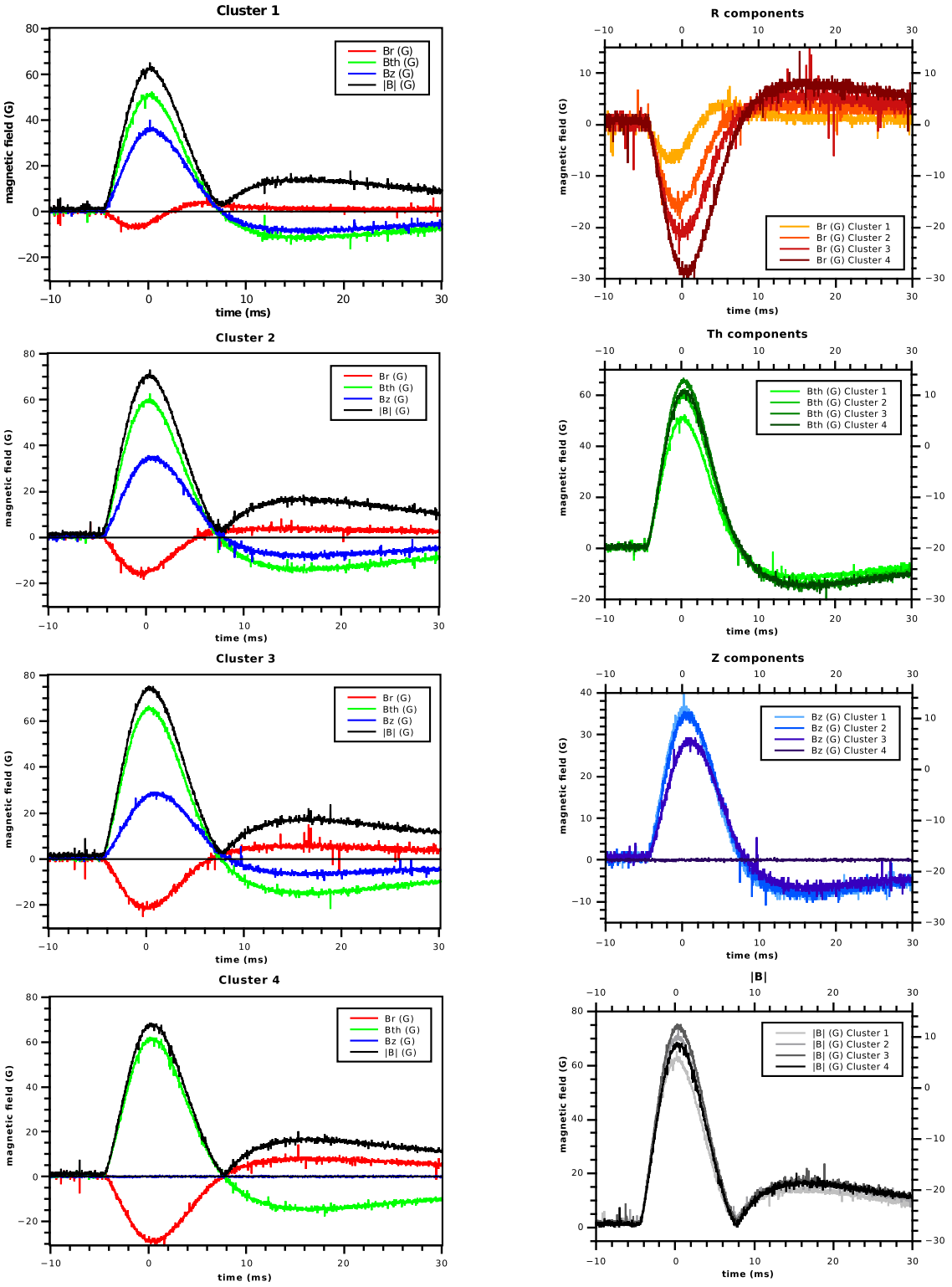

Figure A.6: Vacuum field measured with the magnetic probe array, which was angled such that the arm intersected the horizontal midplane of the electrode directly at cluster 4

of course, easily fixed for plasma shots by adding appropriate negative signs to the IDL routine that display the probe data. It must be kept in mind, however, when data is being taken directly from the probe array itself.

Note that the signals measured with the magnetic probe array peak earlier than the measurements described in the previous section (after $\sim$ 4.8 ms, rather than 5.6 ms), and also exhibit a dip to negative values at later times. It is most likely that these are measurement effects due to the unsophisticated electronics (rather than ringing in the current through the vacuum field coils themselves).

A.3 Calculation of the magnetic field due to a pair of solenoids

Lastly, in order to calculate how much of an effect the iron cores have on the falloff of the magnetic field into the vacuum chamber, the IDL program that calculates magnetic field lines was queried for measurements of what the field would be for two coils without iron cores. Results, shown in Figure A.7, suggest that the magnetic field at 10 cm from the electrodes would be about half the size it is, if not for the coils' iron cores.

A.4 Summary

In general, there is agreement that the vacuum field peaks at $\sim$ 0.3 T at the footpoint of an energized coil (fired from 200 V). The rise time is measured to be $\sim$ 5.6 ms when a single coil is connected to the power supply and $\sim$ 4.8 ms when two coils are connected, perhaps due to interactions between the coils resulting in a decrease in the inductance. In the latter case, the magnetic field produced by each is about 20 percent smaller than in the former.

The field rises significantly faster in front of the nozzles than it does in front of other areas, where it has to diffuse through the copper electrodes. The 3D field evolution must be interesting. Over the course of the microsecond plasma, though, it is effectively stationary.

The magnetic probe array can be used with an amplifier to measure the 3D vacuum field out in the chamber; its only limitation is that it can only do this for $z > 9.5$ cm.

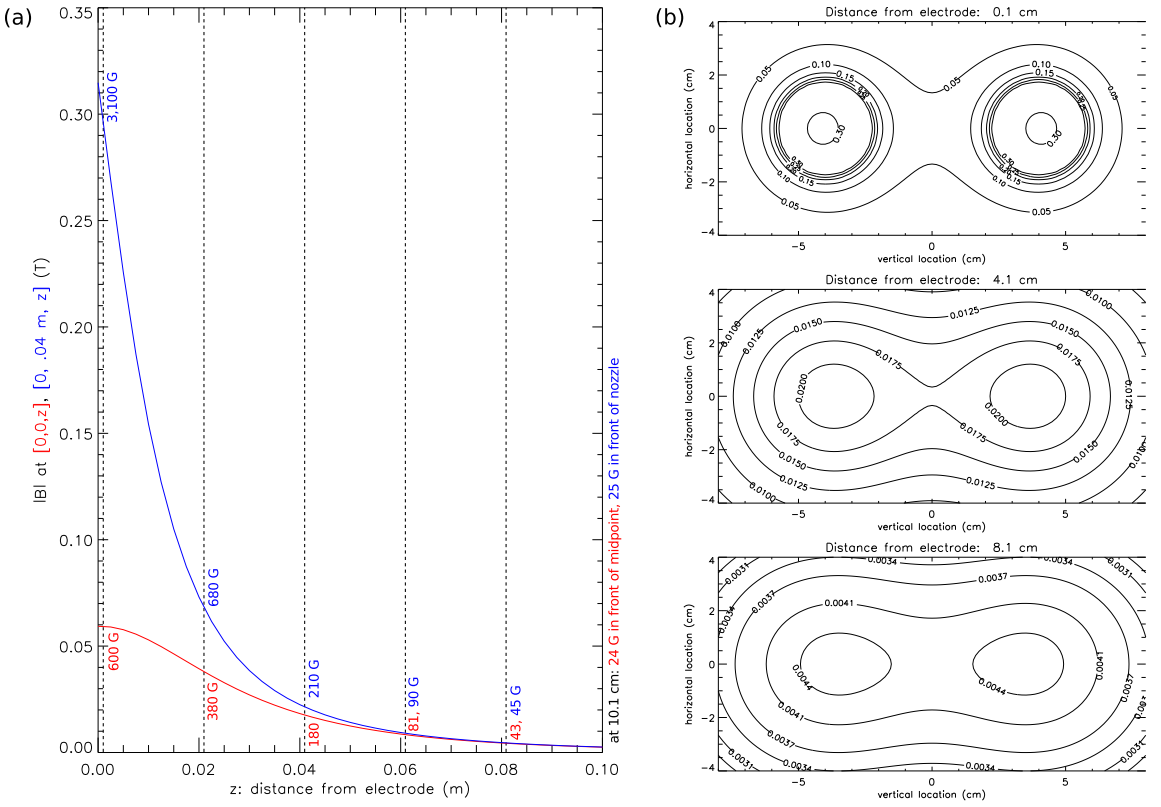

Figure A.7: Magnetic fields calculated for a pair of iron-less solenoids. a.) The magnitude of the magnetic field as a function of distance from the electrodes, for two xy locations: $[0, 0, z]$ (i.e., halfway between the footpoints, where $B = B_x$), shown in red; and $[0, 4\text{ cm}, z]$ (i.e., in front of one of the nozzles), shown in blue. Values in gauss are given at 2 cm increments (dashed lines), starting 1 mm from the electrode surface. b.) Contour plots of the total magnetic field at increased distances from the electrode surface

Appendix B

Details of fast gas valve operations

The details of fast gas valve operation and response are of significant import to the experiments conducted with magnetized plasmas guns. Indeed, it is only by the virtue of fast pulse gas valves that such guns are effective at all. This is because transient concentrated densities are necessary for satisfying the Paschen criterion for breakdown without surrounding the resulting plasma with a suffocatingly large source of neutrals [10].

Due to their essential role, fast gas valves are sometimes a source of "bugs" in experiment operation. For example, variations in the current through a valve (due to heating of the capacitors in the gas valve power supply) were identified as a source of irreproducibility over a series of shots [57]. Other times, these details can be "features" to be exploited. By increasing the gas valve back pressure, Kumar decreased the speed of plasma jets [48]. By decreasing the gas valve charging voltage, Tripathi decreased the total mass of plasma loops, leading to kinetic jets [5].

Whether a pulsed gas valve is a source of bugs or features depends largely on to what extent its quirks are known in advance to its user. Despite their ubiquity in magnetized plasma gun experiments, these valves can still offer surprises to the unexpecting scientist. This appendix is an effort to reduce bugs and increase features.

B.1 Species-dependent variation in total gas released

It may seem obvious in hindsight that gas output is likely to vary by species, but this is often overlooked in discussions of pulsed gas valve behavior. Particle output tends to be described as though it were a fundamental characteristic of the valve design [58, 59], even when a valve has been used with multiple species [59]. Although models of pulsed gas valves may exist that possess this uniform response, the distinction tends to go unmentioned.

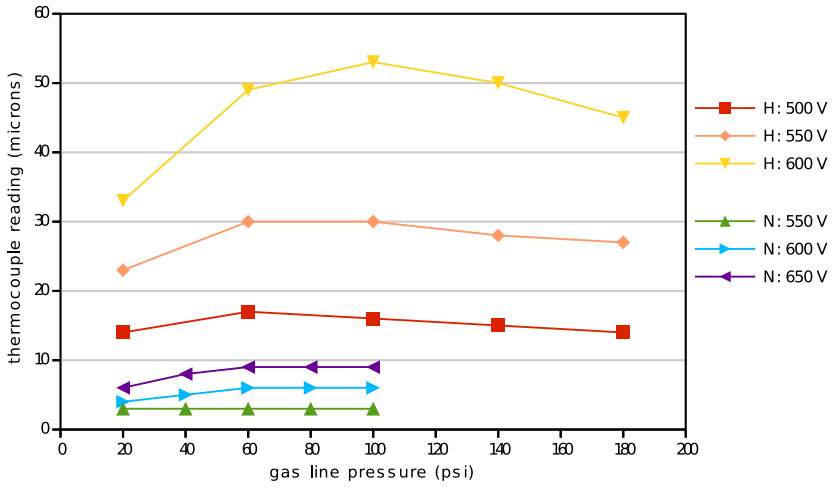

Figure B.1: Pressures reported by the thermocouple gauge in the main chamber (with the gate valve closed) after 10 pulses of one of the fast gas valves show significant dependence on gas species and on power supply charging voltage but relatively little dependence on back pressure.

Even among researchers with considerable experience with the specific model of gas valve currently used at Caltech, different outputs for different gas species have long gone unnoticed — or, at least, unremarked upon. Yun wrote, "The total throughput of the fast gas valve depends on the back pressure and the coil current" with no mention of species dependence [30]. Kumar said little about the gas valves at all, despite making jets of different plasma species [31]. You, too, experimented with plasmas of various species and, in addition, took spatio-temporal measurements of the neutral density prior breakdown [49] — but only as represented by a single test gas.

Within the last couple years, however, notice has been taken. The experiments described in Chapter 3 provide measurements of number density that indicate up to an order of magnitude difference among plasma species. Moser has redone You's fast ion gauge measurements, separately investigating nitrogen and argon [60]. Perkins, in his extensive work on pairs of hydrogen loops, described neutral gas density as being "a major factor in the plasma evolution" and includes measurements of gas valve output as a function of charging voltage for hydrogen, nitrogen, and argon at 100 psi, 60 psi, and 60 psi, respectively[1] [32].

Figure B.1 examines the parameter space in a bit more detail for hydrogen and nitrogen. For a range of back pressures and gas valve power supply charging voltages, the gate valve was closed and a single fast gas valve was triggered 10 times in succession. The resulting rise in the chamber

[1]These are the "go to" back pressures used with the solar quad gun, but may in fact be a hold-over from before the gas valve system was updated.

	thermocouple ratio	molecule ratio	atom ratio
hydrogen	24-30	13-17	26-32
nitrogen	3	2	4
neon	2	2	2
argon	1	1	1

Table B.1: Rough estimates of valve outputs for different species, relative to argon

pressure[2] was read from a thermocouple gauge[3]. This was done for hydrogen, nitrogen, and argon. Argon only caused the thermocouple to read 1–2 mT — if it even increased from zero at all — and therefore was omitted from the plot in Figure B.1. Clearly, there is significant variation from species to species.

From surveying the values in Figure B.1, then incorporating data for argon and neon, a list has been made in the first column of Table B.1 that indicates approximately how much each of four gas species causes the thermocouple pressure to rise for a given back pressure, charging voltage, and number of times the gas valve is pulsed. Values are expressed as a multiplicative factor relative to the increase produced by argon. (E.g., the same settings that would produce a 1 mT rise with argon produce a 2 mT rise with neon.)

The second column estimates a corresponding particle ratio, assuming that the thermocouple — which is calibrated for nitrogen — reads $\sim$ 20 percent high for hydrogen and $\sim$ 30 percent low for argon and neon[4]. The third column gives the atom ratio (i.e., doubling the molecule ratio for diatomic gases). These values actually overshoot the relative differences in number density calculated from the loop evolution speeds in Chapter 3 (see Table 3.1). It is not surprising, though, that the total neutral gas released by the valve over its entire millisecond pulse does not correspond exactly to the number density in the plasma loop.

One can also compare the results in Tables B.1 and 3.1 to the simplest possible model for the gas valve operation: a "gate" that opens for a fixed length of time to let particles out of a reservoir. Figure B.2 illustrates the scenario. Assume that the gas is ideal (so the particles do not collide with one another), and that the gate (the side of the reservoir colored red) opens instantaneously, remains open for time t_g, and then closes instantaneously. A particle will escape the reservoir if it was moving fast enough toward the gate when it opened to get there before it closes — in other words,

[2]The background pressure rise that occurred when the gate valve was closed but no gas valves were triggered was a comparably inconsequential $\sim 6 \times 10^{-6}$ T.

[3]Varian type 0531

[4]These estimates were taken from a "true pressure versus indicated pressure" plot for a thermocouple gauge, though not specifically the Varian 0531 (for which such data were not available).

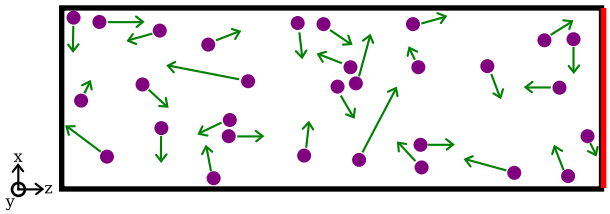

Figure B.2: Cartoon of particles in a gated reservoir

if $v_z \geq d_z/t_g$ where v_z is the z component of its velocity and d_z is its initial displacement from the gate. About half of the particles that are right next to the gate will meet this criterion (the other half are going in the wrong direction), while only a much smaller fraction of particles that are far away will be going fast enough make it out.

Assume further that the wall of the reservoir opposite the gate is infinitely far away, and that the particles have an isotropic Maxwellian velocity distribution so that the distribution function for v_z is given by $f(v_z) = (m/2\pi kT)^{1/2} e^{-mv_z^2/(2kT)}$ where T is the temperature of the system, m is the mass of a particle, and k is Boltzmann's constant. The number of escapees is then given by

$$N_{out} = nA \left(\frac{m}{2\pi kT}\right)^{1/2} \int_{z=-\infty}^{z=0} \int_{v_z=|z|/t_g}^{v_z=\infty} e^{-mv_z^2/(2kT)} \, \mathrm{d}v_z \, \mathrm{d}z \tag{B.1}$$

where n is the number density of the particles, A is the cross-sectional area of the reservoir, and the location of the gate has been chosen as $z = 0$. A few variable substitutions later[5], this simplifies to

$$N_{out} = nA\, t_g \left(\frac{2kT}{\pi m}\right)^{1/2} \int_{w=0}^{w=\infty} \int_{u=w}^{u=\infty} e^{-u^2} \, \mathrm{d}u \, \mathrm{d}w = nA\, t_g \left(\frac{kT}{2\pi m}\right)^{1/2}. \tag{B.2}$$

Thus, for the same gas valve (A, t_g) and back pressure (n, T), the number of particles released should scale as the inverse square root of the molecular mass. The numbers are tabulated in Table B.2, and are closer to the ratios of calculated loop densities from Table 3.1 than the thermocouple's total output measurements were.

	mass (amu)	molecule ratio	atom ratio	experiment n ratio
hydrogen	2	4.5	9.0	10
nitrogen	28	1.2	2.4	1.4
argon	40	1	1	1

Table B.2: Predictions for gas valve outputs from the simplified Maxwell-Boltzmann model (columns 2–3), plus experimentally calculated densities for comparison. Ratios are relative to argon.

[5] Specifically, let $u = v_z/v_T$ and $w = z/(v_T t_g)$ where $v_T = \sqrt{2kT/m}$.

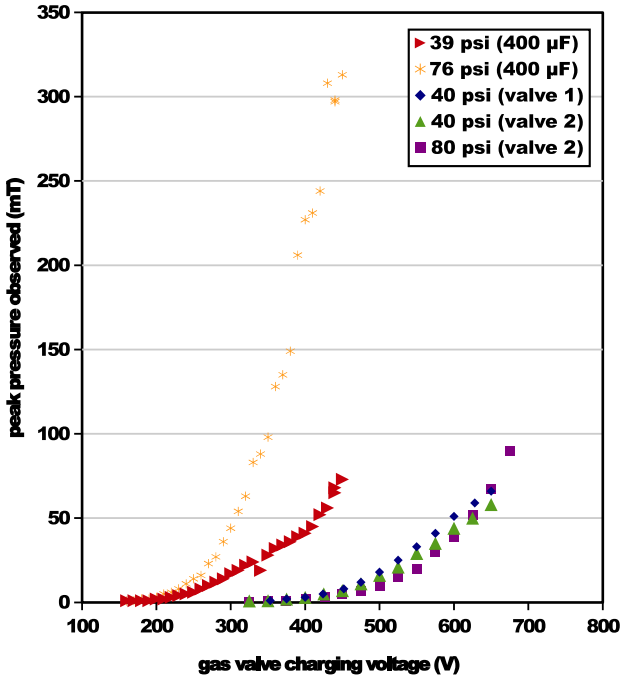

Figure B.3: Fast gas valve output into a test chamber, as measured by the pressure registered on a thermocouple gauge

B.2 Operating regimes

The back pressure dependence in Figure B.1 — or, more precisely, the minimal presence thereof — was surprising because the same model of gas valve has previously been documented as having increased output at higher back pressures. This was seen in Kumar's work [48] and in calibrations on a test chamber. Both of these, however, used different power supplies. It has been noted before that the amount of gas released by a valve is extremely sensitive to the amount of current with which it is pulsed [57]. It seems, in fact, that the amount of current can cause the same valve to operate in significantly different regimes.

Figure B.3 shows fast gas valve output into a test chamber as a function of charging voltage for several setups. The first two tests, with back pressures of 39 and 76 psi, were done with a power supply using two 200 μF metallized polypropylene film capacitors connected in parallel for a total of 400 μF (one of the same banks used by Bellan [57]). The charging voltage was varied from 10 to 450 volts; a sample current pulse is shown in Figure B.4. The gas valve produced an audible "click" starting at 50 V, caused the ion gauge in the test chamber to register an increase in pressure starting at 110 V, and caused the thermocouple gauge to register an increase in pressure starting at 160 V. As can be seen from the plot, having about twice as much back pressure resulted in about 2.5 to 5

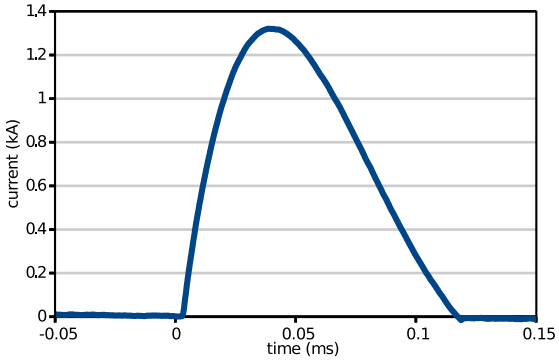

Figure B.4: Current delivered to the fast gas valve from a 100 V charge of the 400 μF capacitor bank, as measured by the power supply's built-in Rogowski coil (calibration factor: $1.678 \times 10^3 = \int V_{R.C.}(t)\mathrm{d}t/I(t)$)

times as much output, depending on the charging voltage.

The next three tests were done with the solar side dual-valve power supply that was installed on the chamber in 2006. This supply uses one 50 μF capacitor per gas valve and produces a 280 A output current for a 100 V charging voltage (as compared to $\sim$ 1.3 kA for the 400 μF bank). Two different back pressures and two different gas valves were tried, all producing about the same output. All five tests used helium gas and the same model of gas valve.

Thomas et al. also found that their throughput was roughly independent of the back pressure for a very similar fast gas valve setup [58]. This, they wrote, "strongly indicates the dynamic pressure differential as the primary supplier of restorative force to the valve piston". For the current generation of Caltech gas valves, this suggests that a sufficiently explosive current pulse may compress the spring[6] enough for it to provide a significant portion of the restoring force on the diaphragm. This would mean that the time the valve is open does not necessarily decrease for higher back pressures, thereby letting more gas through when the back pressure is higher.

B.3 Fast ion gauge measurements of rise time and pressure response

A simple fast ion gauge (FIG) was installed on a test chamber and used to examine time-resolved properties of the fast gas valves. The gauge was constructed using a four-prong feed-through. Two of the prongs were connected via a tungsten wire filament that served as the electron emitter. The other two prongs served as the collector and anode. Schematics for two slightly different versions

[6]There may also be variations from gas valve to gas valve, as there is some uncertainty as to whether all valves of the current model were constructed with the same type of spring.

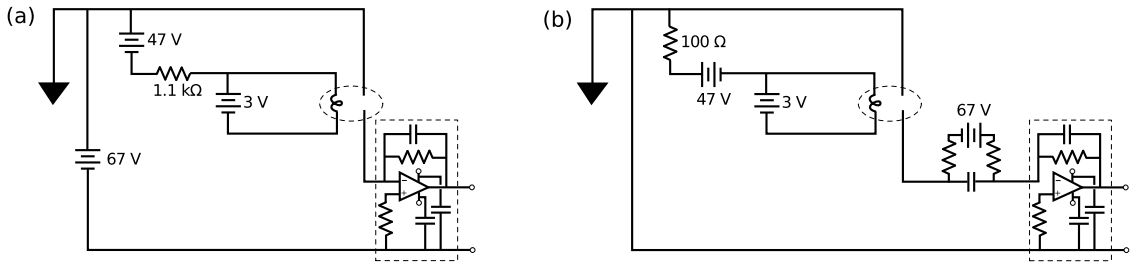

Figure B.5: Two versions of the electrical circuit for the fast ion gauge. The dashed oval encompasses the elements on the vacuum feed-through: the emitter (the negatively biased filament), anode (connected to ground), and collector (even more negatively biased than the emitter). The dashed rectangle surrounds the amplifier for the collector current (output voltage: 48 mV/μA). All capacitors are purely for filtering. In circuit (a), the 67 V negative bias was provided by a power supply, while in (b) it was provided by a battery. Current through the filament was typically $\sim$ 2.5 A, corresponding to an emission current $I_e \sim 5$ mA at vacuum ($\sim 10^{-7}$ T), as measured through the resistor between the filament circuit and ground.

of the accompanying circuit are shown in Figure B.5.

The operating principles for the FIG is as follows:

- Heating current through the filament generates the thermal emission of electrons.
- These electrons are accelerated toward the anode, since it is positively biased relative to the emitter.
- When neutral gas is present, the electrons collide with the gas molecules, creating ions and secondary electrons.
- The ions are attracted to the collector, since it is negatively biased relative to the emitter. The ions "collect" electrons with which they recombine, thereby generating a collector current I_c.
- The ratio of the collector current to the emission current is proportional to the number density of the gas.

The proportionality between density and I_c/I_e must be found by calibrating the FIG against a known pressure measurement for each gas species with which it is to be used.

First, the FIG was tested by measuring the pressure in the test chamber when the gas valve was pulsed at relatively low voltages. The results are shown in Figure B.6 and, being between 0 and 1 mT, match up well quantitatively with the thermocouple-based results (as shown in Figure B.1). Essentially, Figure B.6 is a time-resolved picture of how the gas quickly fills the chamber prior to being pumped out again.

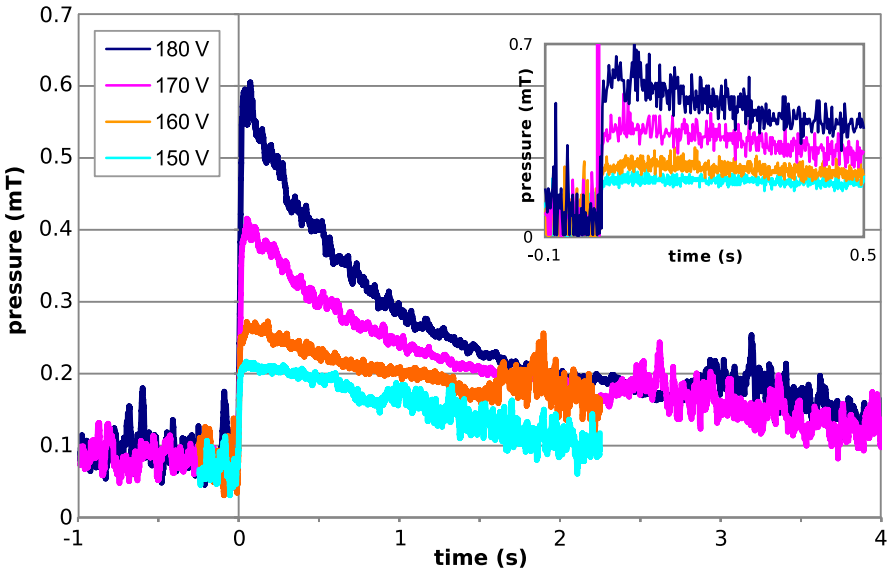

Figure B.6: Smoothed time-resolved measurement of the test chamber pressure due to a pulse of helium (back pressure: 70 psi) from the fast gas valve, for charging voltages of 150, 160, 170, and 180 V. The modest size of the pressure jumps reflect that the FIG was located relatively far from the gas valve in the test chamber. Smoothing was done with a boxcar average ($\pm$ 5 points) that obscures somewhat the quick rise time; the inset shows the unsmoothed measurement over the first half second. True pressures may be $\sim$ 15 percent higher because the FIG was calibrated against a standard ion gauge that in turn was calibrated for nitrogen.

Next, the FIG was positioned on a test chamber port directly opposite a moveable copper tube connected to the gas valve. A diagram of the setup is shown in Figure B.7. When the tube was fully inserted into the chamber ($d = 0$ in the diagram), its end was within centimeters of the FIG (though the gas still had to travel through $\sim$ 47 cm of gas line and copper tube to reach that end). The insertion of the tube was then decreased in steps, and the FIG was used to measure the resulting differences in time-resolved gas density.

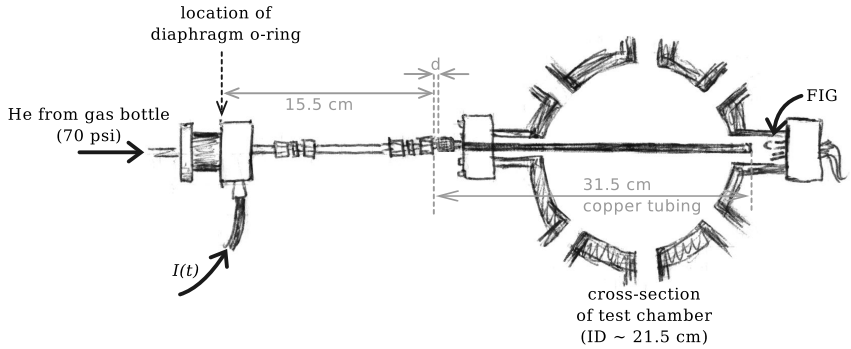

Figure B.7: Varying the distance from the gas outlet to the FIG

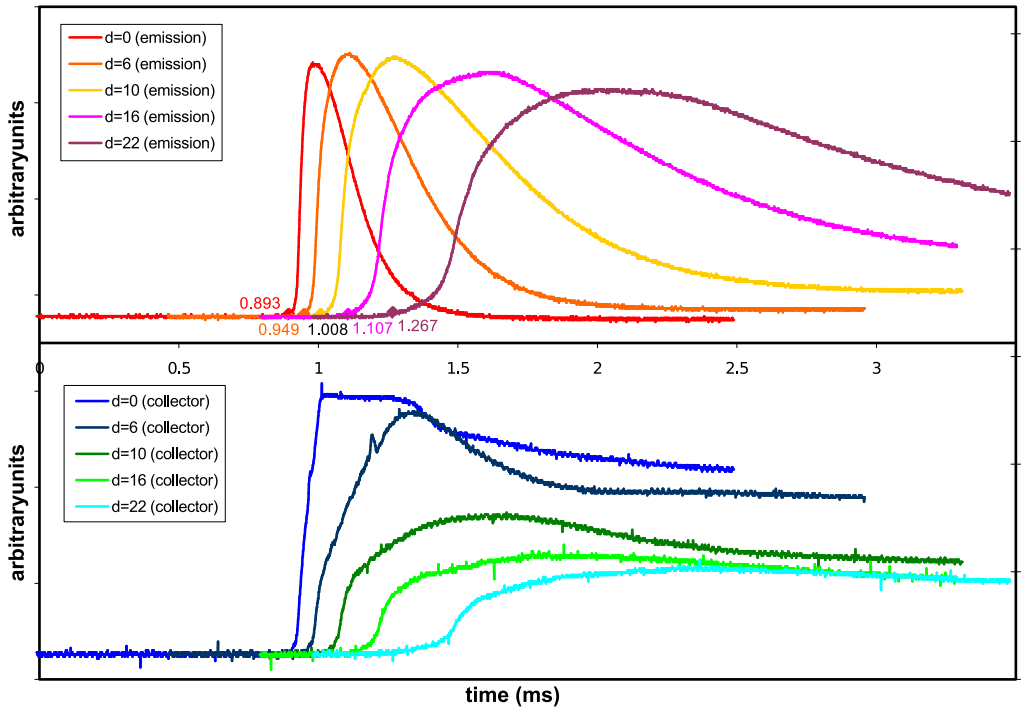

Figure B.8: I_e and I_c at increasing distances from the outlet. The gas valve was operated with helium gas (70 psi back pressure) and a charging voltage of 150 V.

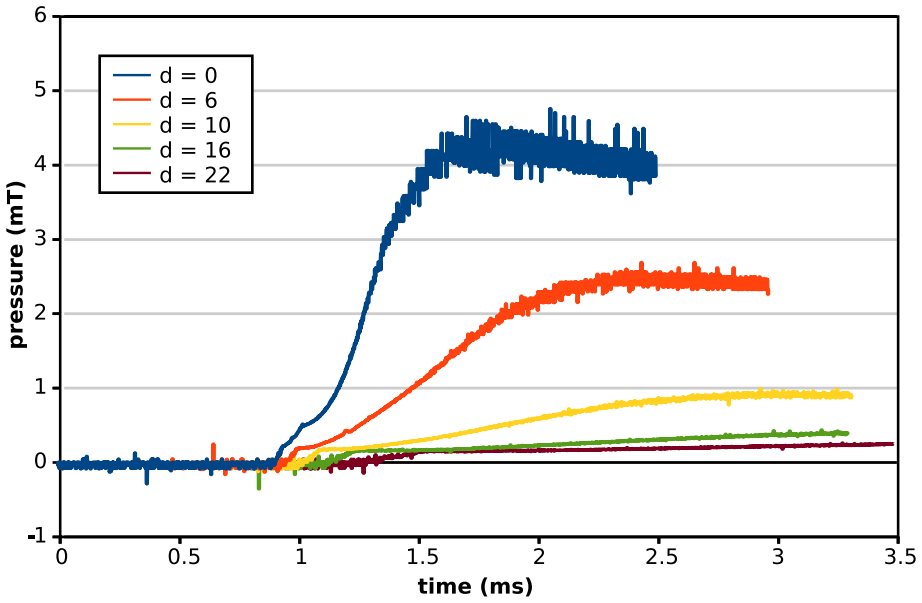

Figure B.9: Pressure at increasing distances from the outlet, as calculated from ratio between the collector and emission currents shown in Figure B.8. (As in Figure B.6, true pressures may be ~ 15 percent higher because the FIG was calibrated against a standard ion gauge that in turn was calibrated for nitrogen.)

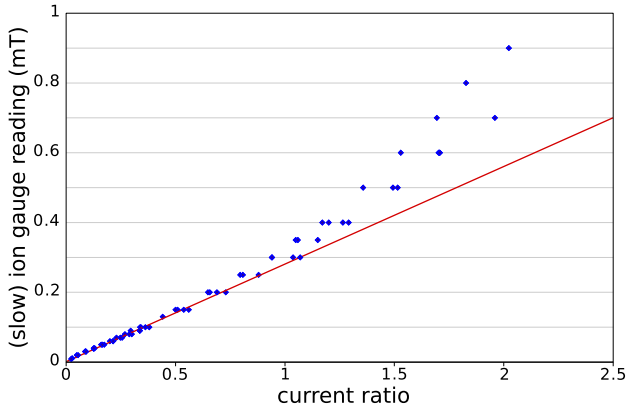

Figure B.10: Pressure (according to the test chamber's standard ion gauge) versus I_c/I_e, recorded while pumping down the chamber. The red line shows the linear fit. The divergence of points at higher pressures is attributed to lag on the part of the ion gauge.

Figure B.8 shows the resulting emission and collector currents for five different values of d, and Figure B.9 shows the corresponding pressures calculated from I_c/I_e, using the calibration shown in Figure B.10. Since 1 mT $\sim 3 \times 10^{19}$ m^{-3}, they are are in good agreement with Yun's order of magnitude estimate for flow rate [30], as well as Moser's calculations using a different FIG on the main chamber [60].

B.4 Summary and suggestions

The amount of gas released by a fast gas valve has been found to depend on a combination of the current form with which it is pulsed and both the species and pressure of the gas supplied to it. The nature of this dependence can be nonlinear and/or unexpected. As a result, inferences based on similar (but not identical) conditions are suspect.

Furthermore, the mass density of the plasma loop does not necessarily scale with the total amount of gas released. One possible explanation for this is that the diaphragm can bounce after it closes, perhaps letting in a secondary pulse of gas considerably after the first. Regardless, using the total gas output as a proxy can be misleading.

In cases where the neutral density at the time of breakdown is significant to the experiment design or analysis, it is highly recommended that a full set of measurements be taken with a FIG. When calibrating the FIG, attention should be paid to how the instrument used for calibration (be it a thermocouple or a traditional ion gauge) measures differently for different gas species.

Appendix C

Estimate for $\mathrm{d}\Phi/\mathrm{d}t$ and other circuit parameters

Because plasmas are highly conductive, it is often tempting to simplify mathematical expressions by assuming that the magnetic flux Φ is perfectly conserved. However, as discussed in Section 3.1, this is not precisely true for the Caltech experiments. This appendix addresses the question of how imprecise that approximation is, and what that implies about other electrical parameters of an individual plasma loop.

The electromotive force due to the change in flux $\mathrm{d}\Phi/\mathrm{d}t$ can be calculated analytically using representative functions for the current $I(t)$ conducted by the plasma loop and for the loop's major radius $r(t)$. Then, by using a combination of Faraday's law (Equation 3.2) and the expression for the inductance of a circular hoop (Equation 3.4), one can easily calculate the induced emf. For comparison, Figure C.1 shows the typical range of measured current and voltage.

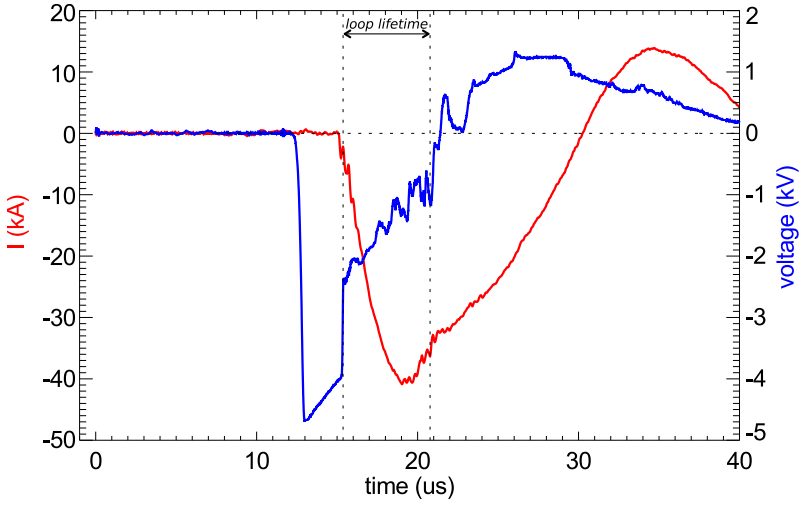

Figure C.1: Sample current and voltage traces, taken from an argon plasma loop *(shot 9067)*

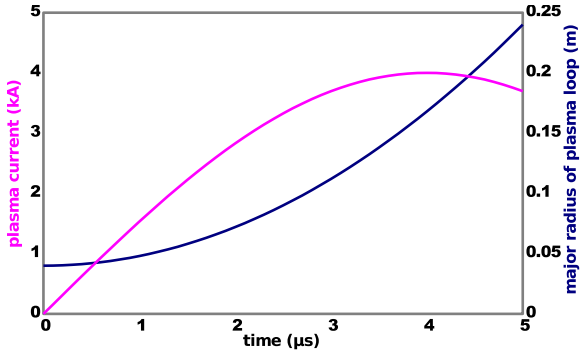

Figure C.2: Representative functions for the radius of the plasma loop (approximated as a circular hoop) and the electrical current the plasma loop conducts

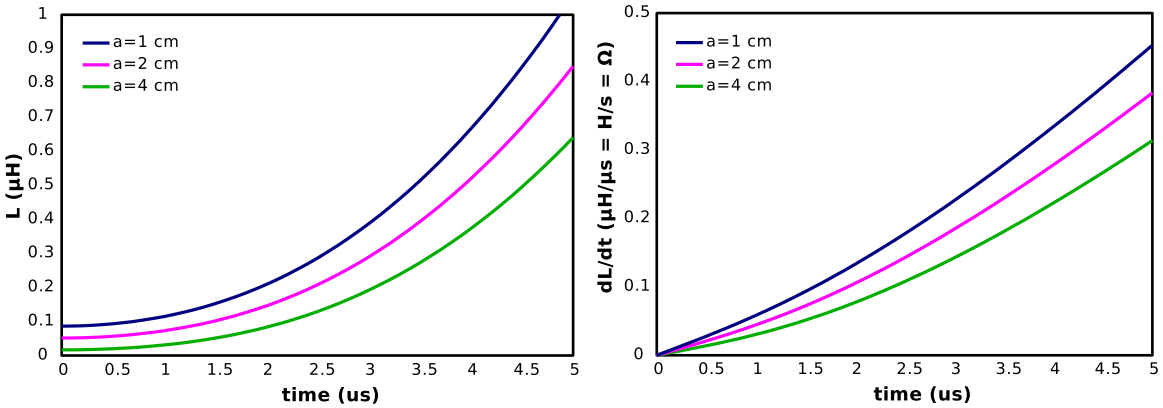

Figure C.3: Inductance L and its time derivative dL/dt as functions of time, for a circular hoop with the current and major radius shown in Figure C.2, a uniform current distribution, and a minor radius of $a = 1$ (blue), 2 (magenta), or 4 (green) cm

Assume a circular loop with an initial radius of 4 cm, increasing quadratically in time. Assume also a sinusoidal capacitor output current with amplitude 40 kA and period 8 microseconds, of which the fraction $f = 0.1$ flows through the loop. Figure C.2 shows the loop radius and loop current plotted versus time.

Recall that the expressions for inductance of a circular hoop and its derivative with respect to radius (Equations 3.4 and 3.6) are[1]:

$$L = \mu_0 r \left(\ln\left(\frac{8r}{a}\right) - 2 + Y \right)$$

$$\frac{\partial L}{\partial r} = \mu_0 \left(\ln\left(\frac{r}{a}\right) + 1.08 + Y \right)$$

[1]This appendix uses r instead of R for the radius to avoid confusion with the plasma resistance R.

Using a uniform current distribution ($Y = 1/4$), $L(t)$ has been calculated from the specified $r(t)$ for three different sizes of minor radius a. Results are shown in the left-hand plot in Figure C.3, and the rate of change in inductance $dL/dt = (dL/dR)(dR/dt)$ is shown in the right-hand plot. (Note that the time dependences of $L(t)$ and $\dot{L}(t)$ are highly reflective of $r(t)$ and $\dot{r}(t)$, respectively, because the logarithmic terms are slowly varying.)

The plasma loop's inductance is on the order of of tenths of microhenries. The corresponding induced electromotive force (shown versus time in Figure C.4) is on the order of a kilovolt, as calculated from Equation 3.8:

$$\frac{\mathrm{d}\Phi}{\mathrm{d}t} = L\frac{\mathrm{d}I}{\mathrm{d}t} + I\frac{\mathrm{d}L}{\mathrm{d}t}.$$

This is also the order of magnitude of the voltages measured across the electrodes of the plasma gun (as seen, for example, in Figure C.1).

Some further examinations of the plasma's electrical parameters can be made, in the model of the circuit analysis of the Caltech coaxial plasma experiment performed by Kumar [31]. The voltage across the electrodes is related to the change in magnetic flux (calculated above) by the equation

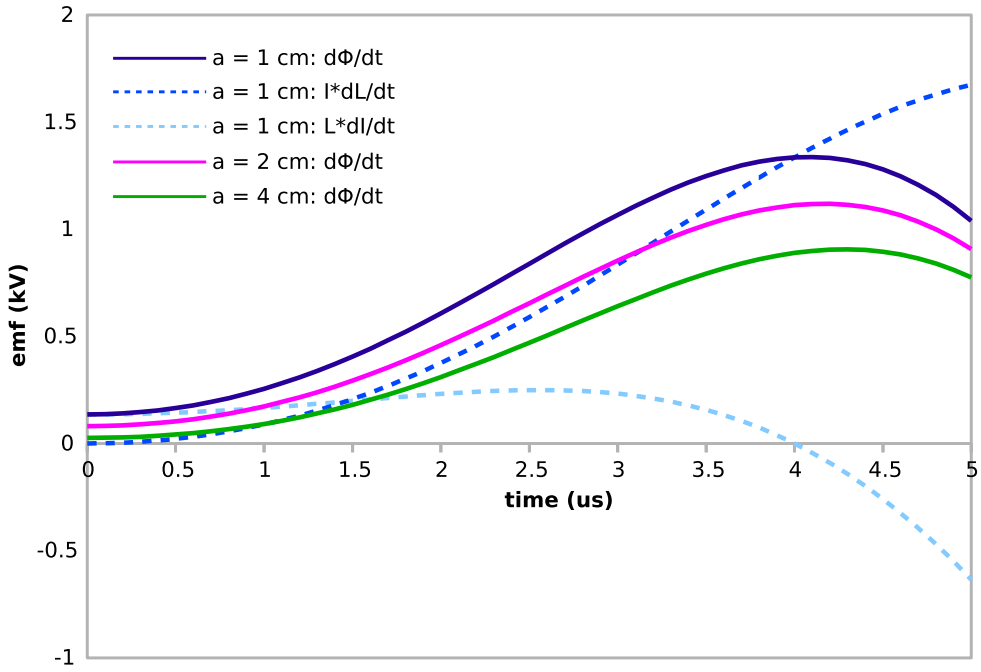

Figure C.4: Instantaneous change in flux $d\Phi/dt$ as a function of time for a hoop with the current and major radius shown in Figure C.2, and a minor radius of $a = 1$ (blue), 2 (magenta), or 4 (green) cm. For $a = 1$ cm, the two terms in $d\Phi/dt$ are shown with dashed lines.

$$\begin{aligned} V(t) &= I(t)R(t) + \frac{\mathrm{d}\Phi}{\mathrm{d}t} \\ &= I(t)\left(R(t) + \dot{L}(t)\right) + L(t)\dot{I}(t) \end{aligned} \tag{C.1}$$

where $R(t)$ is the resistance of the plasma loop.[2] When $\dot{I}(t) = 0$, the equation becomes $R + \dot{L} \sim V/I$. The ratio between voltage and plasma current at the time of the current peak ranges from about 0.25 to 0.75 Ω. Since $\dot{L}$ is in the 0.2–0.3 Ω range (see Figure C.3), this suggests that the plasma loop resistivity is also in the tenths of ohms.

This agrees with another estimate calculated using the Spitzer resistivity η, which Kumar estimated to be $\sim 3.6 \times 10^{-4}$ Ωm. The resistance of the plasma would then be given by

$$\begin{aligned} R &= \frac{\eta l}{\pi a^2} \\ &\sim 0.1 - 0.7\ \Omega \end{aligned} \tag{C.2}$$

for a plasma with minor radius $a = 1$ cm and length ranging from l =10–70 cm.

The table below presents a side-by-side comparison of the parameters described above with those Kumar derived for the coaxial gun.

	solar gun	coaxial gun
L	0.1–1.0 μH	30–50 nH
$\mathrm{d}\Phi/\mathrm{d}t$	$\sim$ 1 kV	$\sim$ 1 kV
R	0.1–0.7 Ω	2.5–5 mΩ
$\dot{L}$	0.1–0.7 Ω	6–7 mΩ

Table C.1: Summary of solar gun and coaxial gun [31] electrical parameters

[2]Note that if one instead assumed that all of the current flowed through the loop, $\mathrm{d}\Phi/\mathrm{d}t$ and IR would be an order of magnitude larger than voltage measured across the electrodes. There still remains the question, however, of why the measured voltage across the electrodes remains relatively constant during the plasma lifetime — rather than increasing — when all the terms in Equation C.1 appear to be increasing in magnitude. (Recall that the sloped signal in Figure C.1 is an artifact of an isolation transformer that does not faithfully transit low frequency signals.)

Appendix D

Analyses of uncertainty, variation, and error in loop traces

Each loop trace presented in the body of this dissertation was generated from an individual plasma shot. This appendix establishes the representative nature of such traces. It examines the reproducibility of the tracing method, the shot-to-shot variation, and qualitative differences between traces of left- and right-handed loops. For dual-gas plasmas, variation in loop segments due to the choice of boundary between two gases (which can be influenced by the choice of image processing technique) is quantified. Potential errors due to geometric considerations (viewing angle variation and the systematic error introduced by measuring the length of a kinked structure via a single two-dimensional projection) are also examined.

D.1 Method reproducibility

Because the axis of the plasma loop is identified "manually" (by the user's clicks, rather than some form of automated image-analysis), there is an element of the resulting measurement — indeed, each click — incorporating a judgment call on the part of the user. As such, it is important to establish that these calls are not so variable that the same user tracing the same image on a different day produces a significantly different result. (Automated image analyses, though they are complex to implement and may "miss" features that would be "obvious" to human analysts, do not have this problem.[1])

To address this question, the same set of images was traced five different times, on four different days. The first trace was four months before the second. The second and third traces were on the

[1] The field of sun spot identification provides an illustrative case study in the process of reconciling traditional, manual image analysis with automated methods.

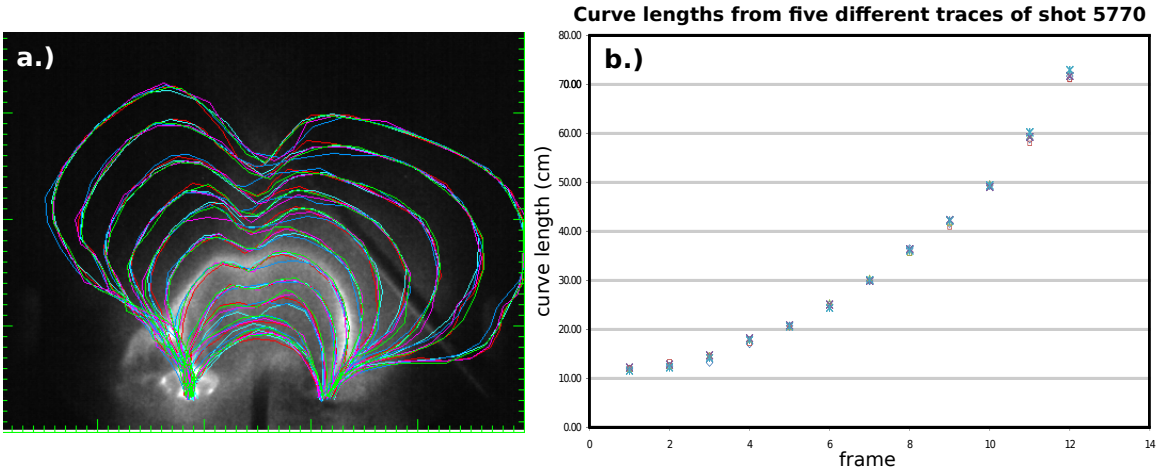

Figure D.1: Five traces of the same hydrogen plasma loop

same day, but used very different presentations of the image data. (The second used the 10-bit version, for which the 8-bit greyscale color table is "cycled through" four times in the course of translating the entire range of pixel values into an image.) The fourth trace was the next day, and the fifth was two days after that. The results are compiled in Figure D.1.

Figure D.1a shows all five sets of loop traces, overlaid on frame 6 of the Imacon series (rescaled to be an 8-bit image). The curve to curve variation is greatest near the kink in later frames, but overall is remarkably low. Figure D.1b shows the variation in the five plots of curve length versus frame number. The standard deviation of the measurement ranged from 0.6 percent (frame 9) to 4.6 percent (frame 3), with an average of 1.8 percent.

Thus, the loop tracing method is quite precise, despite being done manually.[2]

D.2 Shot-to-shot variation

The next question to consider is how much the loop traces vary from one plasma shot to another taken with the same charging voltages. The high reproducibility of the experiment, as evidenced by the effectiveness of combining images from multiple shots, suggests that the shots can generally be treated as interchangeable. Using loop traces, a quantitative measurement can be made.

Analyses were performed for both nitrogen plasmas (which tend to be brighter relative to the background, presumably making identification of the loop axis easier) and hydrogen plasmas (which tend to be dimmer, since only neutrals atoms are visible). Results are shown in Figure D.2.

[2]Since all traces presented in this dissertation were done by the same user, no investigations were made into how the results and/or precision might vary from user to user.

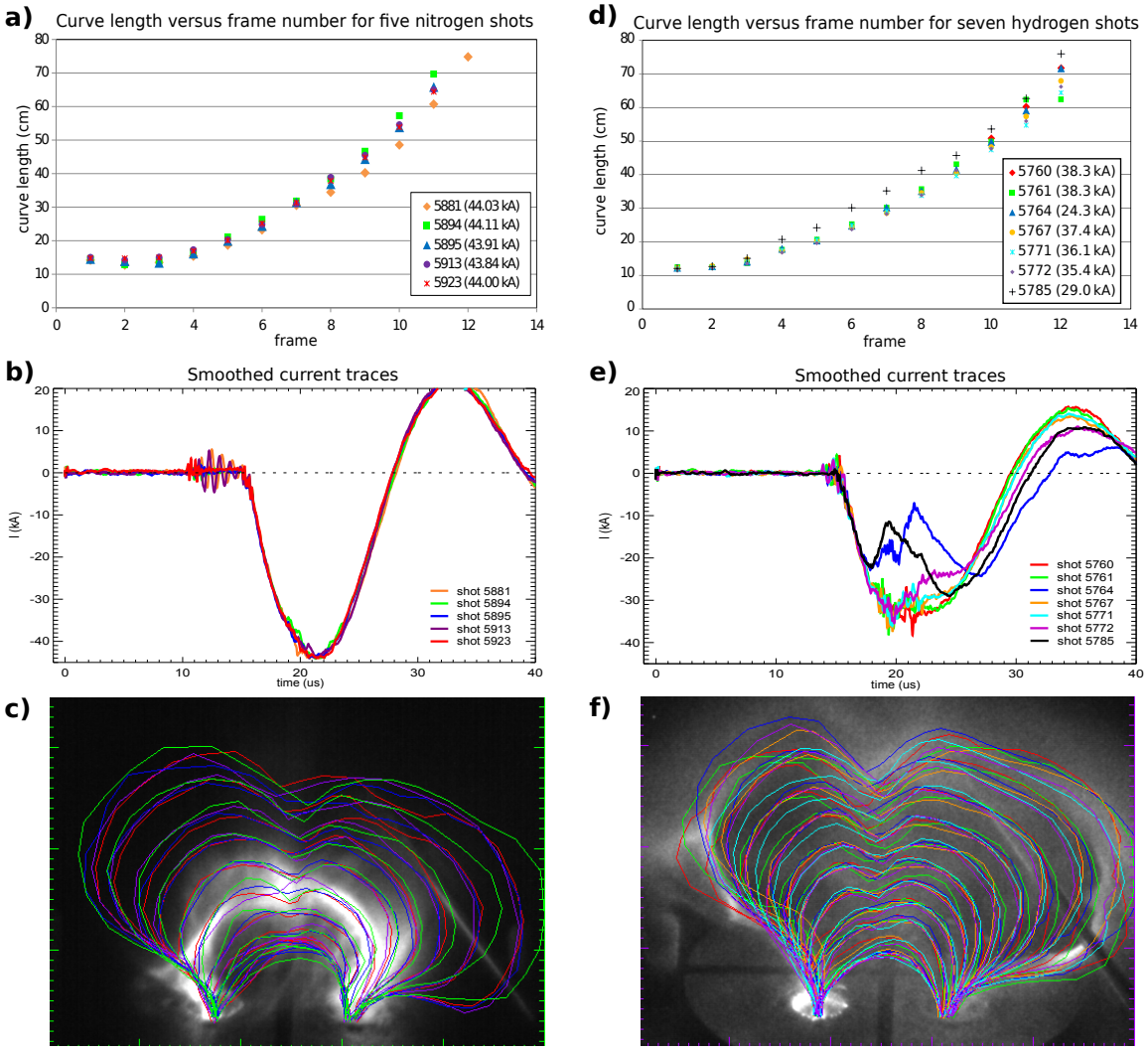

Figure D.2: Shot-to-shot variation in sets of nitrogen (a–c) and hydrogen (d–f) plasma loops. The left-handed loops (5881 and 5795) are omitted from the compilations of curve overlays (c,f), for clarity's sake. The background image in (c) is frame 6 of shot 5923. The background image in (f) is frame 12 of shot 5772. That the current traces for 5764 and 5785 experience severe dips while the plasma loop still expands normally is consistent with the conclusion that only a fraction of the total current is flowing through the loop itself.

Five nitrogen loops that had similar peak values of electrical current were selected for analysis. Among the resulting measurements, there are three sets of curve lengths that fall right on top of one another, one that is noticeably slower, and one that is noticeably faster. Each of the outliers also has a distinct condition relative to the others. The fast loop (shot 5894) was the first shot taken after a reversal of the polarity of the bias magnetic field; it is possible that hysteresis in the iron core of the magnetic field coils might have resulted in a slightly weaker vacuum field (and, thus, flux tube axial field). The slow loop (shot 5881) was left-handed, while the others are all right-handed.

The standard deviation in curve length for the entire set of nitrogen loops ranges from 1.5 percent (frame 7) to 6.4 percent (frame 2), with an average of 4.6 percent. If the two outlier shots are excluded for the reasons described above, the standard deviation ranges from 0.7 percent (frame 7) to 6.4 percent (frame 3), with an average of 2.1 percent.

Seven hydrogen loops were selected for their common diagnostic trigger delay.[3] They exhibit more variation than do the nitrogen shots. Again, though, the one left-handed loop included in the set (shot 5784) is a distinct outlier, this time yielding longer curve length measurements than the set of right-handed loops. Shot 5761 produces the unusual measurement that the curve length barely changes from the 11th to the 12th frame. This is because the plasma loop has clearly detached from the electrode during the interim, as shown in figure D.3); the curve trace, as a result, stops short of making it back to the electrode.

The standard deviation for the entire set of hydrogen loops ranges from 1.6 percent (frame 1) to 8.5 percent (frame 6), with an average of 5.5 percent. If the left-handed loop and the detached frame measurements are excluded, the standard deviation ranges from 1.7 percent (frame 1) to 4.9

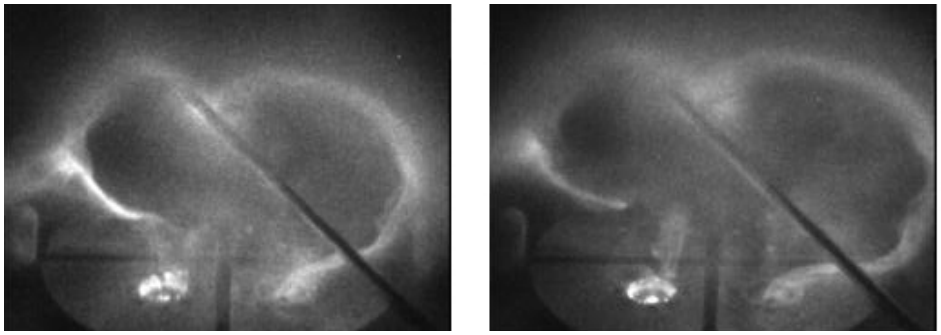

Figure D.3: Frames 11 and 12 of shot 5761 show that the plasma loop coming detached from the cathode

[3]The optical collimator signal used to trigger the diagnostics can occasionally vary slightly; the result is unnoticeable except when superimposing current traces and/or images.

percent (frame 11), with an average of 2.9 percent.

Thus, shot-to-shot variation is also only a few percent of the measured curve length, and some of that variation is due to the measurement itself (as discussed in the previous section). For series of shots in which the helicity of the plasma is unchanged (such as those in Figure 3.10, the variation is even smaller.

D.3 Left-handed versus right-handed loop traces

It was mentioned in the previous section that a right-handed loop and a left-handed loop taken with otherwise identical experiment parameters exhibit larger differences in curve length growth rate than is seen in the shot-to-shot variation of loops with the same helicity. Curiously, the helicity of a loop does not seem to necessarily increase or decrease the measured growth rate. (Recall that the left-handed nitrogen loop is slower than the corresponding right-handed loops in Figure D.2a, while the left-handed hydrogen loop is faster than the corresponding right-handed loops in Figure Figure D.2d.) What is consistent, however, is the qualitative difference in the shape of the loop traces.

The reader may have observed that the sets of loop traces shown in both Figure D.1a and Figures D.2c,f exhibit distinct asymmetry[4], especially at later times (i.e., longer lengths). Compared to the left (cathode) side, the right (anode) sides of the loops appear to bulge out farther horizontally and curve back more toward the electrode near the footpoint.

Figure D.4 shows that this effect is indeed largely attributable to the helicity of the structure. Both the nitrogen and hydrogen right-handed loops (panels a and e) show the lopsidedness described above, while the left-handed loops of both species (panels b and f) exhibit mirrored lopsidedness, bulging out farther to the left and appearing to more closely approach the cathode. Plotting right-handed and left-handed curve traces on the same axis further demonstrates the difference (panel c for hydrogen, g for nitrogen; the right-handed shots are plotted in red, the left-handed shots in blue). It also shows, though, that the mirroring is not exact. To examine this further, once can mirror the left-handed traces across the midline between the footpoints; this improves the qualitative similarity between the sets of traces, especially at the footpoints, but by no means makes the curves coincident (panels d and h).

Much of the lopsidedness of the traces is attributable to viewing angle. This can be seen from

[4]In a testament to the biased nature of human visual perception, this asymmetry is quite obvious when the images are displayed in the rotated orientation (with the apex of the loop pointed toward the top of the page). When the images are viewed in the horizontal orientation with which they are photographed, though, the asymmetry is easy to overlook.

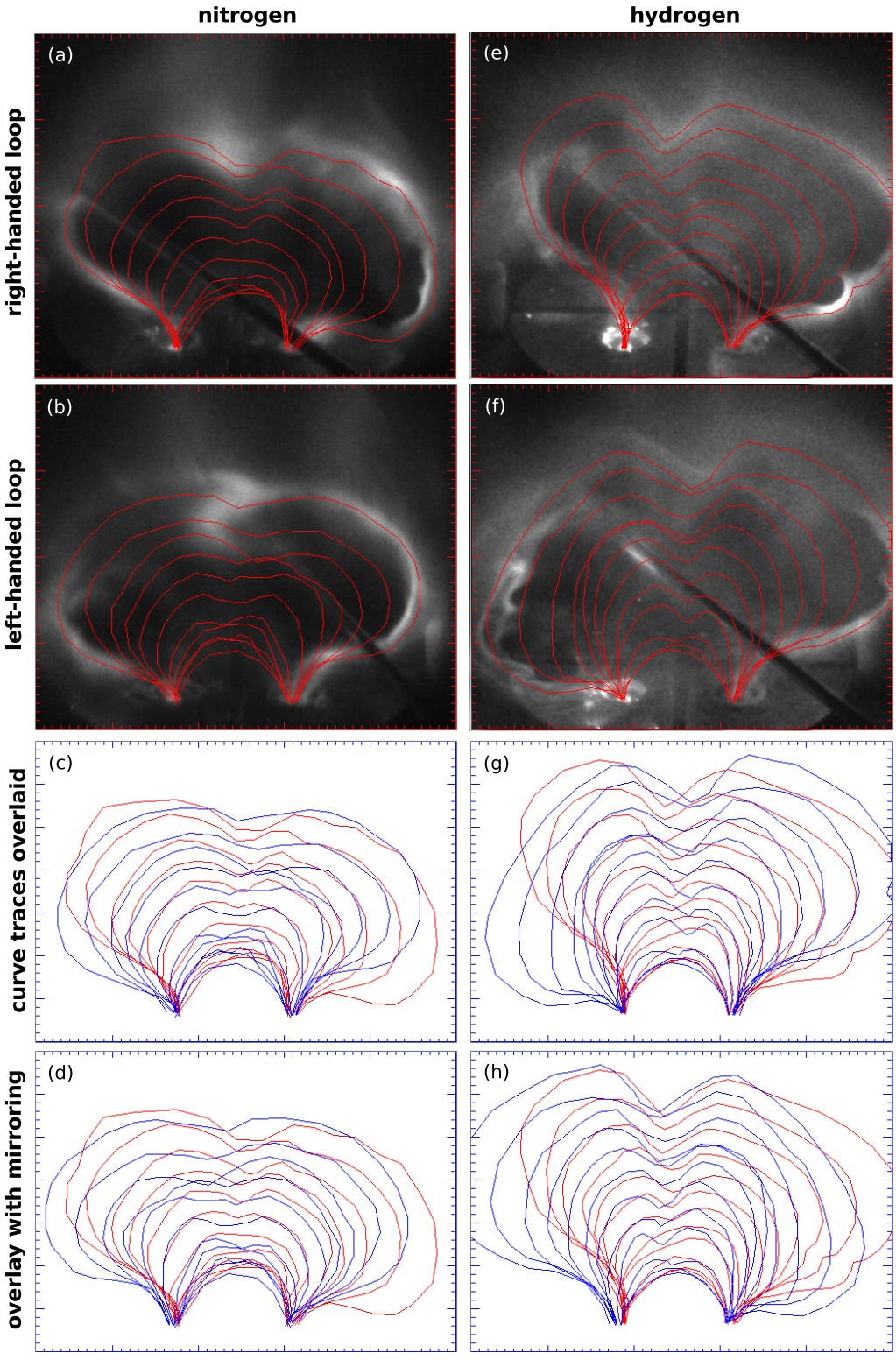

Figure D.4: Helicity-based variation in loop traces. (shots 5895, 55881, 5764, 5785)

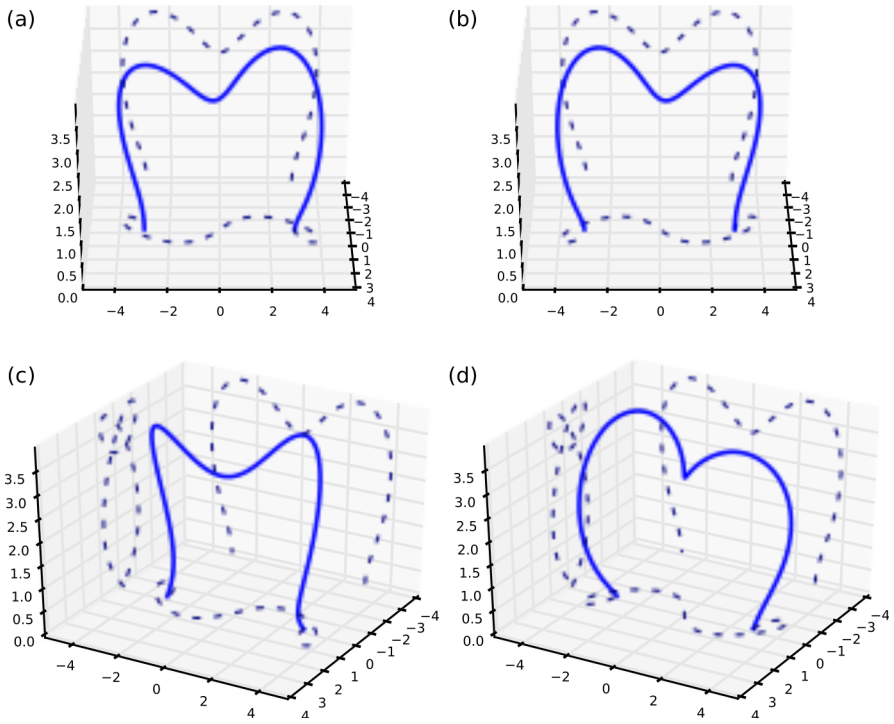

Figure D.5: 3D curves modeling plasma loop axes (solid blue) with projections (dashed blue) onto planes bounding the plotting volume: a.) Right-handed arched helix and b.) left-handed arched helix, both viewed from 30 degrees above the xy plane. c.) Right-handed arched helix, and d.) left-handed arched helix, both viewed from 30 degrees above the xy plane, after a 30 degree rotation about the vertical (z) axis

plots (i.e., 2D projections) of 3D mathematical curves of the form

$$\begin{aligned} x(\theta) &= \pm a \sin(4\theta) \\ y(\theta) &= \cos\theta(R - a\cos(4\theta)) \\ z(\theta) &= \sin\theta(R - a\cos(4\theta)) \end{aligned} \tag{D.1}$$

where $\theta \in [0, 2\pi]$, the sign for $x(\theta)$ is positive for a right-handed helix and negative for a left-handed helix, and R represents the major radius and a the minor radius of a half toroid around which the curve is "wrapped". Figure D.5 shows examples for $R = 4$, $a = 1$.

In Figure D.5a, the right side of the curve appears bulged compared to the left, with the right leg of the curve appearing to "lean over" more toward the bottom plane. In Figure D.5b, the opposite is true. The left half of the curve looks larger than the right, and the left leg appears to be at more of an angle with respect to vertical. (Of course, none of these apparent asymmetries are actually present, as can be seen from the projections onto the $z = 0$ and $x = -4$ planes.) These are the

same trends that were observed in the traces of plasma loops, indicating that these loops, as well, are more symmetrical than they appear.

Figures D.5c and d show the dramatic difference between the appearance of a right-handed helical loop and a left-handed helical loop when the viewer is not in the plane between the two footpoints. Although the Imacon camera might not have been quite in the horizontal plane bisecting the electrode for the plasma loop experiments presented in Section D.4 (as evidenced by the gap between the electrodes not being quite "straight up and down" in the photographs of the hydrogen plasmas), the offset is very minor. As such, it seems insufficient to explain why the right-handed and left-handed traces are not mirror images of one another. Fortunately, the phenomenon appears to be merely a curiosity, as the effects on the quantitative analyses of loop dynamics are quite small.

D.4 Boundary identification in dual-gas loop traces

When tracing the two sections of a dual-gas plasma loop, another source of uncertainty in the loop traces (and the resulting curve lengths of the two segments) is the identification of the boundary between the two species. Color images generated from multiple shots using optical filters (as described in Section 2.3.5) are invaluable for gauging the extent that each jet of plasma extends into the arched flux tube. However, choosing exactly where along the loop to designate as the collision point is not trivial, because different methods of image combination seem to suggest different answers. Furthermore, white light images (in which hydrogen plasma emits significantly less light than nitrogen or argon plasma) can suggest yet a third option.

Figure D.6 presents an analysis of this uncertainty, looking at high, medium, and low estimates for the length of a nitrogen section (which, of course, correspond to low, medium, and high estimates for the hydrogen section of the same loop). Panel (a) shows traces of a set of composite images of three plasma loops, combined via the "averaging" method. The boundary between the two species was chosen to be the end of the higher-emission section of plasma associated with nitrogen, which appears in the averaged image to extend into the more diffuse hydrogen "cloud". The traces in panel (b) come from the same set of images as (a), but here the boundary was chosen based on hue — as opposed to brightness — to be midpoint of the magenta-colored region (where emissions from both species were detected via optical filters). Panel (c) shows traces from a set of composite images of the same three plasma shots, but combined instead via the "subtraction" method. The boundary was chosen to the farthest the blue/magenta region extends. In panel (d), the curve traces from (a-c) are

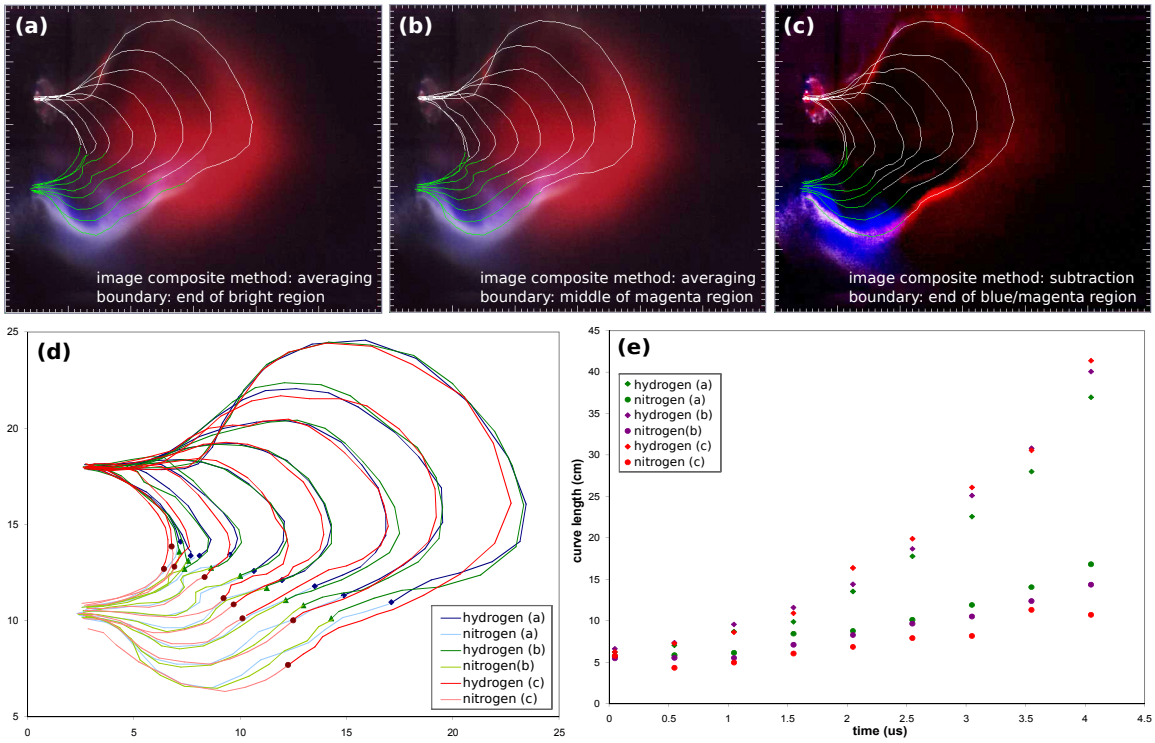

Figure D.6: Measurement uncertainty due to designation of dual-gas boundary. a–c.) Sets of loop traces overlaid on the last frame of their respective image series; nitrogen sections are traced in green, while hydrogen sections are traced in white. d.) The three sets of curves generated from the traces in (a–c), corrected for the camera viewing angle. Points mark the species boundaries. e.) Curve lengths plotted versus time for the curves shown in (c). (shots 5019 [greyscale], 5027 [red-filtered], and 5024 [blue-filtered])

plotted on the same graph. In panel (e), the lengths of the curve traces are plotted versus time. The standard deviation in curve length for hydrogen ranges from 2.3 percent (frame 2) to 9.8 percent (frame 5), with an average of 5.9 percent. For the shorter nitrogen sections, the variation is a larger proportion of the length, with standard deviations ranging from 3.0 percent (frame 1) to 22.0 percent (frame 9), with an average of 13.4 percent.

Hence, the least precise element of the curve length measurements in dual-gas plasmas is the ambiguity regarding at what point along the loop axis the transition occurs from one species to the other. This is reflected in the scatter in Figure 3.8 and suggests that single-species plasmas are somewhat better suited for the precise quantitative analyses of single loops.

D.5 Negligibility of viewing angle uncertainty

As previously described (Section 2.3.5), estimations of plasma length are calculated from image traces using a calibration that includes the camera viewing angle. This viewing angle is calculated from the foreshortening of the electrode in the horizontal direction (measured from the images), and represents yet another source of error in the curve lengths reported. It is a very small one, though, as estimates for the viewing angle only vary by about $\pm$ 1 percent, resulting in a $\pm$ 1 percent variation in the y-coordinate.

D.6 Systematic error of 2D projection

Finally, there is a systematic error that comes from estimating the length of a kinked loop by looking at its projection into a two-dimensional plane. This error can be estimated by considering a straight helix, described by the set of equations

$$\begin{aligned} x(\theta) &= a\cos\theta \\ y(\theta) &= a\sin\theta \\ z(\theta) &= b\theta \end{aligned} \tag{D.2}$$

where a is the radius of the helix and $2\pi b$ is the pitch (the distance between adjacent points on the curve with the same values for x and y). Figure D.7 shows three helices of this type, with values of $a = 1$ and $b = 1$, 2, or 4.

From a viewing angle perpendicular to its axis, the projection of the helix is a sinusoidal curve (as seen on the walls of the bounding boxes in Figure D.7). Hence, a measurement of a helix based

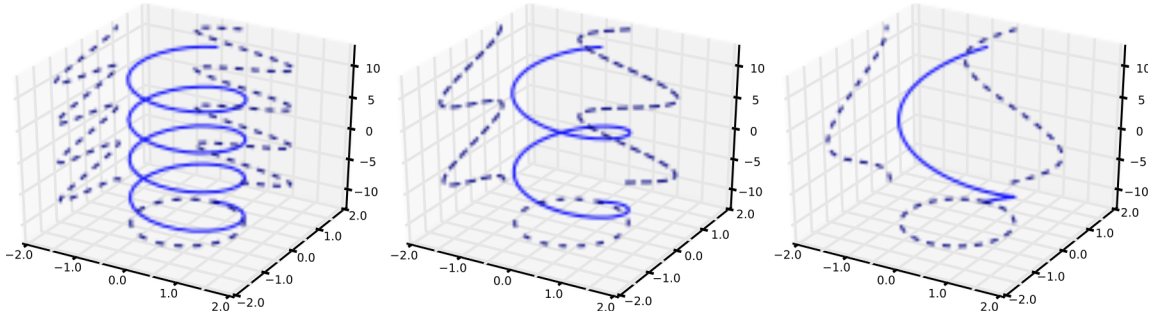

Figure D.7: Three helices with a radius of 1 and a pitch of a.) 2π, b.) 4π, or c.) 8π. Dashed lines show projections of each curve into the three orthogonal planes of its bounding box.

on this projection underestimates the true length of the helix by the ratio

$$\begin{aligned}\frac{\text{length of sinusoid}}{\text{length of helix}} &= \frac{\int_{\theta=0}^{\theta=2\pi}\sqrt{(\mathrm{d}x)^2+(\mathrm{d}z)^2}}{\int_{\theta=0}^{\theta=2\pi}\sqrt{(\mathrm{d}x)^2+(\mathrm{d}y)^2+(\mathrm{d}z)^2}} \\ &= \frac{\int_0^{2\pi}\sqrt{a^2\sin^2\theta+b^2}\,\mathrm{d}\theta}{\sqrt{a^2+b^2}\int_0^{2\pi}\mathrm{d}\theta}\end{aligned} \tag{D.3}$$

where the projection onto the xz plane has been used for the calculation (without loss of generality, since the integral is over one full turn of the helix). The numerator in Equation D.3 is a well-disguised elliptic integral. Letting $m = (a/b)^2$ and taking advantage of the symmetry of the sine function, this integral becomes

$$\begin{aligned}4b\int_{\theta=0}^{\theta=\pi/2}\sqrt{1+m\sin^2\theta}\,\mathrm{d}\theta &= 4b\sqrt{1+m}\int_{\theta'=0}^{\theta'=\pi/2}\sqrt{1-\left(\frac{m}{1+m}\right)\sin^2\theta'}\,\mathrm{d}\theta' \\ &= 4b\sqrt{1+m}\,E\left(\frac{m}{1+m}\right) \\ &= 4\sqrt{a^2+b^2}\,E\left(\frac{a^2}{a^2+b^2}\right)\end{aligned} \tag{D.4}$$

where the first line uses the transformation $\theta = \pi/2 - \theta'$ to get the standard form for E, the complete elliptic integral of the first kind [61]. Substituting this result back into D.3, we find that

$$\frac{\text{length of sinusoid}}{\text{length of helix}} = \frac{2}{\pi}\,E\left(\frac{a^2}{a^2+b^2}\right). \tag{D.5}$$

$E(x)$, shown in D.8 varies from 1 for $a \gg b$ (an extremely compressed spring) to $\pi/2$ for $a \ll b$ (an extremely stretched spring). Hence, the measured length of the projection ranges from 64 percent

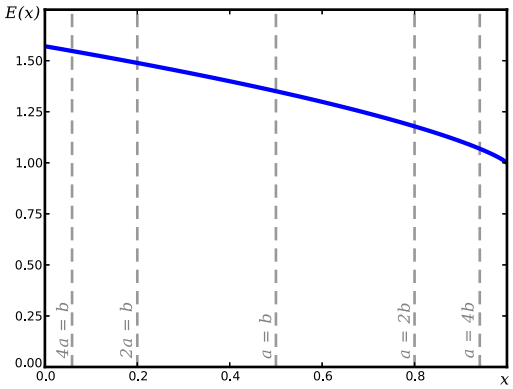

Figure D.8: Plot of $E(x)$. Dashed lines indicate x values for several ratios of helix parameters a, b

of the true helix length (in the former limit) to equaling the true helix length (in the latter limit).

Experimental loops at their most kinked suggest $a \approx b$, based on a comparison of the size of the dip at the apex of late frame traces to the distance between the adjacent peaks. This is also the average[5] for the mathematical curves in Figure D.5. At that ratio of radius to pitch, the projection of a straight helix measures in at 86 percent of the true helix length.

D.7 Summary and discussion

This appendix has analyzed various possible sources of uncertainty, variation, and error in the tracing of plasma loops. The quantitative effects on curve length measurements are summarized in Table D.1.

Single-species loops of the same helicity beget highly precise curve length measurements, with the shot-to-shot variation approaching that of the loop tracing method itself. Sets of shots including both left- and right-handed loops have greater measurement variations by just a few percent, despite qualitative differences in curve shape (beyond those attributable to the viewing angle). Single-species loops are, thus, quite amenable to being represented by individual shots.

Dual-gas loop traces exhibit more quantitative variation, since different methods of image processing suggest different "best" choices for designating the boundary between plasma species. Were a precise quantitative study to require the use of dual-gas single loops, it would be advisable for the experimenter(s) to mollify the ambiguities by specifying image processing and tracing guidelines.

The tracing method itself also has built into it the systematic error that comes from measuring a three-dimensional structure based on its two-dimensional projection. For loops at early times that have not yet developed a significant kink, this error is largely ameliorated by correcting for

source	size of effect	comments
tracing method	1.8 % (st. dev)	present in all loop traces
shot-to-shot variation (single helicity)	2–3 % (st. dev) *	
shot-to-shot variation (mixed helicity)	4–6 % (st. dev) *	
species boundary ambiguity	13.4 % (st. dev) *	dual-gas loop traces only
viewing angle uncertainty	$< \pm 1$ %	
projection of a helix	up to -14 %	systematic underestimate

* Includes tracing method uncertainty.

Table D.1: Quantitative summary of uncertainties/errors/variations in loop traces

[5]Due to the arched axis the pitch is smaller along the inner side of the curves (i.e., closer to the origin) and greater along the outer side. On average, however, each curve undergoes two twists with minor radius $a = 1$ over a length of 4π.

the viewing angle of the camera. For loops at later times with large kinks, the projection may underestimate the loop length by as much as 14 percent.

Although this is larger than the other uncertainties and errors described here, it is relatively small compared to typical uncertainties in plasma parameters (e.g., the number density). Also, because it is systematic, there are many measurements that would not be affected (e.g., the time it takes for a plasma loop to reach a certain size).

One possible impact is on the curvature of $s(t)$, the length of a plasma loop as a function of time (as discussed in great detail in Chapter 3), since the y-values for points corresponding to later times may be deflated up 14 percent, whereas y-values of points at earlier times should be fairly accurate. If that were the case, an analysis that compensates for the growth of the kink would steepen the slope of $s(t)$ at later times, possibly resulting in a better fit of numerical solutions $s_{num}(t)$ to the experimental data.

Appendix E

Species variation in single-gas loops

Single loop plasma structures are so highly reproducible in their dynamic evolution that nearly any image series can be overlaid with any other from the same experiment setup. Furthermore, from one plasma species to the next, the overall dynamics scale very consistently, yet some smaller differences do exist. For anyone working with loops of different species — or even someone working with just one species, but who is seeking to reproduce or build on a result originally observed in a different species — these are things to be aware of.

E.1 In images

All three gases produce bright, collimated loops. The argon loops, however, tend to have a subtly different character from the other two species. Nitrogen and hydrogen loops are not perfectly identical, but they are quite close; recall that Figure D.4 showed them side-by-side. By comparison, the hydrogen and argon loops in Figure E.1 are not as similar to one another.

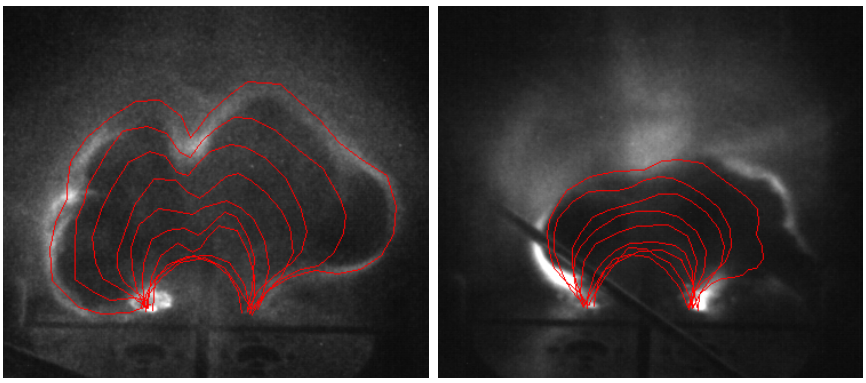

Figure E.1: A set of hydrogen loop traces and a set of argon loop traces, each overlaid on a late time image from their respective shot. *(shots 9105 and 9071)*

The argon image loop is preceded into the chamber by a bright spot just above its apex, it doesn't kink as much, and — as is very clear from the overlaid loop traces — it never gets as big. Argon loops consistently disconnect from the electrode much earlier in their evolution process than do hydrogen or nitrogen loops. Coincidentally, this means the slower-moving argon loops and the faster-moving hydrogen loop both last around the same amount of time (5–6 μs for a 4 kV shot).

A likely explanation for the seemingly premature demise of argon loops is the kink-induced Raleigh-Taylor instability identified by Moser [4].

E.2 In IV data

Trends in current and voltage data can be more difficult to pin down, due to more intraspecies variation and a lack of clear correspondence with the plasma behavior. During one set of shots, the hydrogen currents may be ringing unhindered, while during another they may look like something took bites out of their first peaks. Yet, the image sequences can look the same for both. Overall, though, nitrogen plasmas seem less prone to nonsinusoidal current profiles.

Voltage traces are quite consistent from species to species once breakdown occurs. (The time until breakdown varies, due to the gases' different Paschen curves.)

Figure E.2 offers a quick survey of current and voltage traces of a selection of plasma loops.

E.3 In magnetic data

Probably the most consistent difference is seen in the magnetic data. A representative example is shown in Figure E.3. Nitrogen loops produce the "cleanest" magnetic data, with sharp peaks in the total field and reasonably simple-looking components. Argon data looks pretty similar, just stretched out because the loop moves more slowly past the probe. Hydrogen magnetic peaks, however, instead of looking like skinnier nitrogen peaks, are ugly.

They are always wider (despite being faster moving), often have a double peak in the total magnetic data (as seen here), and have much more complicated components. An important thing to consider is that bright collimated loops rarely last longer than ~ 5 μs after breakdown — which corresponds to around 21 μs in the plots shown here. Since much of the excitement in the hydrogen data happens after this time, one could just chalk it up to "whatever happens after the loop is gone". Recall, however, that the loop lifetime is similar for nitrogen plasmas, and might even be a bit

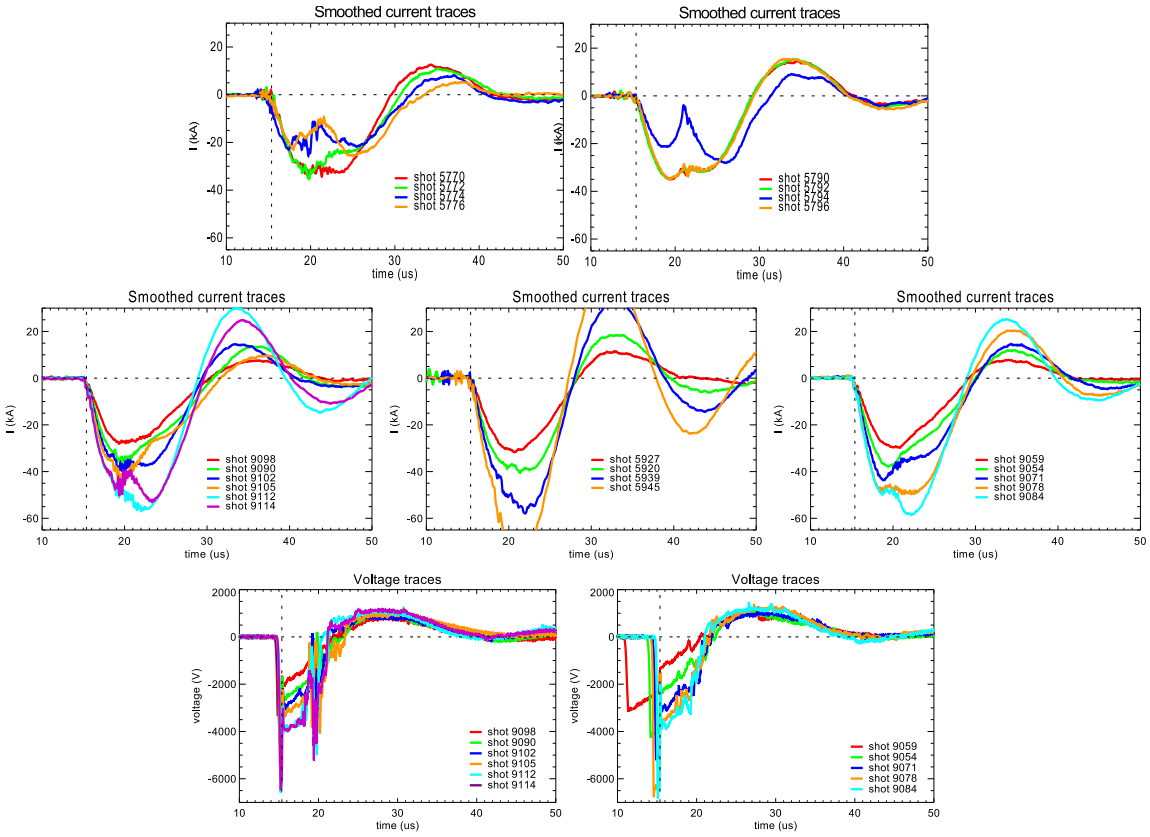

Figure E.2: Top row: Hydrogen (left) and argon (right) plasmas seem more prone to large dips in their current traces than nitrogen plasmas. Middle row: The hydrogen (left), nitrogen (center), and argon (right) plasma loops from Chapter 3 all had fairly uninterrupted currents. Bottom row: Hydrogen (left) and argon (right) voltage traces exhibit shot-to-shot variation during the plasma lifetime due to being fired from different charging voltages, but otherwise have little to distinguish them from one another.

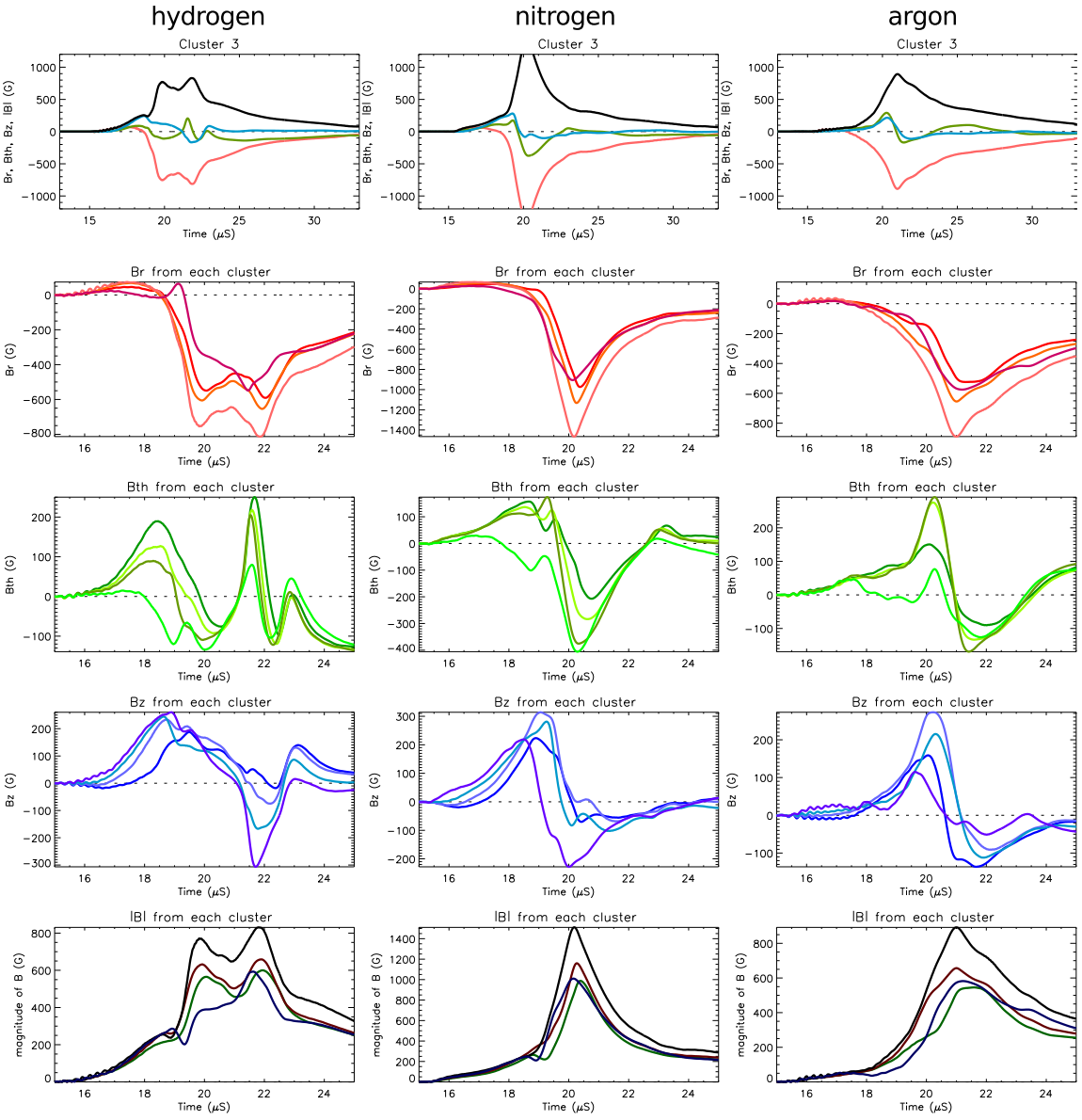

Figure E.3: Magnetic measurements for hydrogen, nitrogen, and argon loops that had the same experimental conditions (except for neutral gas species and pressure). The top row shows the data from cluster 3 (which had the largest magnitude). The next four rows are the data from all four clusters, grouped by components (in the frame of the probe, which was in the same location for all three shots). *(shots 5888, 5785, and 5789)*

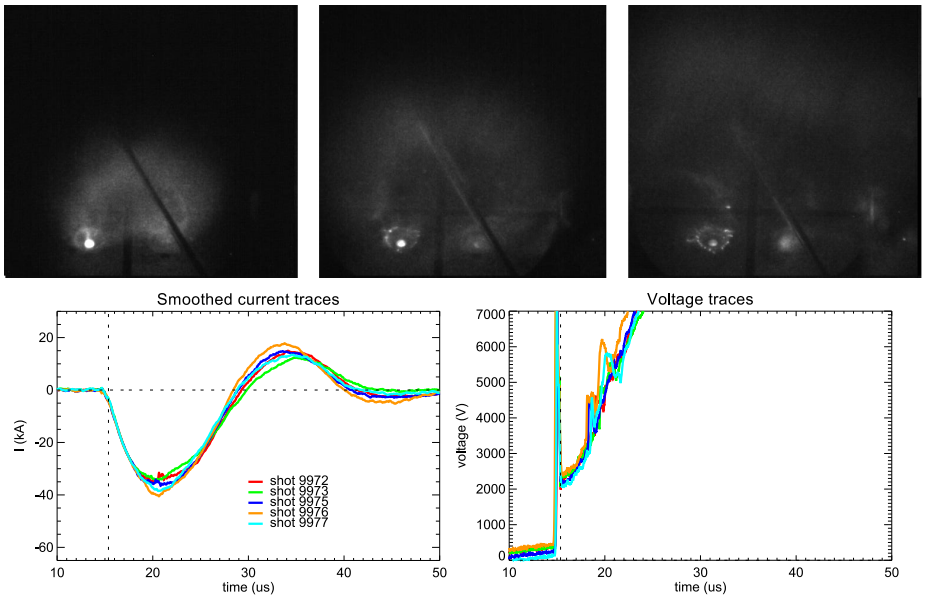

Figure E.4: Top row: A typical neon plasma, diffuse and uncollimated *(shot 9972)*. Bottom row: IV traces for several neon shots

shorter for argon plasmas (as mentioned above), while magnetic data from those two species look very plausibly like flux tubes for the entire time window.

Hence, it is not obvious whether it is the hydrogen loops that are anomalously messy or the nitrogen and argon loops that are anonymously clean. In any case, a person taking magnetic data from a hydrogen loop and expecting it to look like the data from a nitrogen loop will be disappointed.

E.4 Regarding neon loops

There aren't two ways about it: neon loops are duds when it comes to image data. One would expect standard-looking, bright kinked arches with speeds somewhere between corresponding nitrogen and argon plasmas, but neon loops never exhibit collimation.

Figure E.4 shows a typical neon plasma, as well as several current and voltage traces. Most notable about the IV data is the unusual range of the voltage data. What happened is that the plasma took so long to break down, the increasingly inaccurate voltage signal[1] made it all the way up into positive numbers. Hence, neon's poor performance might be related to its Paschen curve.

Alternately, it may be possible that neon loops *do* have dense, collimated cores that do not emit in the visible range; given the abundance of available emission lines, though, this seems unlikely.

[1]Recall that a transformer installed between the optical receiver and the VME caused low-frequency signals not to be transmitted accurately.

Appendix F

Further adventures in numerical integration

The numerical integration results presented in Chapter 3 appear to be correct in magnitude, as they yield plausible values for κ. The fit, however, could be better. This appendix covers other models that have been fit to the data via numerical integration. None tried thus far has produced a better match than the simplified hoop force model.

F.1 Key issues

Finite $R(0)$ begets nonconstant $\ddot{R}(t)$: Recall from the experimental data that plasma curve lengths experience constant acceleration. This is also true for the simplified hoop force model, when $R(0) = 0$. The greater $R(0)$ is, though, the less the numerical solutions to Equation 3.28 resemble a constant acceleration profile. This is true even for the case when $I(t)$ rises linearly throughout, as shown in Figure F.1.

When $I(t)$ is sinusoidal, the effect is even more pronounced, as can be seen from the first and

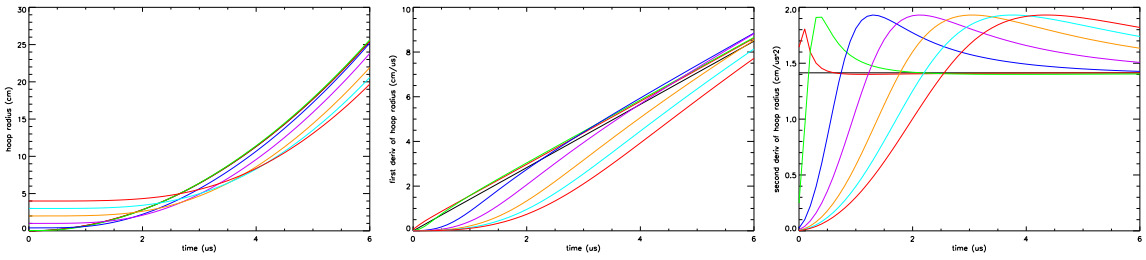

Figure F.1: The hoop radius (left) and its first (center) and second (right) time derivatives for analytic (black) and numerical solutions for the simplified hoop force model with linear current. Each color indicates a different value of $R(0)$.

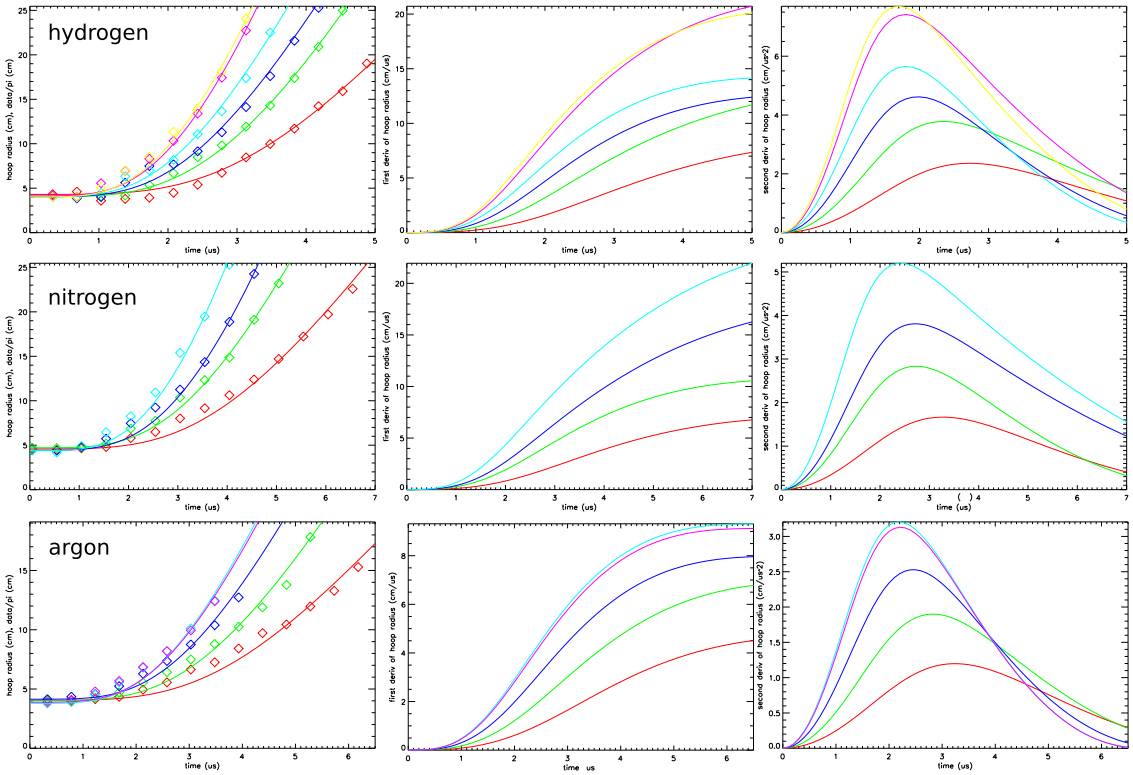

Figure F.2: The curves $R_{num}(t)$ fit to experimental plasma loop data, along with their first and second derivatives

second derivatives of the solutions for the loops from Chapter 3, shown in Figure F.2.

If a different expression for $\ddot{R}(t)$ produced flatter acceleration profiles (while still plausibly capturing the physics of plasma loop expansion), it might be a better candidate than the simplified hoop force model.

Constant κ: Another nonideal feature of the numerical results for the simplified hoop force model was the trend in κ (originally conceived as a constant) for hydrogen shots fired from different voltages. Thus a model that eliminates this trend (again, while still providing a physically sound description of the loop behavior) would also be nice.

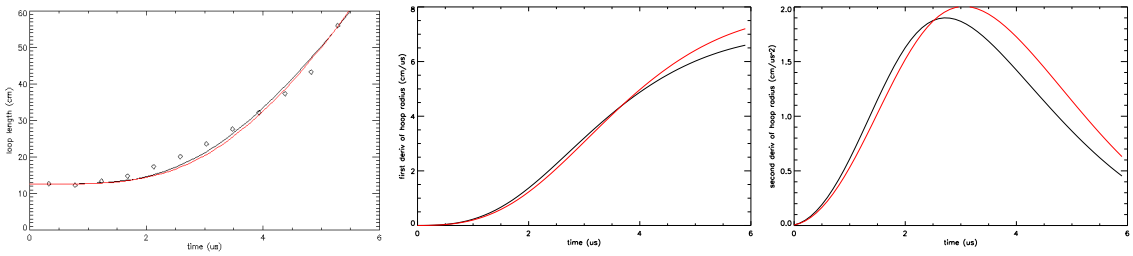

Figure F.3: Numerically solved $R(t)$ using the full expression for the hoop force (Equation F.1) and $a = 1$ cm, for a hydrogen loop. And its first and second derivatives. For comparison, the simplified hoop force solution is shown in black. *(shot 9054)*

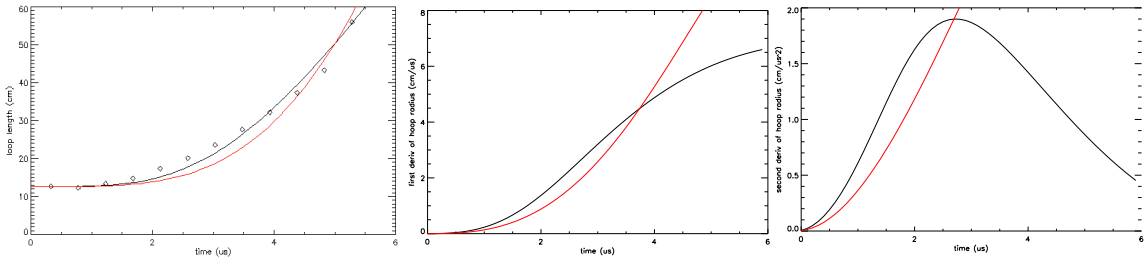

Figure F.4: Numerically solved $R(t)$ for the decreasing density model (Equation F.2), for a hydrogen loop. And its first and second derivatives. For comparison, the simplified hoop force solution is shown in black. *(shot 9054)*

F.2 The options considered

The first, most obvious thing to consider is a return to the full form for the hoop force, with the logarithmic term. This can be written as

$$\ddot{R}(t) = \kappa_2 \frac{I(t)^2}{R(t)} \left(\ln \left(\frac{R(t)}{a} \right) + 1.33 \right) \tag{F.1}$$

where κ_2 is the new adjustable parameter, the axial current distribution has been approximated as uniform ($Y = 0.25$), and a value must be chosen for a.

A typical result is shown in Figure F.3. There isn't much of a change, but what there is fits the data even less well. When applied for multiple hydrogen shots to examine the trend in κ, the trend showed a slight reduction in magnitude ($\sim$10 percent), but still remained.

A second option is to ignore loop brightness and suppose that plasma flows do not, in fact, enter the loop. The loop's density would then decrease, inversely proportional to the increasing loop

length. This would give the expression

$$\ddot{R}(t) = \kappa_3 I(t)^2 \left(\ln\left(\frac{R(t)}{a}\right) + 1.33 \right) \tag{F.2}$$

if one keeps the slowly changing logarithmic part, or simply $\ddot{R}(t) = \kappa_{3'} I(t)^2$ if one approximates it as constant. Either way, the acceleration is huge and the loop takes off far faster than experimental loops. An example is shown in Figure F.4.

A third, more promising idea is to add in the magnetic field line tension that has been neglected from the problem thus far. An order of magnitude estimate suggests that the increase in axial magnetic field density that accompanies the increase in loop length would represent an energy increase of 1–10 J. This is akin to the kinetic energy of the moving loop (estimated to be 2–13 J), which makes it appear to be a plausible factor in the loop acceleration.

However, the expression for the force due to the magnetic field line tension that was used for previous experiment applications [44] is not easily incorporated into the numerical model[1], nor does it offer an intuitive picture as to how the fit or κ might be affected.

Other expressions have not yet been tried. Relatedly, it is somewhat unclear whether the data are sufficiently accurate to effectively offer support for or against the more subtle permutations.

[1] Specifically, it causes the loop length to "crash" early on and never recover for any physically relevant estimate of B_{axial}.

Appendix G

Alfven speed contours for plasma parameter ranges of interest

The Alfven speed of a magnetized plasma is given by

$$v_A \equiv \frac{B}{\sqrt{\mu_0 \rho}} \tag{G.1}$$

where B is the magnitude of the magnetic field, ρ is the plasma mass density, and μ_0 is the permeability of free space.

It is so named because Hannes Alfven in 1943 derived that this is the speed at which a perpendicular perturbation to the magnetic field of an MHD plasma would, in the limit of zero pressure, propagate along the magnetic field (i.e., as a transverse wave). In fact, v_A is featured in other dispersion relations as well, and can be thought of as the fundamental speed at which "communication" through the plasma occurs [1].

Alternately, v_A is an expression of the "floppiness" of a plasma: how strong (and, therefore, resistant to bending) the magnetic field is compared to the inertia of the plasma mass.

In hopes of being a useful reference, this appendix provides contour plots of Alfven velocities as a function of the magnetic field and the number density for hydrogen, nitrogen, and argon, in and around the parameter space of the Caltech solar experiment.

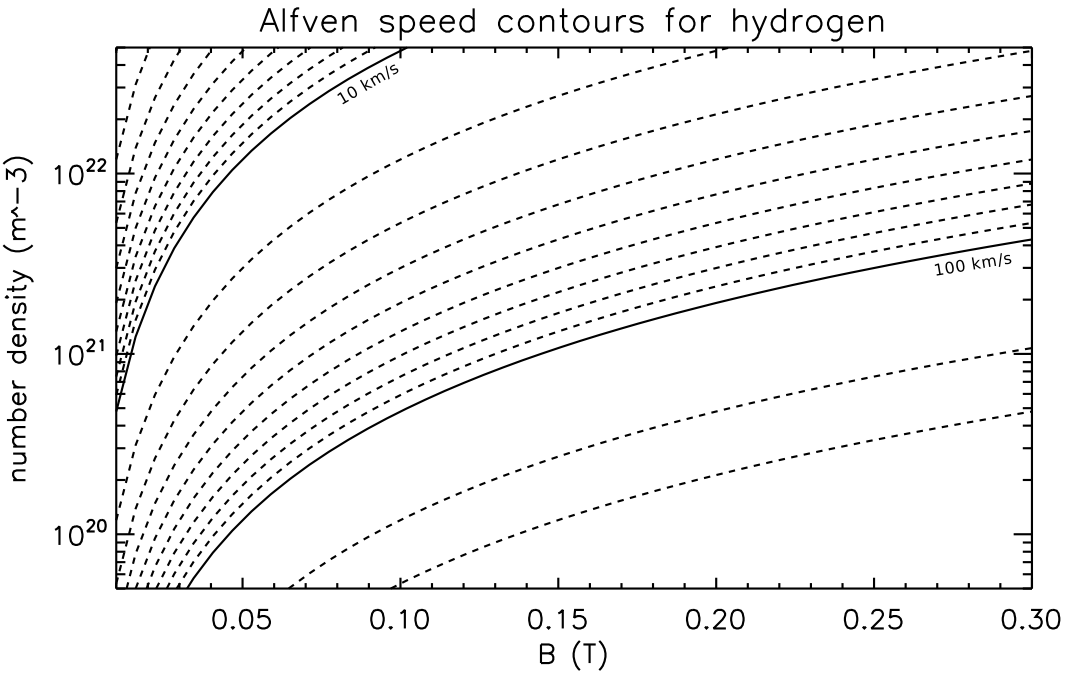

Figure G.1: Contour plot of Alfven speeds for hydrogen plasmas

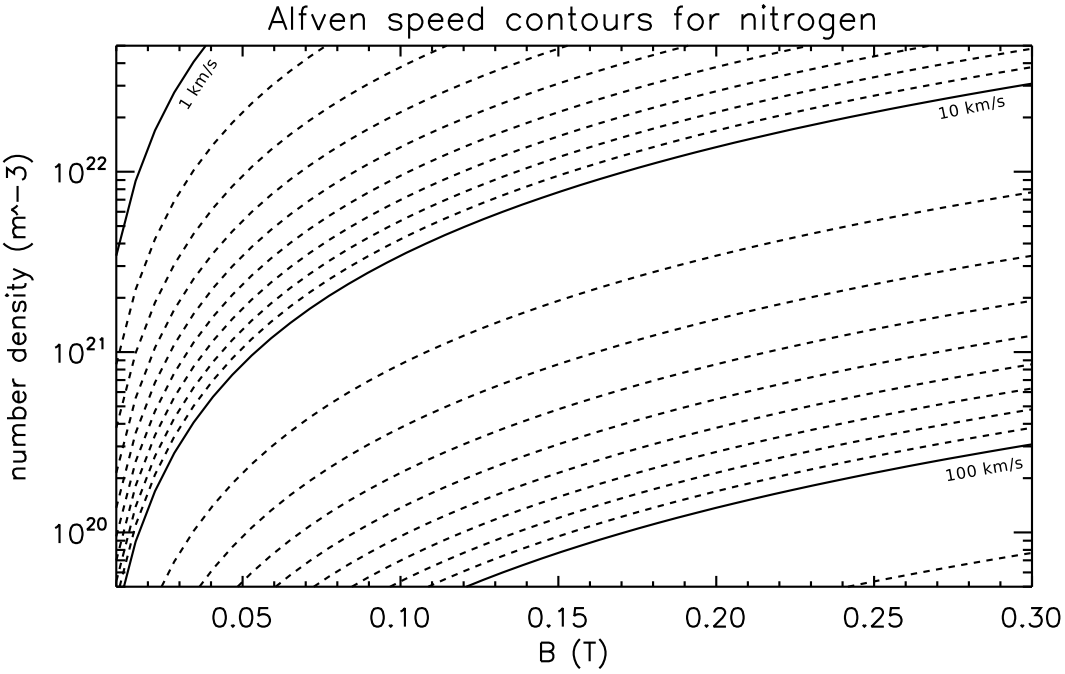

Figure G.2: Contour plot of Alfven speeds for nitrogen plasmas

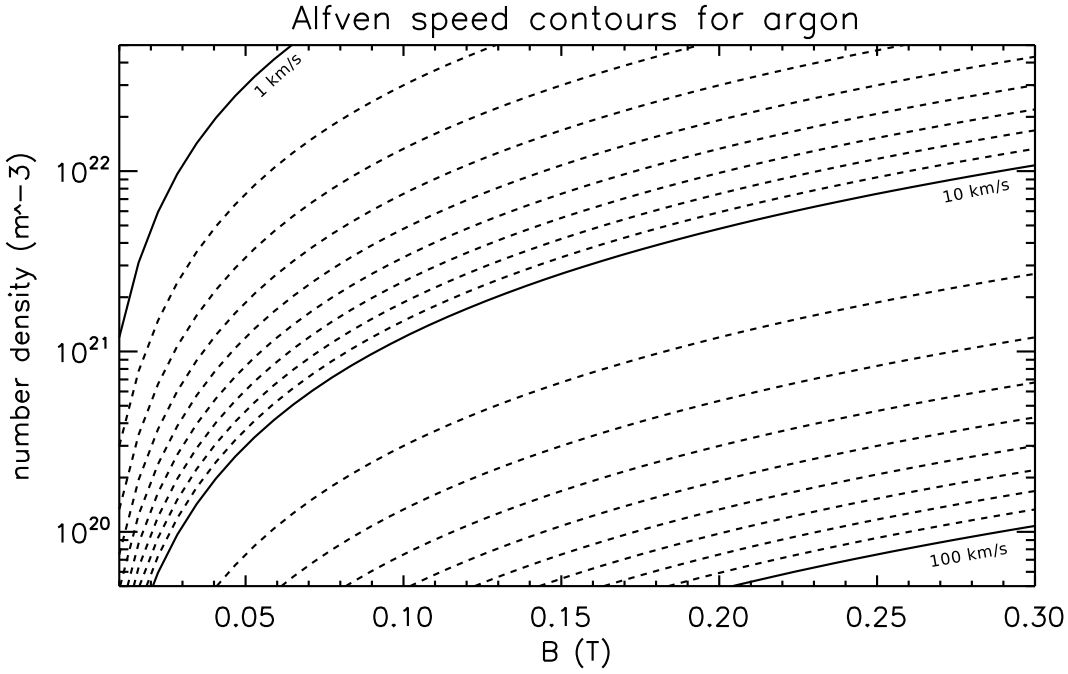

Figure G.3: Contour plot of Alfven speeds for argon plasmas

Appendix H

Timing survey for single-loop plasmas

H.1 Method

In order to better understand the sometimes varied properties of current and voltage traces, an IDL program was written to identify the following potential features of interest, as determined from the smoothed current and voltage traces:

- time at which the bank fired, and the resulting voltage;
- breakdown time and voltage, determined by the end of voltage "mesa" (which coincides with the beginning of the current rise);
- time of the optical collimator pulse leading edge;
- positive peak of the voltage trace (time and value);
- minimum current peak (time and value);
- area under the first peak of the current (i.e., charge);
- time of the first current zero;
- maximum current peak (time and value);
- and time of the second current zero.

These features, except for the trigger from the collimator pulse, are illustrated in Figure H.1. Multiple sets of plasma shots were then analyzed with the program, resulting in a survey of the listed features for more than 250 experiments.

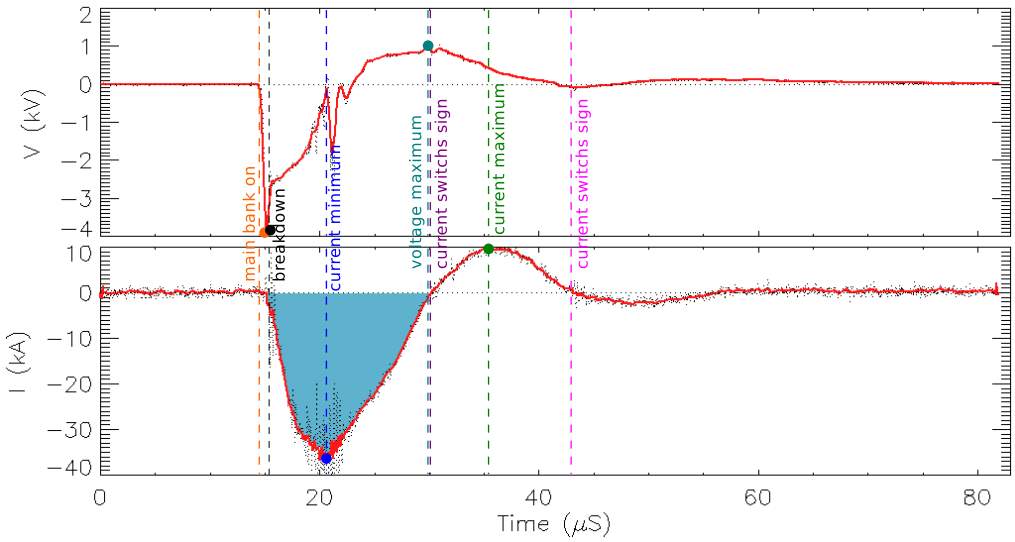

Figure H.1: IV properties surveyed (except for the optical pulse leading edge, which doesn't appear on current and voltage traces). Dashed lines indicate times tabulated. Points indicate where both times and currents or voltages were tabulated. The area under the first current peak (shaded blue) was integrated numerically. *(shot 9094)*

H.2 Results

Some of the survey results confirmed phenomena that were intuitive or expected. Figure H.2a illustrates that the area under the first current peak is proportional to the height of that peak, indicating the peaks scale fairly self-similarly. While this particular plot is for a set of nitrogen shots, hydrogen and argon sets produced similar trends (though with more scatter), despite their current traces often having a jagged "dip" in the center. Figure H.2b illustrates a related trend: the area under the first current peak as a function of the width of that peak; this trend is also present across all gases. Figure H.2c shows that increasing the voltage applied across the electrodes decreases the time to breakdown, as one would expect from the physics of the electron avalanche involved.

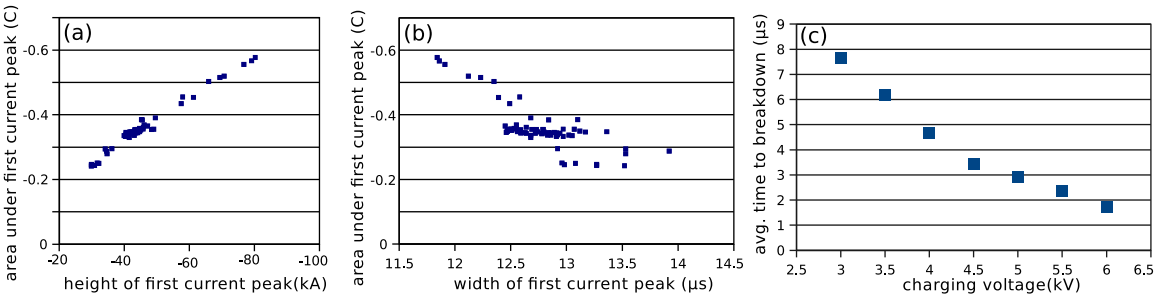

Figure H.2: Survey results for a set of nitrogen plasmas

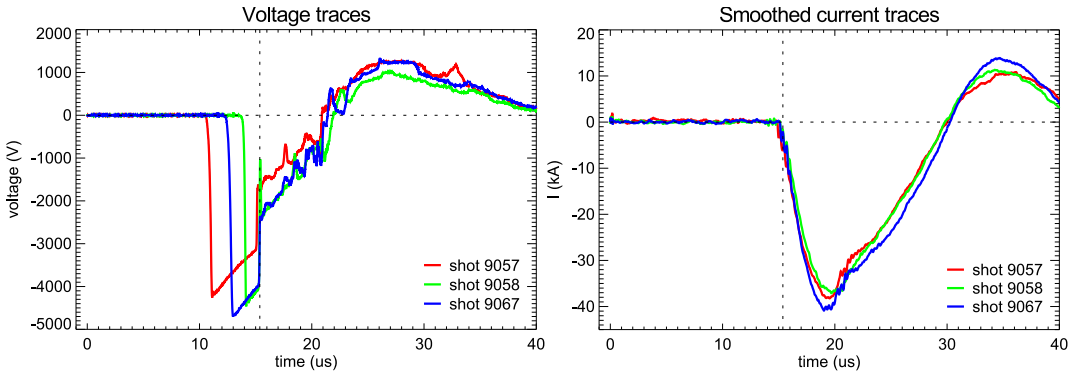

Figure H.3: The "firing voltage" (measured voltage at the time of breakdown) appeared to be unrelated to the current profile

Other results were less anticipated. Although the measured voltage dropped rapidly during the time between the application of high voltage and the plasma breakdown, this seemed to have little effect on the resulting current amplitude, which instead still scaled with the charging voltage. This effect is shown in Figure H.3. The reason, it turned out, was a loss of lower frequency signal components, due to the introduction of a transformer between the optical receiver and the VME (so as to prevent ground loops). Xiang Zhai's new voltage probe solves this issue.

Another finding of note is that the voltage maximum does not necessarily coincide with the current zero. Even though shots like the one in Figure H.1 may suggest this to be the case, Figure H.4a indicates otherwise.

Figures H.4b–c show that both dual-gas plasmas and plasmas with "exotic" magnetic field configurations (which often don't result in bright, collimated flux tubes) still exhibit the same trends in their current traces as do collimated single-gas loops. (Compare to Figure H.2a–b.) Although dual-gas loops with standard vacuum field configurations evolve with the same scaling as do single-gas

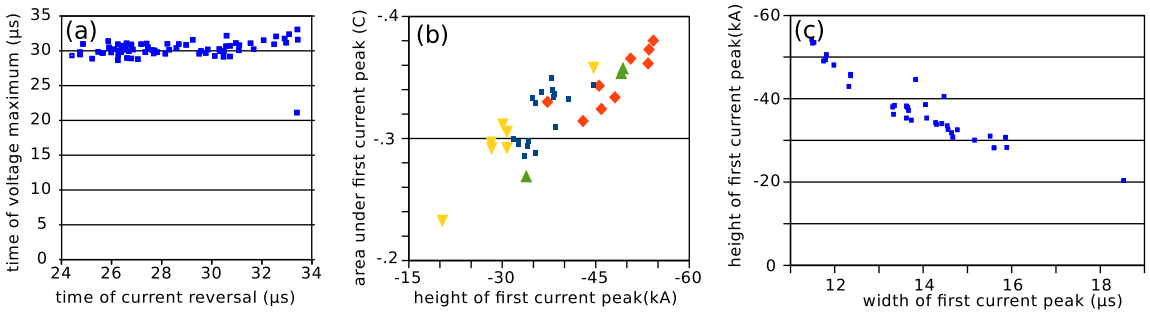

Figure H.4: Survey results for a.) set of hydrogen plasmas, and b–c.) a set of argon/hydrogen dual-gas plasmas. The different symbols in (b.) represent different vacuum magnetic field configurations (no field, one coil, etc.).

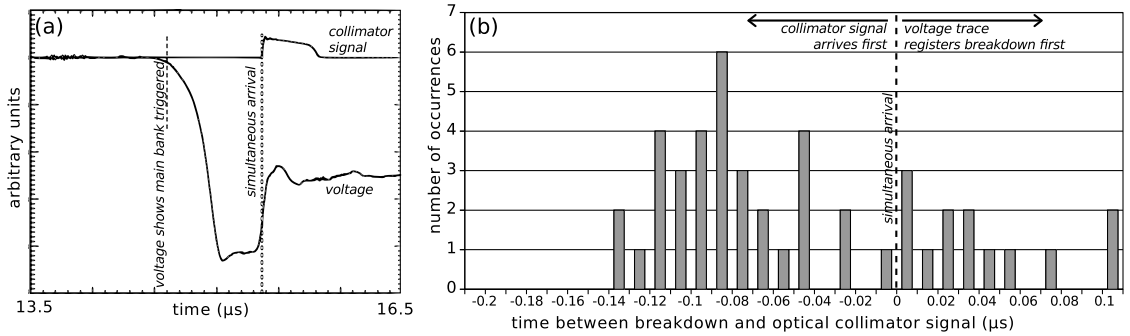

Figure H.5: "Speedy" optical collimator signals (implying delayed voltage data). a.) Data from the VMA shows the collimator signal arriving simultaneously with the voltage drop that indicates breakdown. *(shot 9094)* b.) Histogram of differences between the two timing events for a set of nitrogen shots; the horizontal axis shows the boundaries of the bins. (For example, there were six cases in which the collimator edge was recorded between 0.08 and 0.09 μs before the voltage drop.)

loops (Chapter 3), plasmas with nonstandard configurations usually do not (Chapter 5). Hence, the lack of a clear difference in their current profiles is consistent with the capacitor acting as a current source, and with the idea that the current may "ignore" unfavorable magnetic configurations and flow elsewhere.

Figure H.5 shows another surprising feature: the pulse from the optical collimator is often recorded at the VME simultaneously or even before the voltage drop associated with breakdown. Since this should be physically impossible (it takes ~ 0.15 μs for the emission from the plasma to reach the threshold necessary to send an optical signal from the collimator[1]), it indicates a delay in the transmission of the IV signals that is longer than that for the collimator transmission (and isn't usually considered).

Finally, one of the more extensive sets of results comes from an examination of the delay in breakdown (of which Figure H.2c is just one part). The resulting data set, shown in Figure H.6, offers a guide for anyone looking to time events with early stages of plasma formation (prior to the optical collimator signal). Two trends are clear and easy to explain:

1. The delay is shortest for hydrogen, longest for nitrogen, and in between for argon. This is likely attributable to the three gases' different Paschen curves and relative densities.

2. Increasing the charging voltage decreases the breakdown time in all cases (again, as one would expect).

However, it is a mystery as to why the delay for hydrogen shots was longer for the plasmas made

[1]This was calculated by Deepak Kumar and Gunsu Yun when the diagnostic timing set-up was installed.

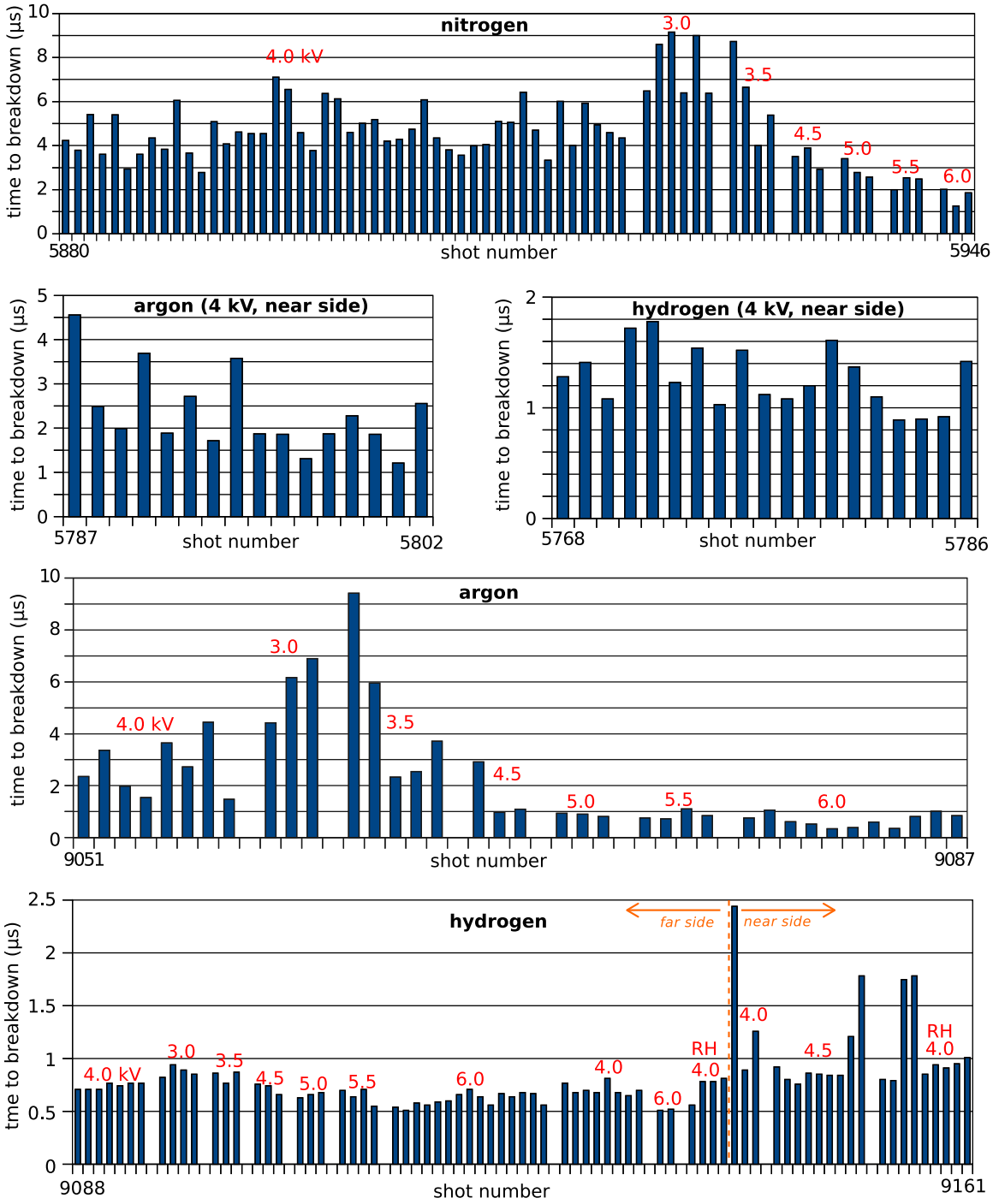

Figure H.6: Breakdown delays for five sets of single-gas, single-loop shots. The vertical axes measure the delay between the time the main bank is fired and the time of the optical collimator pulse leading edge. "Breakdown jitter" is the variation in the size of the bars (which represent the delay lengths for individual shots) for the same experiment parameters. Blank spaces are used as a visual aid to separate shots with different charging voltages, indicated in red. "RH" indicates right-handed loops in an otherwise left-handed set. "Far side" and "near side" refer to the halves of the electrode relative to the viewing windows.

on the near side of the electrode than on the far side.

H.3 Conclusions

There is a great deal of information available to be mined from the specifics of the current and voltage traces. In order to see it, one must extract the parameters of interest in a methodical and/or automated fashion. Doing so can yield confirmation of features that were inferred or assumed; identification of unexpected or not-yet-explained features; and/or an indication as to which diagnostics could use a tune-up.

Bibliography

[1] P. M. Bellan. *Fundamentals of Plasma Physics*. Cambridge University Press, 2006.

[2] J. Dietrich. William A. Fowler: Nobel Laureate 1983. *Engineering and Science*, 47(2), 1983.

[3] F. F. Chen. *Introduction to plasma physics and controlled fusion*. Plenum Press, 2nd edition, 1984.

[4] A. L. Moser and P. M. Bellan. Magnetic reconnection from a multiscale instability cascade. *Nature*, 482:379–381, 2012.

[5] S. K. P. Tripathi, P. M. Bellan, and G. S. Yun. Observation of Kinetic Plasma Jets in a Coronal-Loop Simulation Experiment. *Physical Review Letters*, 98(13):135002, 2007.

[6] W. D. D'haeseleer, W. N. G. Hitchon, J. D. Callen, and J. L. Shohet. *Flux Coordinates and Magnetic Field Structure: A Guide to a Fundamental Tool of Plasma Theory*. Springer-Verlag, 1991.

[7] D. Alexander. *The Sun*. Greenwood Press, 2009.

[8] M. J. Aschwanden. *Physics of the Solar Corona: An Introduction with Problems and Solutions*. Springer, 2nd edition, 2005.

[9] D. S. De Young. Astrophysical Jets. *Science*, 252:389–396, 1991.

[10] P. M. Bellan. *Spheromaks: A Practical Application of Magnetohydrodynamic Dynamos and Plasma Self-Organization*. Imperial College Press, 2000.

[11] W. M. Stacey. *Fusion: An Introduction to the Physics and Technology of Magnetic Confinement Fusion*. Wiley-VCH, 2010.

[12] K. H. Finken, S. S. Abdullaev, M. W. Jakubowski, M. F. M. de Bock, S. Bozhenkov, C. Busch, M. von Hellermann, R. Jaspers, Y. Kikuchi, A. Krämer-Flecken, M. Lehnen, D. Schega,

O. Schmitz, K. H. Spatschek, B. Unterberg, A. Wingen, R. C. Wolf, O. Zimmermann, and the TEXTOR team. Improved Confinement due to Open Ergodic Field Lines Imposed by the Dynamic Ergodic Divertor in TEXTOR. *Physical Review Letters*, 98:065001, 2007.

[13] V. Archontis, A. W. Hood, and C. Brady. Emergence and interaction of twisted flux tubes in the Sun. *Astronomy and Astrophysics*, 466:367–376, 2007.

[14] J. E. Leake, M. G. Linton, and S. K. Antiochos. Tests of dynamical flux emergence as a mechanism for coronal mass ejection initiation. *The Astrophysical Journal*, 722(1):550–565, 2010.

[15] L. Arnold, J. Dreher, R. Grauer, H. Soltwisch, and H. Stein. Three-dimensional magnetohydrodynamical simulation of expanding magnetic flux ropes. *Physics of Plasmas*, 15(4):042106, 2008.

[16] M. G. Linton, R. B. Dahlburg, and S. K. Antiochos. Reconnection of Twisted Flux Tubes as a Function of Contact Angle. *The Astrophysical Journal*, 553:905, 2001.

[17] G. Allen Gary. Plasma Beta above a Solar Active Region: Rethinking the Paradigm. *Solar Physics*, 203:71–86, 2001.

[18] H. Lin, M. J. Penn, and S. Tomczyk. A New Precise Measurement of the Coronal Magnetic Field Strength. *The Astrophysical Journal Letters*, 541:L83, 2000.

[19] H. Lin, J. R. Kuhn, and R. Coulter. Coronal Magnetic Field Measurements. *The Astrophysical Journal Letters*, 613:L177, 2004.

[20] S. Tomczyk, G. L. Card, T. Darnell, D. F. Elmore, R. Lull, P. G. Nelson, K. V. Streander, J. Burkepile, R. Casini, and P. G. Judge. An Instrument to Measure Coronal Emission Line Polarization. *Solar Physics*, 247:411–428, 2008.

[21] S. Liu, H. Q. Zhang, and J. T. Su. Comparison of Nonlinear Force-Free Field and Potential Field in the Quiet Sun. *Solar Physics*, 270:89–107, 2011.

[22] Y. Liu and H. Lin. Observational Test of Coronal Magnetic Field Models. I. Comparison with Potential Field Model. *The Astrophysical Journal*, 680:1496, 2008.

[23] D. Alexander. Laboratory Exploration of Solar Energetic Phenomena. *Astrophysics and Space Science*, 307:197–202, 2007.

[24] X. Sun, T. P. Intrator, L. Dorf, J. Sears, I. Furno, and G. Lapenta. Flux Rope Dynamics: Experimental Study of Bouncing and Merging. *Physical Review Letters*, 105:255001, 2010.

[25] S. K. P. Tripathi and W. Gekelman. Laboratory Simulation of Arched Magnetic Flux Rope Eruptions in the Solar Atmosphere. *Physical Review Letters*, 105(7):075005, 2010.

[26] E. G. Zweibel, E. Lawrence, J. Yoo, H. Ji, M. Yamada, and L. M. Malyshkin. Magnetic reconnection in partially ionized plasmas. *Physics of Plasmas*, 18(11):111211, 2011.

[27] J. F. Hansen. *Laboratory Simulations of Solar Prominences*. PhD thesis, California Institute of Technology, 2001.

[28] S. C. Hsu and P. M. Bellan. A laboratory plasma experiment for studying magnetic dynamics of accretion disks and jets. *Monthly Notices of the Royal Astronomical Society*, 334:257–261, 2002.

[29] J. Yee. *Experimental investigations in spheromaks: injection into a tokamak and formation in an unbounded environment*. PhD thesis, California Institute of Technology, 2000.

[30] G. S. Yun. *Dynamics of Plasma Structures Interacting with External and Self-Generated Magnetic Fields*. PhD thesis, California Institute of Technology, 2008.

[31] D. Kumar. *Experimental Investigations of Magnetohydrodynamic Plasma Jets*. PhD thesis, California Institute of Technology, 2009.

[32] R. J. Perkins. *Experimental and analytical studies of plasma loops on the Caltech solar loop experiment*. PhD thesis, California Institute of Technology, 2011.

[33] S. C. Hsu and P. M. Bellan. Experimental Identification of the Kink Instability as a Poloidal Flux Amplification Mechanism for Coaxial Gun Spheromak Formation. *Physical Review Letters*, 90:215002, 2003.

[34] C. A. Romero-Talamás, P. M. Bellan, and S. C. Hsu. Multi-element magnetic probe using commercial chip inductors. *Review of Scientific Instruments*, 75:2664, 2004.

[35] W. H. Press, B. P. Flannery, S. A. Teukolsky, and W. T. Vetterling. *Numerical Recipes in C: The Art of Scientific Computing, Second Edition*. Cambridge University Press, 1999.

[36] PPPL generals prep: Hoop Force, 2010. Website: http://qed.princeton.edu/main/PPL_generals_prep/Hoop_Force.

[37] A. Otsuka, T. Kiyoshi, and M. Takeda. A 1.3 GHz NMR Magnet Design Under High Hoop Stress Condition. *IEEE Transactions on Applied Superconductivity*, 20(3):596–599, 2010.

[38] K. Shikimachi, T. Tamada, M. Naruse, N. Hirano, S. Awaji S. Nagaya, G. Nishijima, K. Watanabe, S. Hanai, S. Kawashima, and Y. Ishii. Unit Coil Development for Y-SMES. *IEEE Transactions on Applied Superconductivity*, 21(3):1348–1353, 2011.

[39] J. Knaster, W. Baker, L. Bettinali, C. Jong, K. Mallick, C. Nardi, H. Rajainmaki, P. Rossi, and L. Semeraro. Design issues of the precompression rings of ITER. *AIP Conference Proceedings*, 1219:145–154, 2010.

[40] J. P. Freidberg. *Plasma Physics and Fusion Energy*. Cambridge University Press, 2008.

[41] V. D. Shafranov. Plasma Equilibrium in a Magnetic Field. *Reviews of Plasma Physics*, 2:103, 1966.

[42] G. Bateman. *MHD Instabilities*. The MIT Press, 1980.

[43] R. Dengler. Self inductance of a wire loop as a curve integral. *ArXiv e-prints*, apr 2012.

[44] J. F. Hansen and P. M. Bellan. Experimental Demonstration of How Strapping Fields Can Inhibit Solar Prominence Eruptions. *The Astrophysical Journal Letters*, 563:L183, 2001.

[45] E. B. Rosa. The Self and Mutual Inductances of Linear Conductors. *Bulletin of the Bureau of Standards*, 4(2):301–344, 1908.

[46] T. Žic, B. Vršnak, and M. Skender. The magnetic flux and self-inductivity of a thick toroidal current. *Journal of Plasma Physics*, 73(5):741–756, 2007.

[47] P. M. Bellan. Why current-carrying magnetic flux tubes gobble up plasma and become thin as a result. *Physics of Plasmas*, 10(5):1999–2008, 2003.

[48] D. Kumar and P. M. Bellan. Nonequilibrium Alfvénic Plasma Jets Associated with Spheromak Formation. *Physical Review Letters*, 103(10):105003, 2009.

[49] S. You, G. S. Yun, and P. M. Bellan. Dynamic and Stagnating Plasma Flow Leading to Magnetic-Flux-Tube Collimation. *Physical Review Letters*, 95(4):045002, 2005.

[50] J. Chen, C. Marqué, A. Vourlidas, J. Krall, and P. W. Schuck. The Flux-Rope Scaling of the Acceleration of Coronal Mass Ejections and Eruptive Prominences. *The Astrophysical Journal*, 649:452, 2006.

[51] R. Liu, D. Alexander, and H. Gilbert. Kink-induced Catastrophe in a Coronal Eruption. *The Astrophysical Journal*, 661:1260, 2007.

[52] B. De Pontieu, S. W. McIntosh, M. Carlsson, V. H. Hansteen, T. D. Tarbell, P. Boerner, J. Martinez-Sykora, C. J. Schrijver, and A. M. Title. The Origins of Hot Plasma in the Solar Corona. *Science*, 331(6013):55–58, 2011.

[53] W. Liu, T. E. Berger, A. M. Title, and T. D. Tarbell. An intriguing chromospheric jet observed by *hinode*: Fine structure kinematics and evidence of unwinding twists. *The Astrophysical Journal Letters*, 707:L37, 2009.

[54] S. Lundquist. Magneto-hydrostatic fields. *Arkiv for Fysik*, 2(35):361–365, 1950.

[55] J. F. Hansen, S. K. P. Tripathi, and P. M. Bellan. Co- and counter-helicity interaction between two adjacent laboratory prominences. *Physics of Plasmas*, 11(6):3177–3185, 2004.

[56] P. M. Bellan and J. F. Hansen. Laboratory simulations of solar prominence eruptions. *Physics of Plasmas*, 5(5):1991–2000, 1998.

[57] P. M. Bellan. Thermal instability of electrolytic capacitor bank used for gas puff valve. *Review of Scientific Instruments*, 73(8):2900–2905, 2002.

[58] J. C. Thomas, D. Q. Hwang, R. D. Horton, and R. Raman. A simple fast pulse gas valve using a dynamic pressure differential as the primary closing mechanism. *Review of Scientific Instruments*, 64(6):1410–1413, 1993.

[59] A. Savtchkov, K. H. Finken, and G. Mank. Development of a fast gas valve for mitigating disruptions in tokamaks. *Review of Scientific Instruments*, 73(10):3490–3493, 2002.

[60] A. L. Moser. *Dynamics of magnetically driven plasma jets: An instability of an instability, gas cloud impacts, shocks, and other deformations*. PhD thesis, California Institute of Technology, 2012.

[61] R. H. Good. Elliptic integrals, the forgotten functions. *European Journal of Physics*, 22:119–126, 2001.